Department of Physics and Astronomy

University of Heidelberg

Master thesis

in Physics

submitted by

Lennart Huth

born in Buchen

2014

Development of a Tracking Telescope

for Low Momentum Particles and High Rates

consisting of HV-MAPS

This Master thesis has been carried out by Lennart Huth

at the

Physikalisches Institut

under the supervision of

Herrn Prof. Dr. André Schöning

Development of a Tracking Telescope for Low Momentum Particles and High Rates consisting of High-Voltage Monolithic Active Pixel Sensors

Physics beyond the Standard Model (SM) of particle physics motivates the search for the charged lepton flavor violating decay $\mu^+ \rightarrow e^+e^-e^+$ by the Mu3e experiment. This decay is suppressed with a branching ratio below 10^{-54} within the SM. Detecting this decay would be a clear sign for new physics beyond the SM. Reaching the aimed sensitivity of better than one in 10^{16} μ^+- decays in a reasonable time requires excellent momentum and vertex resolution for background suppression at high decay rates $\mathcal{O}(10^9 \mu/s)$. The maximum energy of 53 MeV of the decay particles results in a multiple scattering limited vertex and momentum resolution requiring a detector with little material. These requirements will be fulfilled by a pixel detector consisting of 50 μm thin High-Voltage Monolithic Active Pixel Sensors (HV-MAPS) with a time resolution of better than 20 ns.
A low momentum particle tracking telescope was developed to test the detector components and the data acquisition (DAQ) to perform a first integration test of the Mu3e detector and to use it at the Paul-Scherrer-Institue (PSI). The development of the mechanics and DAQ and the results of two testbeam campaigns is presented: It is shown that the readout concept of the telescope is working and that the sensors can be synchronized. It also can handle high particle rates $\mathcal{O}(600$ kHz). The mechanical alignment can be carried out with a high precision $\mathcal{O}(100$ μm). Furthermore it is shown that the particle track reconstruction works for 5 GeV electrons with thick sensors of 2 ‰ of radiation length. All measurements are supported by additional simulations.

Entwicklung eines Strahlteleskops für niederenergetische Teilchen und hohe Raten basierend auf hochspannungsbetriebenen monolithischen aktiven Pixelsensoren

Physik jenseits des Standardmodells (SM) der Teilchenphysik motiviert die Suche nach dem geladenen Lepton-Zahl verletzenden Zerfall $\mu^+ \rightarrow e^+e^-e^+$ durch das Mu3e Experiment. Dieser ist im SM mit einem Verzweigungsverhältnis von weniger als 10^{-54} unterdrückt und dessen Beobachtung wäre daher ein klares Zeichen für neue Physik. Um die angestrebte Sensitivität von weniger als einem in 10^{16} μ^+ – Zerfällen in einer angemessenen Zeit zu erreichen, wird eine hohe Zerfallsrate von $\mathcal{O}(10^9 \mu/s)$ sowie exzellente Vertex-, Impuls- und Zeitauflösung zur Untergrundunterdrückung benötigt. Durch die geringe maximale Energie von 53 MeV der Zerfallsteilchen ist die Energie- und Impulsauflösung von Vielfachstreeung dominiert. Dies erfordert einen dünnen Detektor.
Um diese Anforderungen zu erfüllen, wird der Pixeldetektor von Mu3e aus dünnen, bei Hochspannung betriebenen monolithischen aktiven Pixelsensoren (HV-MAPS) gebaut, die am Physikalischen Institut der Universität Heidelberg charaktersiert werden.
Um die Detektorkomponenten und die Datennahme des Mu3e-Detektors zu testen, sowie einen ersten Integrationstest durchzuführen und es am PSI einzusetzen, wurde ein Strahlteleskop aus HV-MAPS realisiert. Die mechanische Konstruktion, das Datennahmesystem und die Analyseprogramme werden vorgestellt. Außerdem wird der Einsatz bei zwei Strahlzeiten und deren Ergebnisse erläutert. Es wird gezeigt, dass es möglich ist ein synchronisiertes Teleskop aus HV-MAPS zu betreiben, welches hohe Teilchenraten $\mathcal{O}(600$kHz) verarbeiten kann. Außerdem ist es möglich das System mechanisch mit einer Präzision von $\mathcal{O}(100$ μm) auszurichten. Des weiteren wird gezeigt, dass die Spurrekonstruktion trotz der noch ungedünnten Sensoren, d.h. mit 2 ‰ Strahlungslänge, gute Resultate für Elektronen mit einem Impuls von 5 GeV liefert. Die Ergebnisse der Strahlzeiten lasssen sich anhand von Simulationen verifizieren.

Contents

Part I

Introduction

Introduction

One challenge in modern physics is the search for new physics beyond the Standard Model (SM) of particle physics. This search can be done in different ways. On the one hand, one can increase particle energies and try to directly produce new heavy particles. This idea is followed by experiments at large accelerators like the Large Hadron Collider (LHC) or the planned International Linear Collider (ILC). On the other hand, one can go to high particle rates to find very rare decays, which are forbidden or suppressed down to an unobservable level in the SM. This research can be done with relatively small accelerators, which deliver a high number of low momentum particles, like the High Intensity Proton Accelerator (HIPA) at the Paul-Scherrer-Institute (PSI) in Switzerland. Both research fields require new detector concepts. For completeness, it should be also mentioned that the search for new physics can also be done by searching for dark matter.

The Mu3e experiment aims to find the decay of a muon into three electrons, which is strongly suppressed in the SM or to give an upper limit on the branching ratio of this decay in the order of 10^{-16}. Therefore, an intense muon beam of $2 \cdot 10^9$ muons per second is needed to perform the experiment on an appropriate timescale. The currently existing beamline at PSI provides up to 10^8 muons per second. A new High intensity Muon Beamline (HiMB) could provide the required rate of $2 \cdot 10^9$ muons per second. In order to be sensitive to such a rare decay, one has to build a detector with very high momentum resolution, excellent vertex reconstruction and low noise to suppress background below the aimed sensitivity level. The material budget in the active region has to be minimized to reduce multiple Coulomb scattering, which limits the vertex and momentum resolution at low particle momenta. The last important issue is to have an excellent timing to reduce combinatorics.

This can be achieved by the use of a novel silicon pixel design, the so called High Voltage Monolithic Active Pixel Sensor (HV-MAPS). The main advantages of this technology are the fast pixel readout, which reduces the dead time of the detector, and the fact that the electronics of the chip is directly implemented in the active area. Therefore no additional separate electronic layer is required, which would introduce additional material. Due to the thin active area the chip can be thinned down to less than 50 µm. The high event multiplicity additionally requires very precise timing in the order of 100 ps. This requirement can be met by scintillating fibers and tiles, which are also included in the detector design.

All new devices have to be tested, characterized and specified for the usability in the Mu3e experiment. Therefore, the MuPix HV-MAPS prototypes are characterized in the lab at the Physikalisches Institut (PI) in Heidelberg and in test beams at DESY in Hamburg, at CERN and at PSI in Villigen. At DESY, the spatial resolution of prototypes can be determined with the EUDET-telescope installed in test beam area T22. At PSI such a beam telescope is not available.

These particle tracking telescopes are an important tool to characterize new devices. The MuPix sensor is a perfect candidate to build such a telescope due to its properties. In addition, the HV-MAPS technology can handle high particle rates and allows for thin sensors suitable for low momentum particle tracking. The MuPix sensor characterization at PI provides all the needed electronics and support structure to build a telescope. Due to these advantages and as an integration test, it was decided to build a standalone, flexible and compact low momentum particle tracking telescope from the MuPix prototypes at the PI in Heidelberg.

The goal of this thesis is to develop such a telescope. Therefore a new mechanical structure is designed and relaized, which is used to mount the telescope planes. The electronics of four single sensors have to be connected to a common readout computer and synchronized. Also a DAQ software has to be developed, based on the DAQ software for the single MuPix test setup.

At the beginning, the SM and Lepton flavor violating decays are explained, which motivate the MU3e experiment that is discussed afterwards. In the third chapter, the interaction of particles with matter and their detection is discussed in more detail, followed by a introduction in particle track reconstruction, focusing on straight tracks. The fifth chapter introduces the MuPix telescope and discusses the used components adapted from the Mu3e experiment in detail. The following chapter examines the data acquisition system and explains the graphical user interface. The simulations of the telescope are addressed in the seventh chapter. Chapter eight and nine discuss the two testbeam campaigns carried out and their results. At the end, the work is summarized and an outlook is given.

Chapter 1

The Standard Model of Particle Physics

The Standard Model (SM) of particle physics [1] is a quantum field theory describing the smallest constituents of matter, the elementary particles, and their interactions. Figure 1.1 shows a schematic view of the particle content of the SM, consisting of six quarks (and anti quarks), six leptons (and anti leptons), four gauge bosons and the Higgs boson.

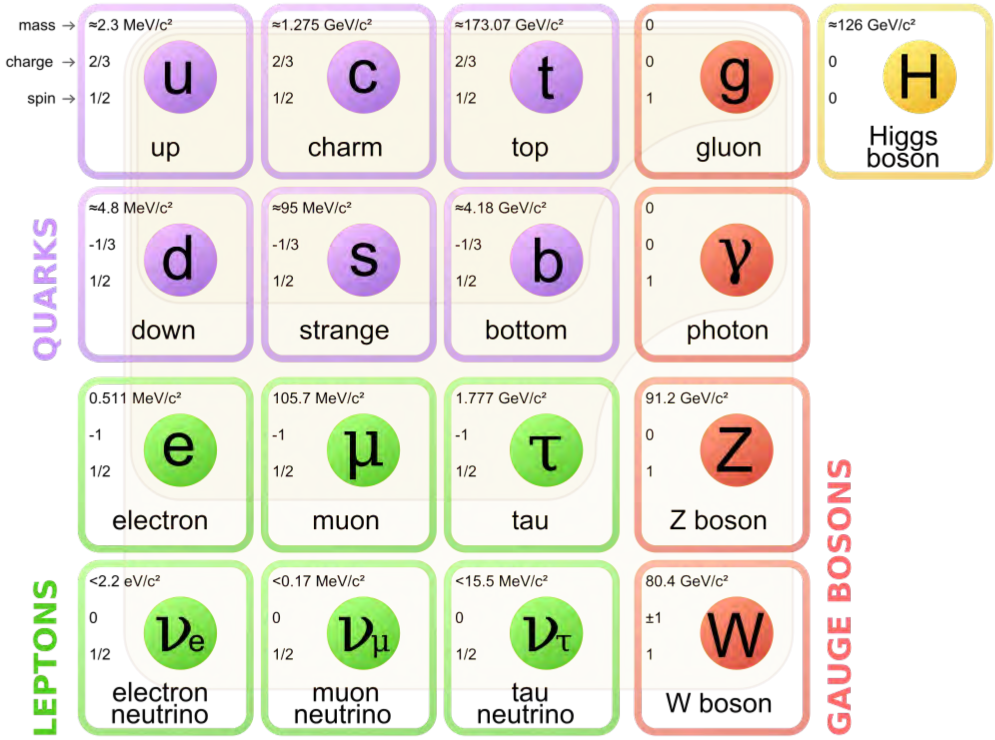
mass →
charge →
spin →
≈2.3 MeV/c² 2/3 1/2 u up
≈1.275 GeV/c² 2/3 1/2 c charm
≈173.07 GeV/c² 2/3 1/2 t top
0 0 1 g gluon
≈126 GeV/c² 0 0 H Higgs boson
≈4.8 MeV/c² -1/3 1/2 d down
≈95 MeV/c² -1/3 1/2 s strange
≈4.18 GeV/c² -1/3 1/2 b bottom
0 0 1 γ photon
0.511 MeV/c² -1 1/2 e electron
105.7 MeV/c² -1 1/2 μ muon
1.777 GeV/c² -1 1/2 τ tau
91.2 GeV/c² 0 1 Z Z boson
<2.2 eV/c² 0 1/2 νe electron neutrino
<0.17 MeV/c² 0 1/2 νμ muon neutrino
<15.5 MeV/c² 0 1/2 ντ tau neutrino
80.4 GeV/c² ±1 1 W W boson
QUARKS
LEPTONS
GAUGE BOSONS

FIGURE 1.1: The Standard Model of particle physics [2].

The quarks and leptons are arranged in three generations and the interactions between them are mediated by the gauge bosons. The first generation consists of the two lightest quarks up (u) and down (d) with a charge of +2/3 and -1/3, respectively, the electron (e^-) with an electric charge of -1 and the neutral electron neutrino (ν_{e^-}). The second and third families look similar: Two quarks, one charged lepton and one neutrino with the same quantum numbers, but with different masses. The second family consists of the charm (c) and the strange (s) quark, the muon (μ^-) and the muon neutrino (ν_μ), while the third family contains the top (t) and bottom (b) quarks, the tau (τ^-) and the tau neutrino (ν_τ). The neutrinos are assumed to be massless in the SM, while the lepton flavour number (the number of leptons minus anti leptons from the same family) is conserved in every decay.

All particles from the three families are spin 1/2 particles, the so called fermions interact via the exchange of gauge bosons which are spin 1 particles. The interactions between the particles are classified in three groups: The electromagnetic interaction is mediated by the photon (γ), the eight gluons are responsible for the strong interaction and the Z, W^+ and W^- mediate the weak interaction.

The SM is one of the most successful theories in modern physics and is confirmed by numerous experiments. Especially the discovery of the long ago predicted Higgs boson at the LHC [3, 4] has shown, that the SM is consistent: The Higgs boson is a manifestation of the Higgs field responsible for the symmetry breaking between the electromagnetic and weak interactions (i.e. the larger masses of the W and Z bosons).

Nevertheless there are many effects, that can not be explained by the SM, like neutrinos oscillating between different flavour eigenstates, which is observed in many experiments like SNO [5], Daya-Bay [6], Super-Kamiokande [7]. This is only possible by introducing mass differences between the neutrino mass eigenstates. One way is expanding the SM by introducing a heavy right-handed neutrino, which gives a small mass to the left-handed ones (the so called seesaw mechanism [8]). Even if neutrino oscillations can be explained with an extended SM, there are still many open questions: Why do we only have 3 families? How can gravity be explained? Why do we have a matter - antimatter asymmetry in the universe? What is the origin of dark matter? What happens at higher energies? Is the charged lepton flavor conserved in all decays?

Those questions are linked to many new theories (beyond the SM) which try to explain those effects and predict new particles. Those theories have to be verified by new experiments, reaching higher energies and/or higher rates.

1.1 Muon Decays

Many models for physics beyond the standard model predict measurable amounts of charged lepton flavour violation (cLFV) processes. cLFV could be observed in the decays of leptons, such as muon decays. The dominating muon decay into two neutrinos and an electron is shown in Figure 1.2a.

One possible LFV muon decay is the decay $\mu^+ \to e^+e^-e^+$, which is forbidden on tree level in the SM and can therefore only happen via higher order loop corrections with neutrino oscillation (compare Figure 1.2b). This decay is strongly suppressed in the SM with a branching ratio (BR) of below 10^{-54}. Therefore it is not observable and any observation would be a very clear hint for new physics beyond the SM. There are several theories predicting an increased BR for this decay, like γ/Z penguin diagrams with a loop of supersymmetric (SUSY) particles or tree diagrams with new particles like heavy vector bosons, doubly charged Higgs or scalar neutrinos. Two possible diagrams are shown in Figure 1.3.

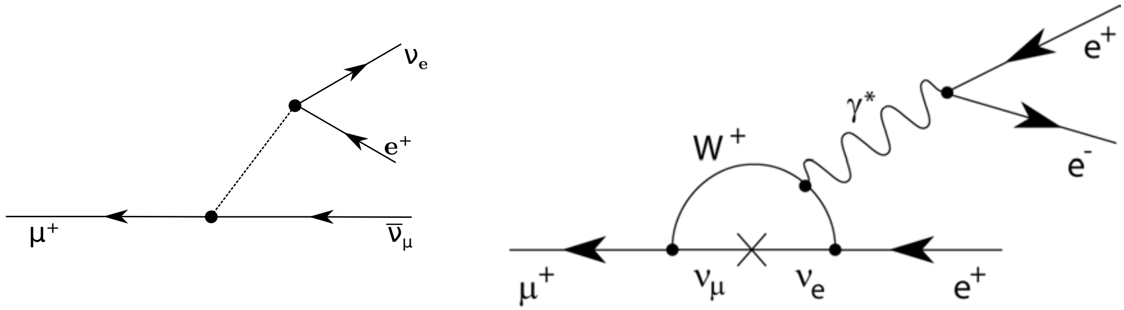

(A) Feynman graph of the dominating muon decay channel in the SM: $\mu \to e + \nu_\mu + \bar{\nu_e}$.

(B) Neutrino mixing loop diagram of the decay $\mu^+ \to e^+e^-e^+$.

Figure 1.2: Feynman graphs of possible SM muon decays.

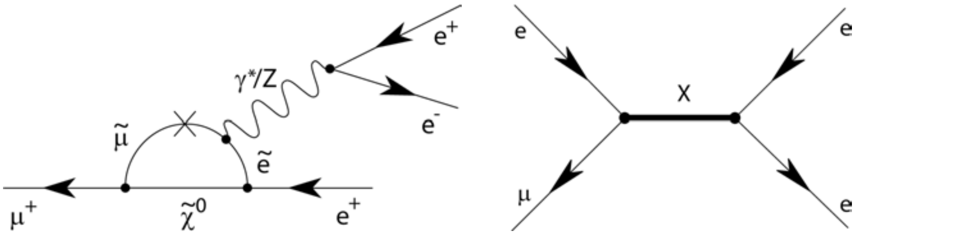

(A) Penguin diagram with a SUSY loop.

(B) Tree diagram with new particles.

Figure 1.3: Feynman diagrams for $\mu^+ \to e^+e^-e^+$assuming beyond SM physics.

Chapter 2

Mu3e - Search for New Physics at the High Rate Frontier

As mentioned in the introduction, the search for new physics is a central and challenging part of modern particle physics. In the following the research in the context of high rate experiments in the muon sector is addressed. At the beginning a rough overview over the current experimental situation is given. The second section discusses the Mu3e experiment in detail, beginning with the signal decay followed by the main backgrounds and the resulting requirements. Subsequently the experimental concept and the used detectors are introduced. At the end, the muon beam available at PSI is discussed.

2.1 Experimental Situation

In the year of 1953, the first experiment searching for charged lepton flavor violation in muon decays started data taking. Up to now no signal was found, only upper limits on branching ratios were achieved. The best limit on the $\mu^+ \to e^+e^-e^+$ branching ratio is set by SINDRUM [9], while MEG [10] is leading in the $\mu \to e\gamma$ search.

SINDRUM

The SINDRUM [9] experiment searched from 1983 to 1986 for the process $\mu^+ \to e^+e^-e^+$ and did not detect any signal. They set a limit on the branching ratio of BR($\mu^+ \to e^+e^-e^+$) $< 10^{-12}$ at 90% confidence level (C.L.). The SINDRUM detector was placed at PSI and consisted of a hollow double cone target to stop 28 MeV/c surface muons in a solenoid magnetic field of 0 33 T. The target was surrounded by five tracking layers of multiwire proportional chambers and a trigger hodoscope. The main background

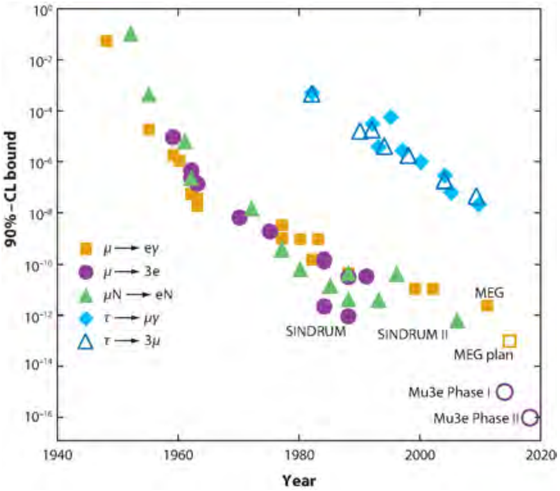

FIGURE 2.1: The history of LFV muon decay research, adapted from [11].

was given by the decay $\mu^+ \to e^+e^+e^-\overline{\nu_\mu}\nu_e$ which was estimated to be $5 \cdot 10^{-14}$. So the published SINDRUM result was only limited by the number of stopped muons.

MEG

The MEG experiment [10] searches for the LFV decay $\mu^+ \to e^+\gamma$ and is in operation since 2008. The main detection concept is to detect the positron in a drift chamber and the photon in a liquid Xenon calorimeter. The MEG-system was updated after the run time in 2008 and the data analysis yielded to an upper limit of $\mathrm{BR}(\mu^+ \to e^+\gamma) < 5.7 \cdot 10^{-13}$ [12]. The MEG detector will be upgraded [13] and is supposed to continue searching for $\mu \to e\gamma$.

2.2 The Mu3e Experiment

Mu3e [14] is an experiment, which searches for the lepton flavor violating decay of a positive muon into two positrons and one electron and aims for a high sensitivity, requiring $2 \cdot 10^9$ muons per second. Such an intense beam does not exist at the moment, but could be realized at PSI after 2019 [15]. To handle the large amount of data, a non triggered readout with fast online track reconstruction is proposed. To suppress background, excellent timing with a time resolution of $\mathcal{O}$ (100 ps) as well as fast and good vertex reconstruction with a spatial resolution $\mathcal{O}$ (100 μm) is required for the online event filter.

2.2.1 Signal Decay

The $\mu^+ \rightarrow e^+e^-e^+$decay signal has a vanishing total momentum

$$\vec{p}_{tot} = \sum_{i=0}^{2} p_i = 0 \tag{2.1}$$

because the muons decay at rest. The total energy has to be equal to the muons rest mass of 105.659 MeV/c^2 [1]:

$$E_{tot} = \sum_{i=0}^{2} E_i = m_\mu \cdot c^2. \tag{2.2}$$

Equation 2.1 restricts the electrons energy between $m_e c^2$ and 1/2 $\mathrm{m}_\mu \approx 53$ MeV.

2.2.2 Backgrounds

The detection of a very rare decay requires a good understanding of backgrounds and the possibility to suppress them down to a level below the desired sensitivity. The two critical backgrounds are random combinations and internal conversion.

Random Combination Background

The high rate operation of Mu3e leads to many decays. The probability to find a configuration similar to the $\mu^+ \rightarrow e^+e^-e^+$ signal by random combinations is quite high: Two positrons from Michel decays (the dominant muon decay, shown in Figure 1.2a) can combine with an electron from a photon conversion process or mis-reconstruction (see Figure 2.2). Since the particles originate from different decays, they do not share a common vertex and most likely the sum of their momenta and energy does not vanish. In addition, the decays do likely not happen exactly at the same time. This background can be efficiently suppressed by excellent time, momentum and spatial resolution.

Internal Conversion

The second and most challenging background is the internal conversion, shown in Figure 2.3a. A muon decay with an additional virtual photon that converts into an electron-positron pair can be misinterpret as a signal. Since all particles come from the same decay, they are coincident in time and share the same vertex, but they have in average lower momentum and energy due to the two neutrinos carrying away energy which is not detected. The branching fraction can be calculated as a function of missing energy [16] and is plotted in Figure 2.3b. To reach the aimed sensitivity of $< 10^{-16}$

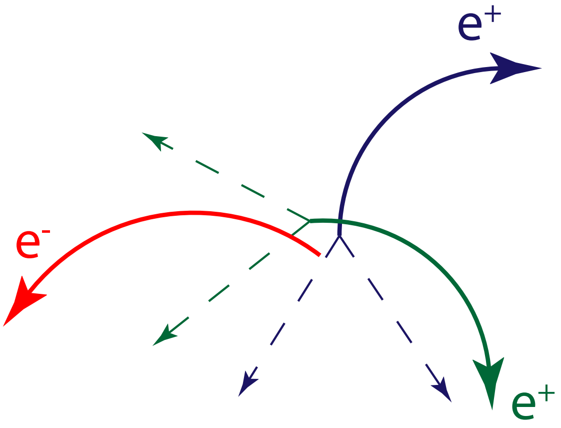

Figure 2.2: Accidental background from three different decays.

at 90% C.L., the invariant mass resolution has to be better than 1 MeV, to be able to reliably distinguish the signal from this background.

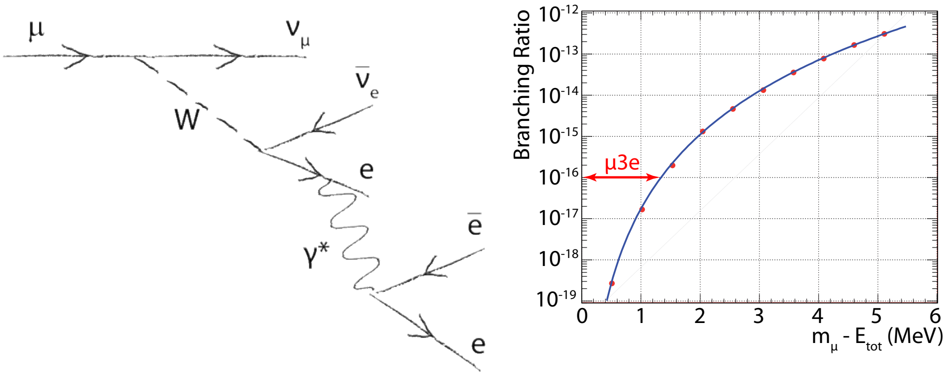

(a) Feynman graph of the internal conversion decay.

(b) Branching ratio of the internal conversion process versus the missing energy [16].

Figure 2.3: Internal conversion background

2.2.3 Requirements

The characteristics of the decays described above pose stringent requirements on a detector built to search for the signal $\mu^+ \rightarrow e^+e^-e^+$: First of all, high rates have to be handled. Secondly, excellent vertex reconstruction, momentum resolution and timing are needed. Thirdly the detector has to be very thin to reduce effects of multiple scattering without losing sensitivity for charged particles. The geometrical acceptance and the efficiency of the sensors should be as high as possible to reduce the required measurement time.

2.2.4 Experimental Concept

The central principle of the Mu3e experiment is to stop more than 10^{16} muons in total on a large surface. Therefore, the muon beam is stopped on a double hollow cone target made of aluminum. The stopped muons decay at rest and the decay particles are bent in a homogeneous static magnetic field of 1 Tesla. Four layers of pixel detectors arranged in two double layers measure the particle tracks with very high precision. Inside the third pixel layer an array of scintillating fibers is used for precise timing. The re-curling electrons and positrons are detected again by a double layer of pixel detectors and stopped in scintillating tiles, which give the most precise timing information of below 100 ps. A sketch of the detector is shown in Figure 2.4.
Due to the low momentum of the decay electrons, the detector is built as thin as possible in order to reduce multiple scattering. In addition, the cooling of the detector is done with a constant flow of gaseous helium [17, 18, 19], which has the advantages of a good heat transfer and low multiple scattering.

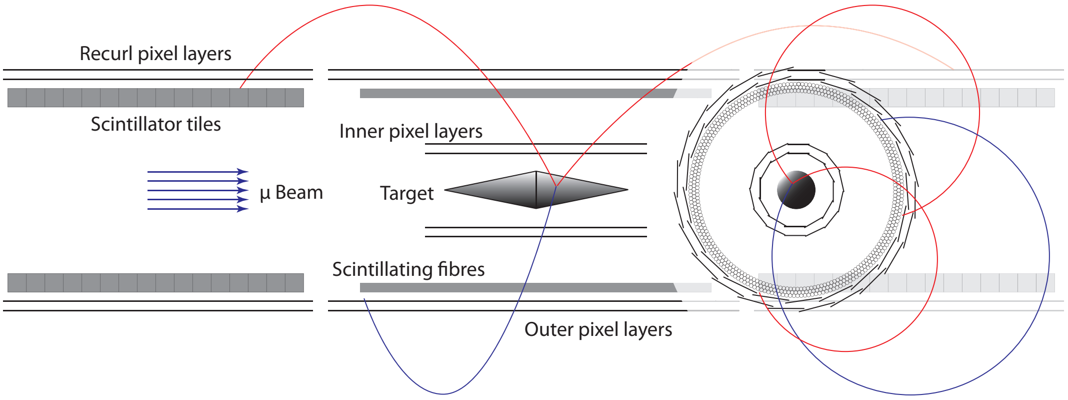

Figure 2.4: Schematic view of the Mu3e detector with a $\mu^+ \rightarrow e^+e^-e^+$signal event decay. On the right side, a view along the beam axis is given. [14]

2.2.5 Sub Detectors

Pixel Detector

The pixel detector is based on HV-MAPS (see Chapter 3.2) with a pixel size of 80x80 μm^2. One chip has 1x2 cm^2 in size in the inner layer and 2x2 cm^2 in the outer and recurl layers. In total, an area of more than a square meter with 275 million pixels is used to track particles.
To reduce the material budget below 1 ‰ of radiation length per pixel layer, the sensors are thinned to 50 μm, glued on top of a 25 μm thick Kapton foil and wire bonded to

the Kapton flexprint cables. The readout is supposed to run via serialized 800 MBit/s thin Low Voltage Differential Signaling (LVDS) links and is zero suppressed.
The mechanical structure is self supporting and a mockup has already been constructed with thin glass layers as a silicon sensor replacement. A picture of a half barrel with the two black plastic end pieces and Kapton flexprint cables replacements mounted is shown in Figure 2.5.

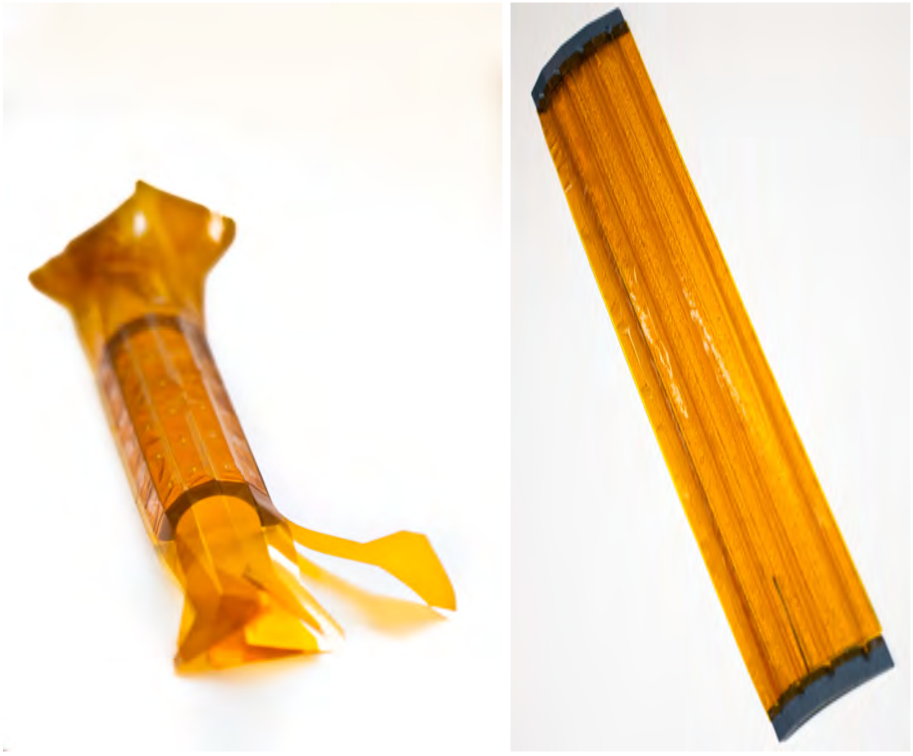

(A) Inner pixel layer prototype

(B) Outer pixel layer prototype

Figure 2.5: Kapton pixel support structure prototypes

The pixel chip itself is under development and prototypes, shown in Figure 2.6 have been analyzed, tested, characterized and improved in various bachelor and master theses [20, 21, 22, 23, 24]. A detailed description of the prototypes can be found in Chapter 5.

Fiber Tracker

The fiber tracker consists of three to five layers of 250 µm diameter and 36 cm scintillating fibers. They are read out by arrays of compact silicon photomultipliers at both ends and have a timing accuracy in the order of a few hundred picoseconds. The fibers are placed at a radius of 6 cm from the target center, in between the inner and outer pixel layers (the grey central area in Figure 2.4). The fiber tracker is developed at

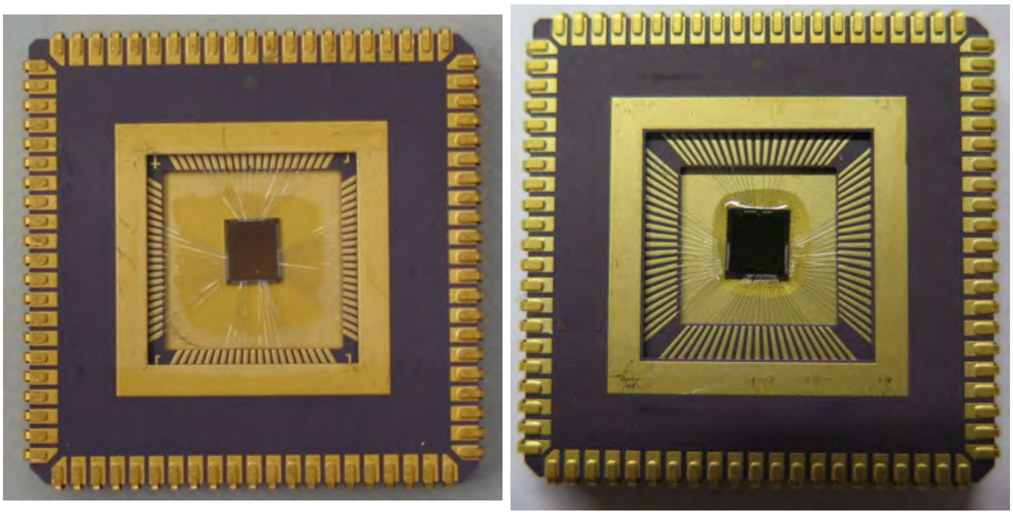

(A) MuPix 4 prototype

(B) MuPix 6 prototype

Figure 2.6: Top view of the MuPix 4 and 6 prototypes, glued and bonded on a carrier.

the University of Zürich, Eidgenössische Technische Hochschule Zürich, University of Geneva and Paul-Scherrer-Institute.

Scintillating Tiles

The scintillating tiles consist of 7.5 x 7.5 x 5 mm sized scintillating tiles, which are read out by silicon photomultipliers as well. The tiles will be placed in the outer recurl layers of the detector (grey blocks in Figure 2.4) and give a very precise timing below 100 ps. They are developed at the Kirchhof-Institut für Physik at Heidelberg [25]. They are also used as a timing reference for the MuPix telescope.

2.2.6 Readout Concept

The Mu3e readout chain, sketched in Figure 2.7, is designed to send time slices of the complete detector information to each GPU on the filter farm. Therefore, the complete information from all sub detector systems has to be buffered, sorted, merged and transformed into a useful data structure by the data acquisition (DAQ) system using 238 FPGAs, which are handling a data stream of about 1 TBit/s. This stream is sent to readout boards, which transit short time slices of the complete detector information to the GPU-filter farm. Here, the tracks are reconstructed online, the events of interest are selected and sent to a Data Collection Server. This server writes the data to a mass storage system.

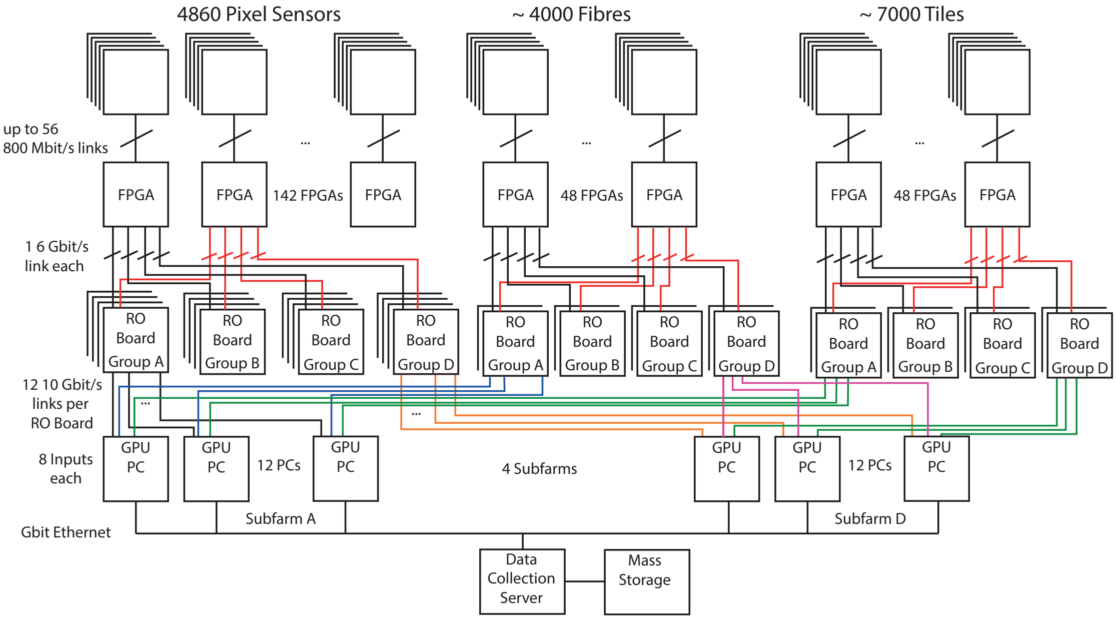

Figure 2.7: Schematic of the Mu3e DAQ chain: The data from all sub detectors, sent via 108 links, with 800 MBit/s each, is buffered in 238 FPGAs and sent to the readout boards. From those boards, the data is send to the GPU farm and the tracks are reconstructed. The final data is stored.

2.2.7 Muon Beam

The Mu3e experiment is planned to run in two phases, using the most intense available muon beam at the experimental hall of PSI, shown in Figure 2.8:
The cyclotron at PSI delivers a 2.2 mA 590 MeV proton beam, which hits the rotating carbon target E and produces pions. They decay at rest and the muons are collected into the beamline πE5, which provides a 28 MeV/c muon beam with a rate in the order of 10^8 muons per second. This beam and a measurement period of roughly three years are required to reach a sensitivty of 10^{-15}.
Phase II aims for another order of magnitude improvement in sensitivity and therefore needs a more intense muon beam. This could be realized by the planned High intensity Muon Beamline (HiMB) at the SINQ spallation neutron source [26]. This beamline will provide a beam of more than $3 \cdot 10^9$ muons/s while the Mu3e experiment requires $2 \cdot 10^9$ stopped muons per second for the aimed sensitivity in Phase II.

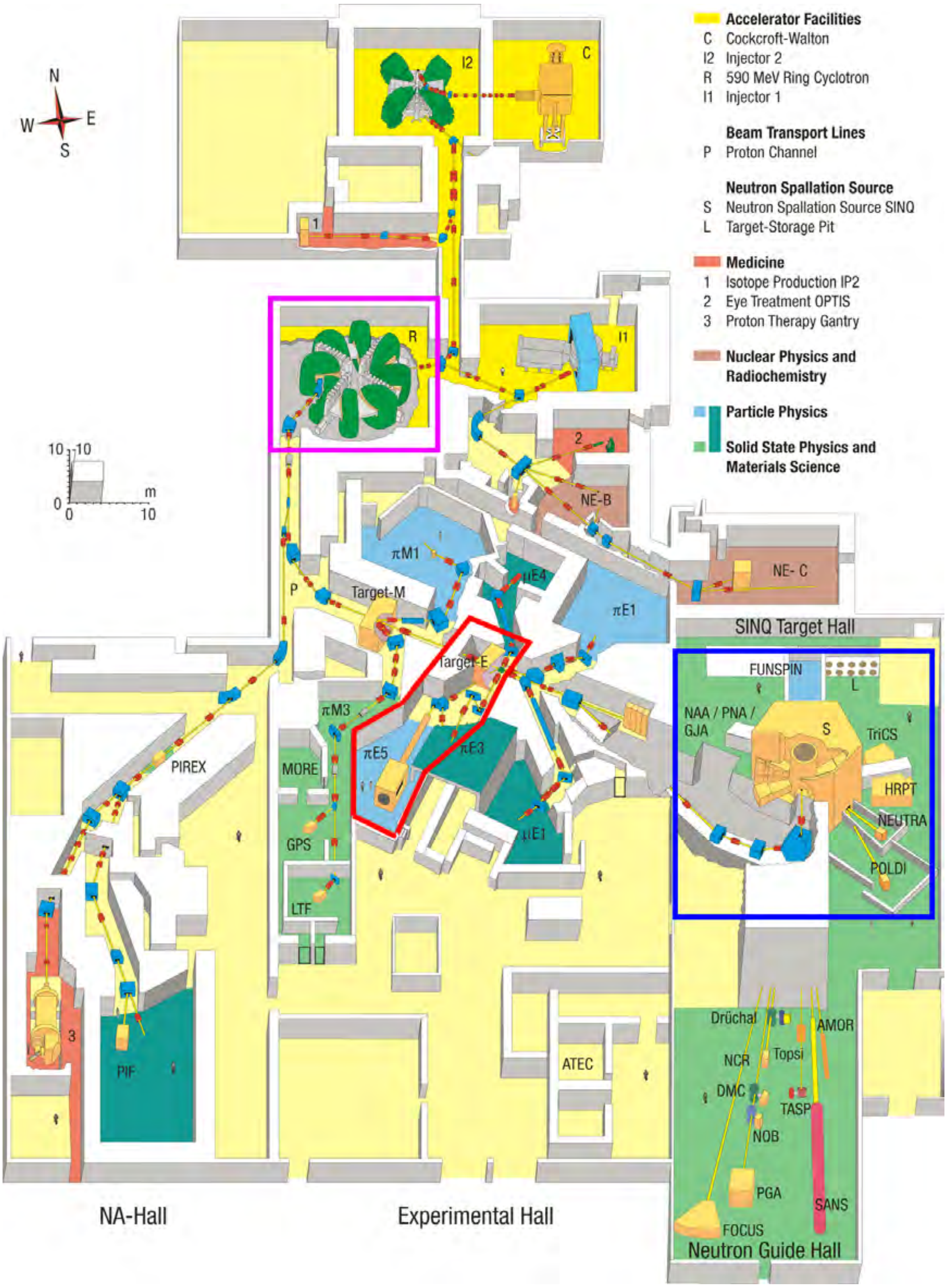

Figure 2.8: The experimental hall of the PSI with the beamlines and the different areas. The Mu3e experiment will be located in the area surrounded in red. The main accelerator is located at the north-west corner of the hall and marked in purple. The SINQ target is placed on the east side, marked with a blue square. Image from [23] .

Chapter 3

Particle Interaction and Detection

In the first part of this chapter the central concepts of particle interactions with matter is discussed. First the interactions of particles are explained, followed by a detailed description of multiple Coulomb scattering.
For particle tracking in general and in the Mu3e experiment, the position of a particle using detector layers of position sensitive devices is measured. They are addressed in a second part, focusing on **H**igh-**V**oltage **M**onolithic **A**ctive **P**ixel **S**ensors (HV-MAPS), which are used for the Mu3e experiment and the telescope.
The last part discusses two central tools required to control and readout a detector: Signal transmission and the technology of FPGAs.

3.1 Particle Interactions with Matter

The particle interaction depends strongly on the particle's charge, mass and energy and the matter itself. First of all, one distinguishes between charged and neutral particles. In addition, there is an important difference between light particles (electrons and photons) and heavy particles and ions (protons, neutrons, heavy nuclei,...). In the following, only interactions of electromagnetic charged particles are described, because they are the most relevant for telescopes.

Heavy Particles

Heavy particles can interact via electromagnetic interaction. The most important one is ionization, which depends strongly on the particle's energy. The mean energy loss is described by the so called Bethe-Bloch formula [27]:

$$-\langle\frac{\mathrm{d}E}{\mathrm{d}x}\rangle = \frac{4\pi n z^2}{m_\mathrm{e} c^2 \beta^2} \cdot \left(\frac{e^2}{4\pi\epsilon_0}\right)^2 \cdot \left[\ln\left(\frac{2 m_\mathrm{e} c^2 \beta^2}{I \cdot (1-\beta^2)}\right) - \beta^2\right] \tag{3.1}$$

with the relative velocity β defined as the particles velocity v over the speed of light c, the charge number z, particles energy E, traveled distance x, electron charge e, electron mass m_e, electron density in the material n and the mean excitation potential I ($\approx 10eV \cdot Z$, with atomic number Z). Equation 3.1 shows, that the energy loss has a minimum at $E \approx 3 \cdot \beta\gamma = 3 \cdot \frac{p}{m_0 c}$. Particles with the corresponding momentum deposit only little energy in the material and are called minimum ionizing particles. For higher momenta, the energy loss increases logarithmically due to the relativistic extension of transversal E-field. Towards lower energies, the energy loss increases proportional to β^{-2} due to the increasing interaction time between the particle and the E-field.

Electrons

Electron interactions with matter are dominated by two processes [1]: Ionization and Bremsstrahlung. The energy loss due to ionization increases logarithmically with energy, while the loss due to Bremsstrahlung increases linearly with energy. For low momentum particles, ionization is therefore dominant. The higher the energy gets, the stronger becomes the influence of Bremsstrahlung. The energy, where both effects are equal defines the critical Energy. Above this energy, the Bremsstrahlung becomes dominant.
Bremsstrahlung describes electromagnetic radiation due to deceleration of charged particles in the field of a nucleus. The emitted photons can build positron electron pairs if their energy is above 2 $\cdot m_e$ and an electromagnetic shower is initialized.
The energy loss is similar to the one of heavy particles with corrections for the lower mass and the possibility of electron exchange with the shell electrons [28].

3.2 Multiple Coulomb Scattering

Beside the energy loss particles also scatter at nuclei, while traveling through matter. For precise particle tracking a detailed understanding of multiple Coulomb scattering is required. The theoretical treatment of multiple scattering was studied first in 1922 [29] and fully developed in the 1940ies [30, 31, 32, 33] and summarized in [34]. These theories all assume the scattering angle being independent of the material thickness, which is obviously not correct. Lewis included this effect in his paper from 1950 [35]. The effects, changing the direction of flight and the plane position are summarized for small scattering angles in Figure 3.1. For experimental usage, the Highland [36] parametrisation can be used to define Θ_{MS} [37] as

$$\Theta_{MS} = \frac{13.6\ \text{MeV}}{\beta c p} z \sqrt{\frac{x}{X_0}} \left(1 + 0.038 \ln \frac{x}{X_0} \right), \tag{3.2}$$

with Θ_{MS} being the RMS of the central 98% of the planar scattering angle distribution, the particles velocity in units of the speed of light β, the material's radiation length X_0, the material's charge number z and the particle's momentum p. Obviously the scattering strongly depends on the particle's momentum and becomes more important at lower energies. Therefore the momentum range has to be considered when designing detectors. The displacement of the particle , e.g. y_{plane} in Figure 3.1, is negligibly small for very thin detectors like the HV-MAPS and only the deflection angle has to be taken into account.

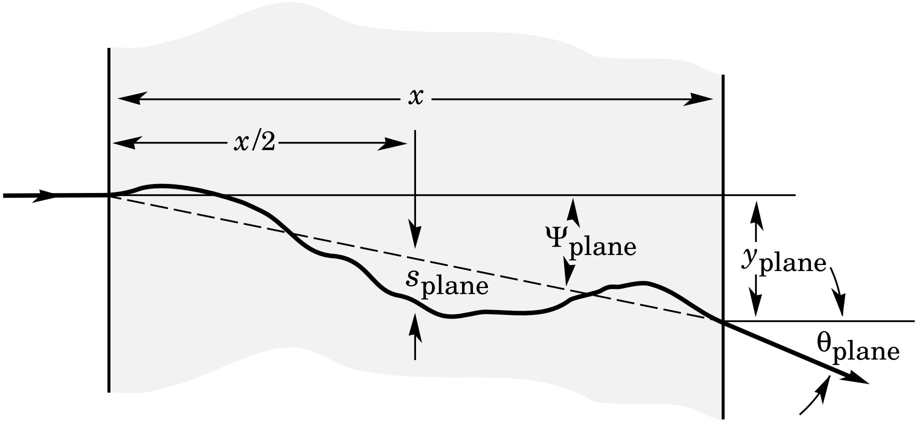

Figure 3.1: Sketch to visualize the small angle multiple scattering effect [37].

3.3 Particle Tracking Detectors

Particle tracking detectors are used to identify particles, measure the momentum and energy and the velocity. All those concepts require measurements of the particles position on a detector layer. Therefor position sensitive devices are needed.

Position Sensitive Devices

The detection of particles can only be done via the interaction of particles with some material. A strong interaction of a particle with the detector material allows for high signals, but the particle characteristics change strongly. So there is always a trade-off between detecting a particle and changing its energy and momentum. In the case of a tracking experiment, the momentum and direction of flight should be affected as little as possible. This means, that the multiple Coulomb scattering and energy loss should be small - this only can be achieved by reducing the material budget the particle has to travel through, while it still has to loose enough energy in the detector to be detected. In order to build a position sensitive device, the sensitive medium is usually segmented and each segment is read out separately. Depending on the task, the active media can be solid, liquid or gaseous and the segmentation size can differ. Besides the common problem of the different velocity of ions and electrons, which are produced by a particle interacting with matter leading to space charge effects, each detection material has advantages and disadvantages:

- **Gaseous:** The main advantage is the small amount of material needed for those devices. A particle traversing the gas leads to ionization. A strong electric field is required to collect the ions and electrons via drift. Gases have the disadvantage of being slow and having a large drift and dead time (μs). Additionally there are the issues of aging and strong space charge effects for high rate. Therefore they can only handle low rates and multiplicities.
- **Liquid:** They are often used to build large volume detectors for neutrino experiments, have the advantage of large volume capacities and have a relatively low spatial resolution. A disadvantage is that thick walls are needed to stand the pressure of the liquid. This makes it not suitable for low momentum tracking. The particles can be detected via created scintillation light, Chrenkov light and drift. For position measurements drift and scintillation can be used. Scintillation and Cherenkov light are fast, but charge collection via drift in those systems (i.e. Time-Projection-Chambers) is very slow.
- **Solid:** Solid state detectors are the most compact ones and have the advantage of a small absolute size, but usually involve the most expensive technology. They can be very fast, handle high rates and are often used for vertex detection at collider experiments. Their disadvantage is that they have the highest density introducing a large amount of scattering if they are thick (usually in the order of a percent of radiation length).

For a tracking telescope for low momentum particles, one can use gaseous or solid concepts, but if one wants to handle high rates, the best choice is a solid-state detector. Usually, rectangular segmented ones, so called pixel detectors are used. The most common materials are silicon and germanium.

3.3.1 Silicon Pixel Detectors

Silicon pixel detectors are based on a well understood technology and they are used in many experiments (ATLAS, ALICE, CMS,...). The classical approach is to use a sensitive segmented material, which is connected via bump-bonds to a chip with the readout electronics. The charge collection is done in reversed biased HV diodes. The bumps usually consist of a high z material like tin and introduce a significant amount of multiple scattering. The second and most important issue concerning this hybrid detector type is the huge amount of bumps: It is very complicated to connect all the pixels to their electronics. This makes the technology very expensive. As an example, one can take the ATLAS pixel sensors: They consist of an active part, the p-n-p silicon sensor chip and the separate readout chip. Both elements are connected with 25 µm bumps, which are spaced by roughly 50 µm. The complete sensor is roughly 1 mm thick and therefore unusable for experiments with low momentum tracking due to the amount of multiple scattering.

The solution for this problem was already developed in the 60s: Active-pixel-sensors (APS). An APS pixel consists of a CMOS-diode as active sensor next to the readout electronics on the same chip. Unfortunately, the sensitive area is only in the order of 30 % of the chip, which is not enough for particle tracking. APS are used for imaging sensors.

3.3.1.1 MAPS

The next step in the active sensor technology development are the **M**onolithic **A**ctive **P**ixel **S**ensors (MAPS), which use the complete sensor as active material and implement the electronics directly on top of the active area, as shown in Figure 3.2 [38]. With this technique, one can achieve an active area of nearly 100 % and use the sensors for particle detectors like the STAR experiment [39]. Due to the use of a commercially available CMOS process, the production of these sensors is reasonably priced. Another advantage is, that the minimal structure size for these processes is very small (down to 23 nm). The main disadvantage is the slowness of the sensor, because the charge is collected via diffusion, which is much slower than the collection time in bump bonded sensors, which are operated with HV and have charge collection via drift.

3.3.2 HV-MAPS

A fast charge collection can be achieved with a novel detector technique, unifying the advantages of the different technologies, the **H**igh-**V**oltage **M**onolithic **A**ctive **P**ixel **S**ensors (HV-MAPS) [38]. The principle, shown in Figure 3.2, is to implement the discriminator logic directly in the pixel cell: The p-substrate surrounds a slightly n doped n-well, building up the diode. Applying high-voltage $\mathcal{O}$ (50–80 V) on this diode in reverse direction results in a small depletion zone of a few µm thickness which is used as a sensitive layer. Charge created in the depletion zone drifts to the electrode in a strong electric field, which leads to a charge collection time below 1 ns. A schematic of a 2x2 matrix of the HV-MAPS is visualized in Figure 3.3. The charge is collected

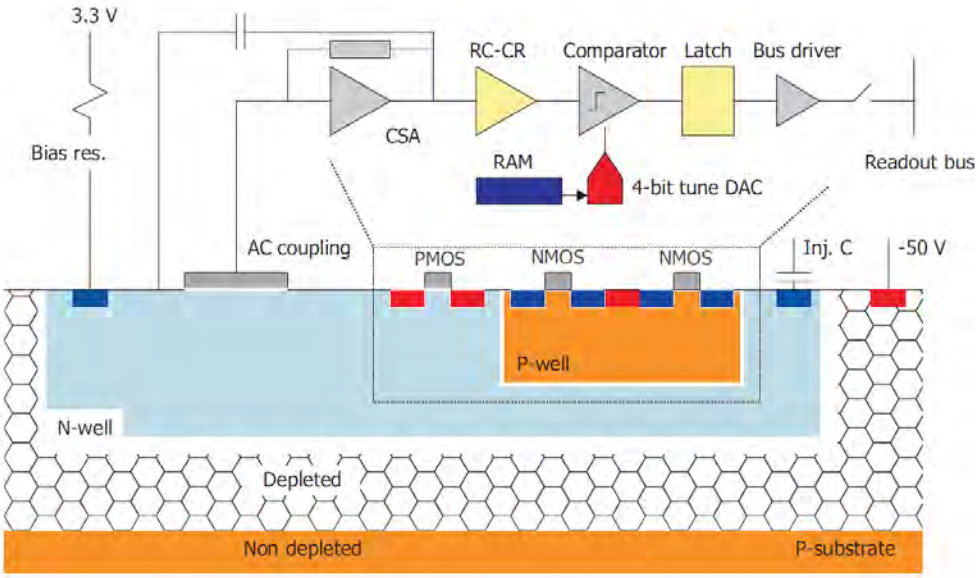

Figure 3.2: Schematic view of a MuPix2 HV-MAPS pixel cell [38]. For the prototypes 4 and 6, the comparator is moved outside the pixel into the periphery.

in the n-well, where the analog and digital electronics are directly implemented. This process is commercially available and reasonably priced.

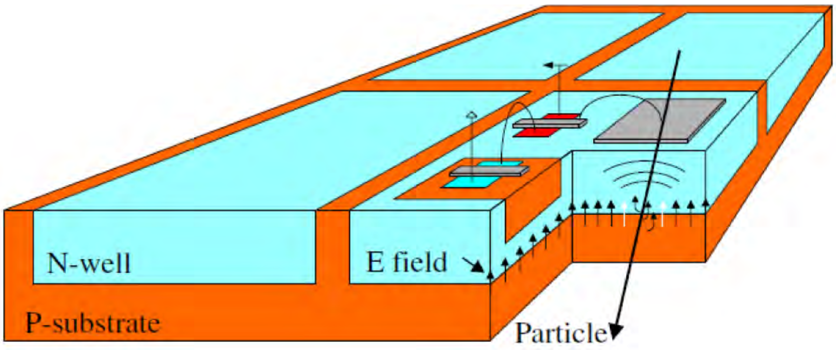

Figure 3.3: Schematic view of a 2x2 pixel matrix of a HV-MAPS with a charged particle traversing it. The arrows indicate the E field and the charge drift [38].

3.4 Data Transfer and Readout

3.4.1 Field Programmable Gate Arrays (FPGA)

FPGAs started to appear in the 1980s, as a reaction to the growing complexity of electronic circuits. It was not longer sensible to build application-specific integrated circuits (ASICS) for all purposes, due to high costs and development time. In order to keep the advantages of being very fast, compact and having a low power consumption

compared to software solutions, programmable interconnections between different logical elements became more and more important. A good compromise in this context is the use of FPGAs: They consist of an array of up to several thousand basic building blocks which can be interconnected by programmable switches. In principle, each logic cell can be connected to every other cell on the chip and each input or output pad can be connected to every other logic element. A program, written in a hardware description language, can be used to configure the connections and describes the FPGA's functionality.
During the last 30 years, the amount of in- and outputs and logic blocks strongly increased and FPGAs were established as standard components in modern particle physics.

3.4.2 Signal Transmission

Digital and Analog Signals

There are two different principles for electrical signal transmission. They can be either analog or digital. Analog signals are continuous signals and are for example represented by the time development of a physical value like the current or voltage. The higher the amplitude of an analog signal, the stronger the corresponding quantity. Those signals have the advantage of transporting the complete information of a system, but they are hard to implement in logic and very sensitive to electrical fluctuations and noise. Therefore, analog signals are usually converted into digital ones. Digital signals take the values one or zero, depending on the intensity of an electrical signal. Under a certain threshold (the red Threshold low line in Figure 3.4), the signal is interpreted as zero, over another threshold it is interpreted as a one (blue Threshold high line in Figure 3.4). This makes for more stable and noise resistant signals. This conversion can be done by so called "Analog-to-Digital-Converters" (ADCs). The simplest ADC is just a comparator, comparing a signal with a threshold. Comparators are also used in the MuPix prototypes to digitize the hit information. There is a large amount of different standards for digital signal transmission. In the following, the ones used in the telescope project are introduced.

TTL Signal Standard

The **T**ransistor-to-**T**ransistor-**L**ogic standard describes circuits of transistors and is subdivided into different classes. For the telescope, Low Voltage-TTL (LVTTL) is used. The supply voltage is 3.3 V and the switching threshold is 1.5 V, while the output voltage is 2.4 V.

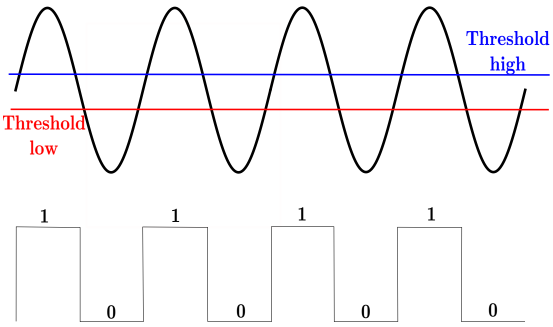

Figure 3.4: Analog to digital conversion

LVDS

The **L**ow **V**oltage **D**ifferential **S**ignaling (LVDS) is a standard for differential high data rates and the standard is defined by ANSI/TIA/EIA-644-A [40]. The idea is, that a transmitter creates a constant current of 3.5 mA. Depending on the logic level, this current flows from one to the other output and is terminated over a 100 Ω resistor at the receiver side. Depending on the current direction, this creates a voltage change of ± 350 mV on the receiver side. The 100 Ω termination fits the impedance of the transmission line and prevents reflections. In addition, the signal is very robust against cross talk and no net current is flowing, which prevents charging of components.

Fast NIM Standard

The **N**uclear **I**nstrumentation **S**tandard (NIM) was developed in 1964 for Nuclear and High energy physics and is defined by DOE/ER-0457T [41]. The logic zero is defined as a current of 0 A at 50 Ω. The logic 1 is defined as a current of -12 to –32 mA corresponding to -0.6 to -1.6 V at 50 Ω termination.

Chapter 4

Particle Track Reconstruction

Particle tracks can be reconstructed from particle hits in multiple detector layers. In the following chapter the used coordinate system, the track model and the track fits are described. The first technique is the straight line track assuming no scattering in the detector material which is a good approximation for relatively high particle momenta and therefore low multiple scattering. The main advantage is that this reconstruction method is very fast. A more complex track fit that takes correlations between the planes and the scattering uncertainty into account is explained at the end.

4.1 Coordinate System

A Cartesian coordinate system where the z-axis is parallel to the beam is chosen. The x and y axes are defined to be parallel to the columns and rows of the sensors, respectively. It is assumed that the telescope layers do not have any rotations relative to each other.

4.2 Track Model

The track model is a simple straight track defined by

$$\vec{x}(z) = \vec{x_0} + \vec{a} \cdot z, \tag{4.1}$$

where $\vec{x}(z)$ is a two dimensional vector, containing the x and y position as a function of the z position. $\vec{x_0}$ is the initial track offset and $\vec{a}$ is a constant two dimensional slope. In a more general matrix form this can be written as [42]

$$Y = \beta X, \tag{4.2}$$

with

$$\beta = (dx/dz, dy/dz, x_0, y_0)^{\mathrm{T}}$$

being the track parameters which have to be estimated and X is the propagator of the parameters to the measurement points, which can be represented in the following matrix form:

$$X = \begin{pmatrix} z & 0 & 1 & 0 \\ 0 & z & 0 & 1 \\ \vdots & \vdots & \vdots & \vdots \end{pmatrix} \tag{4.3}$$

$Y = (x_0,\ y_0,\ x_1,\ y_1, \dots)^{\mathrm{T}}$ are the hits on the telescope. In order to find the best estimate for the parameters, the weighted squared distance from the measurement points has to be minimized:

$$\mathcal{X}^2 = (Y - X\beta)^{\mathrm{T}}\, \Omega\, (Y - X\beta) \tag{4.4}$$

Ω is the weighting matrix, which has to be known.

The terminus $\mathcal{X}^2$ is usually used to describe the sum of the squared weighted residuals in physics even if this is not the mathematical correct term. Due to multiple scattering effects, which are ignored here, it is not expected that the statistics follow a $\mathcal{X}^2$ distribution for n degrees of freedom. Therefore it should not be used to estimate the fit uncertainties.

4.3 Straight Track Reconstruction without Multiple Scattering

If the effects of multiple scattering are ignored and the tracks are assumed to be perpendicular to the planes, the $\mathcal{X}^2$ reduces to

$$\mathcal{X}^2 = \sum_{i=1}^{n} \left(\frac{\left(x_i - (x_0 + a_x \cdot z_i)\right)^2}{\sigma^2_{x_{m_i}}} + \frac{\left(y_i - (y_0 + a_y \cdot z_i)\right)^2}{\sigma^2_{y_{m_i}}} \right), \tag{4.5}$$

with the measurement uncertainties $\sigma_{x_{m_i}} = pixel_{x_{length}}/\sqrt{12}$ and $\sigma_{y_{m_i}} = pixel_{y_{length}}/\sqrt{12}$ at each plane. This is equivalent to $\Omega = \mathbb{1}$. To get the best estimators, one can calculate the derivatives of equation 4.5 with respect to the track parameters

$$\begin{aligned}
\frac{\partial \mathcal{X}^2}{\partial x_0} &= \sum_{i=1}^{n} 2 \cdot \frac{x_i - (x_0 + a_x \cdot z_i)}{\sigma^2_{x_{m_i}}} \\
\frac{\partial \mathcal{X}^2}{\partial y_0} &= \sum_{i=1}^{n} 2 \cdot \frac{y_i - (y_0 + a_y \cdot z_i)}{\sigma^2_{y_{m_i}}} \\
\frac{\partial \mathcal{X}^2}{\partial a_x} &= \sum_{i=1}^{n} 2 \cdot z_i \cdot \frac{x_i - (x_0 + a_x \cdot z_i)}{\sigma^2_{x_{m_i}}} \\
\frac{\partial \mathcal{X}^2}{\partial a_y} &= \sum_{i=1}^{n} 2 \cdot z_i \cdot \frac{y_i - (y_0 + a_y \cdot z_i)}{\sigma^2_{y_{m_i}}}
\end{aligned} \tag{4.6}$$

and set those equations equal zero. Dividing by the constant pre-factors and rearranging leads to a set of normal equations that can be written in the following matrix form:

$$\begin{pmatrix} \sum_{i=1}^{n} x_i \\ \sum_{i=1}^{n} (x_i \cdot z_i) \\ \sum_{i=1}^{n} y_i \\ \sum_{i=1}^{n} (y_i \cdot z_i) \end{pmatrix} = \begin{pmatrix} \sum_{i=1}^{n} z_i & \sum_{i=1}^{n} 1 & 0 & 0 \\ \sum_{i=1}^{n} {z_i}^2 & \sum_{i=1}^{n} z_i & 0 & 0 \\ 0 & 0 & \sum_{i=1}^{n} z_i & \sum_{i=1}^{n} 1 \\ 0 & 0 & \sum_{i=1}^{n} {z_i}^2 & \sum_{i=1}^{n} z_i \end{pmatrix} \cdot \begin{pmatrix} a_x \\ x_0 \\ a_y \\ y_0 \end{pmatrix} \tag{4.7}$$

Inverting this matrix (see Appendix A) leads to analytic expressions for the estimated track parameters. Implementing those equations in C++ gives a fast and non iterative algorithm to reconstruct straight tracks at the expense of ignoring possible correlations.

Parameter Uncertainties

The fit uncertainty of a parameter p is defined over the second derivative of $\mathcal{X}^2$ [42]:

$$\frac{1}{\delta p^2} = \frac{1}{2} \frac{\partial^2 \mathcal{X}^2}{\partial p^2} \tag{4.8}$$

In the case of equation 4.5 those derivatives can be calculated analytically:

$$\sigma_{a_x}^{-2} = \frac{1}{2} \frac{\partial^2 \mathcal{X}^2}{\partial {a_x}^2} = \sum_{i=1}^{n} \frac{z_i^2}{\sigma^2_{x_i}} \tag{4.9}$$

$$\sigma_{x_0}^{-2} = \frac{1}{2} \frac{\partial^2 \mathcal{X}^2}{\partial {x_0}^2} = \sum_{i=1}^{n} \frac{1}{\sigma^2_{x_i}} \tag{4.10}$$

$$\sigma_{a_y}^{-2} = \frac{1}{2} \frac{\partial^2 \mathcal{X}^2}{\partial {a_y}^2} = \sum_{i=1}^{n} \frac{z_i^2}{\sigma^2_{y_i}} \tag{4.11}$$

$$\sigma_{y_0}^{-2} = \frac{1}{2} \frac{\partial^2 \mathcal{X}^2}{\partial {y_0}^2} = \sum_{i=1}^{n} \frac{1}{\sigma^2_{y_i}} \tag{4.12}$$

4.4 Straight Track Reconstruction with Correlations

The second implementation (implemented by M. Kiehn [43]) is again based on the straight track model, but also takes correlations between neighboring planes and multiple scattering into account. Starting from a reference plane one can propagate the uncertainties to the other layers. Therefore, the weighting matrix Ω is more complex:

$$\Omega = \begin{pmatrix} \mathrm{cov}_m(0) & 0 & \dots & 0 \\ 0 & \mathrm{cov}_m(1) & 0 & \vdots \\ \vdots & 0 & \ddots & 0 \\ 0 & 0 & 0 & \mathrm{cov}_m(n) \end{pmatrix} \tag{4.13}$$

In the above matrix, the $\mathrm{cov}_m(i)$ are the 2x2 uncertainty matrices at each plane, which are the sum of the propagated multiple scattering uncertainty and the local measurement uncertainty (for more details see Appendix A).

Minimizing the $\mathcal{X}^2$ can again be done by calculating the derivatives of $\mathcal{X}^2$ and setting them equal to zero [42]. This leads to the solution

$$\beta = (X^{\mathrm{T}}\Omega^{-1}X)^{-1}X^{\mathrm{T}}\Omega^{-1}Y, \tag{4.14}$$

which can be solved numerically. This needs more computational effort due to numerical matrix inversion and the iterative calculation the local measurement covariance matrices.

Part II

Setup & Measurements

Chapter 5

The MuPix Telescope

The MuPix telescope is discussed in this chapter in detail. The first part motivates the development and compares the telescope with existing ones. This is followed by an overview over the telescope concept. The components are introduced in the following starting with the mechanical setup. Subsequently the MuPix sensor is explained. The last part addresses the used electronics, focusing on a description of the customized PCBs.

5.1 Motivation

Particle tracking telescopes are developed as a tool for track reconstruction, especially at testbeam facilities and used to test the position and time resolution of detector prototypes. The two most actively used telescopes in Europe are the TimePix telescope at SPS at CERN and the EUDET telescope at DESY II at DESY. Both are individually customized for local beam properties. A comparison between those telescopes and the MuPix telescope is shown in Table 5.1.

The Timepix telescope uses bump bonded sensors and is therefore thick, while the MuPix and the EUDET telescope consist of MAPS, which are very thin but slow. The pixel sensor size varies from 18.4 µm for the EUDET to 80 µm for the MuPix telescope, resulting in a pointing resolution from 1.8 µm to 12 µm for 180 GeV pions. For low momentum particles, like 50 MeV electrons, the pointing resolution is 150 µm for the MuPix telescope, which is more precise than the others assuming 1 cm flight distance and dominating multiple scattering effects. The main advantage of the MuPix telescope is the high track rate of 20 MHz, which it is designed for.

The TimePix fits best the requirements of the beam at SPS and the EUDET for DESY II. For the high rate and low momentum beam at PSI, no customized pixel telescope exists. This is the reason why the MuPix telescope project was started.

	Timepix Telescope	EUDET Telescope	**HV-MAPS Telescope**
Pixel size	55 μm	18 4 μm	80 μm
Pointing resolution			
180 GeV π	2 μm	1 8 μm	12 μm
50 MeV e^{-} *	400 μm	180 μm	150 μm
Material	300 μm sensor	50 μm sensor	50 μm sensor
	700 μm readout	50 μm foil	25 μm Kapton
in radiation length	28 ‰	0.7 ‰	0.6 ‰
Time resolution	1 ns (in special plane)	112 5 μm	17 ns
	16 ms otherwise		
Frame rate	60 Hz	9 kHz	20 MHz
Maximum track rate	15.5 kHz	≈ 100 kHz	≈ 20 MHz
Track reconstruction	mostly offline	offline	online

Table 5.1: Comparison of the MuPix, Timepix and EUDET telescopes. The MuPix telescope is named HV-MAPS Telescope [44].

Another argument to build the telescope is to perform an integration test: The Mu3e experiment has a streaming readout providing absolute time information for all hits. Up to 2013, only single sensor standalone tests for the pixel sensors have been carried out. To scale up the system to a telescope with four planes is a perfect step towards a larger detector system.

5.2 Telescope Concept

The central idea of a particle tracking telescope is to detect the particle in multiple detector planes and reconstruct its track while minimizing the impact on the particle's track. The MuPix telescope is designed to track low momentum particles, where multiple Coulomb scattering is the dominating effect (compare Chapter 3.1) for the track resolution. Therefore the layers should be as thin as possible and only medium sized pixels are needed. The telescope consists of four layers of MuPix prototypes. An optional "device under test" (DUT) could be placed in the middle, but was neither used nor implemented in this thesis.
Figure 5.1 shows the four sensors layers, framed by two optional trigger scintillators, which can be used as a timing reference for the telescope.

The MuPix chips, thinable down to 50 μm are used as sensors. The sensors used in the measurements described in this thesis are between 250 and 300 μm thick. They are mounted either on a carrier (for the DESY T22 test beam, see Chapter 8), directly glued to a thinned PCB board (for the PSI test beam, see chapter 9) or glued on Kapton,

[*] Assuming 1 cm flight distance and dominating multiple scattering effects.

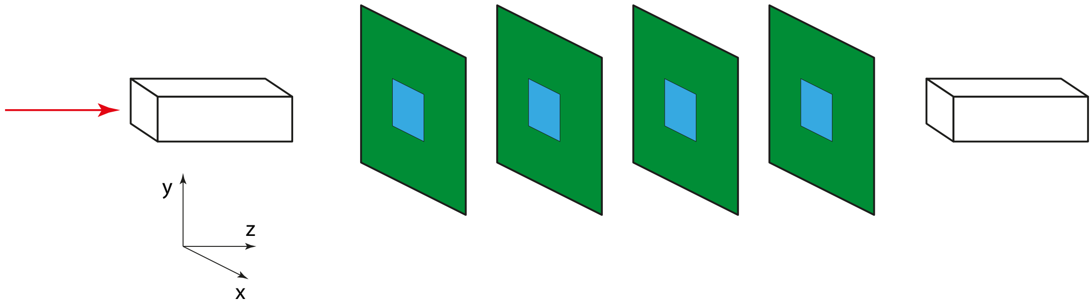

FIGURE 5.1: Design concept of the MuPix Telescope: In white, the two trigger scintillators are shown, framing the blue drawn MuPix chips, mounted on MuPix-PCBs drawn in green.

mounted on a perforated PCB. This results in a radiation length of 30 ‰ per layer for the chip on carrier and 2.5 ‰ for the chip on a thin board, respectively.
To readout the telescope a powerful computer, housing two Stratix IV FPGA development boards with one FPGA each, inserted in the PCIexpress ports of the mainboard and an Intel i7 **C**entral **P**rocessing **U**nit ("CPU") is used. It also contains an NVIDIA GForce **G**raphic **P**rocessing **U**nit ("GPU") and 16 GB **D**ouble **D**ata **R**ate 3 **S**ynchronous **D**ynamic **R**andom **A**ccess **M**emory ("DDR3-SDRAM"). A 256 GB **S**olide **S**tate **D**rive ("SSD") is used for operating system usage and 3x3 TB **H**ard **D**isk **D**rives ("HDD") serve as data storage volume.

Nomenclature

The connections of the test PCBs to the computer are organized as shown in Figure 5.2: The FPGA card mounted in the top PCIe slot is called TOP StratixDEVBoard, the lower one BOTTOM StratixDEVBoard. The **H**igh **S**peed **M**ezzanine **C**ard (HSMC) connectors A are used for readout and the connectors B for slow control. Each HSMC adapter card has two 40 line ribbon cable connectors, one at the back, called BACK and one at the front, called FRONT.

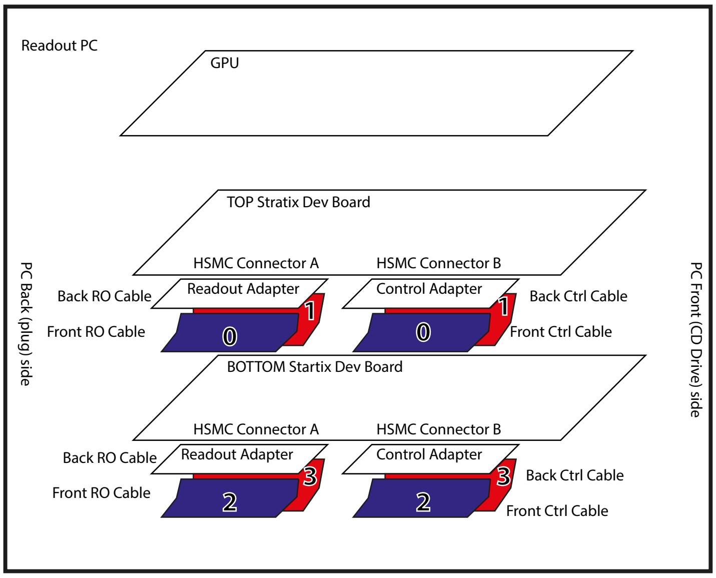

Figure 5.2: Scheme of the telescope PC side readout and control electronics.

5.3 Mechanics

The telescope is designed to be as stable and compact as possible. To realize this concept with maximal flexibility, optomechanical parts from Thorlabs are used for all components, except for the PCB holders which are self designed and constructed by the institute's workshop. The use of commercially available parts has the advantages of being cheap and easily replaceable in the case of mechanical failure, damage or activation after a testbeam. The system is placed on two parallel, 10 cm spaced, optical rails mounted on an optical breadboard with a size of 60x15 cm^2 as shown in Figure 5.3. Each sensor is mounted on a PCB holder which is connected to two stainless steel posts, which have the same spacing as the rails. Those posts are plugged into post holders, standing on rail clamps, which are connected to the rails and can be fixed via a screw. Due to this structure, the layers can be moved independently of each other on the rails. The second advantage of the use of two rails is, that the sensors can not be rotated relative to each other.

The minimal distance between two layers is given by the sum of the thickness of the thickest component on the MuPix boards on both sides and the PCB itself. In the current design, this leads to a minimal spacing of 2.5 cm between two layers. The minimal distance between two double layers, spaced 2.5 cm is roughly 8 cm in the

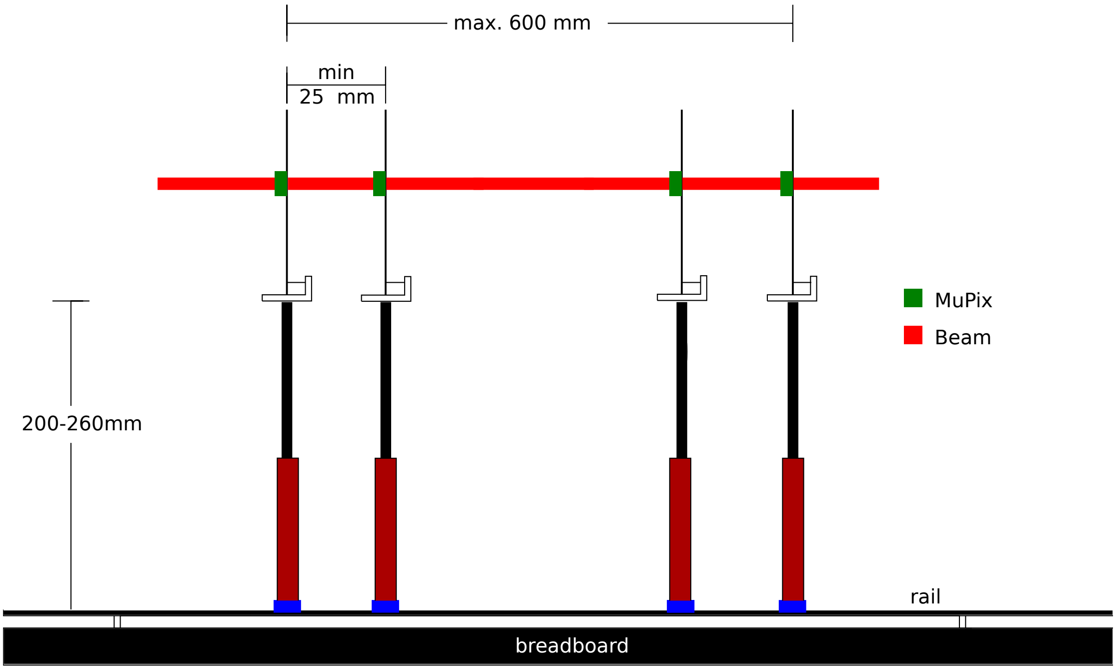

Figure 5.3: Overview over the mechanical structure of the telescope: The system is placed on an optical breadboard and the MuPix sensors are mounted on stainless steel posts, placed in post holders, colorord dark red. The postholders are mounted on a optical rail via rail clamps, drawn in blue, for maximal flexibility.

current setup. This is a result of the black fixation screws shown in Figure 5.4. To reach the minimal spacing, the screws have to point into opposite directions. This results in two screws touching each other, if two double planes are moved closely together.

A simple structure consisting of two posts and two cross studs are used as a stress relief for the readout and slow control ribbon cables. In principle the system can be extended by adding another breadboard and two rails, for larger DUTs or additional pixel layers.

5.3.1 PCB Holders

The PCB holders are the only non commercial parts and were built in house to fit the custom PCBs. Three different prototypes all consisting mainly of aluminum have been developed:
The first prototype was designed to mount the PCB on only one single post (see Figure 5.5a and 5.5b bottom). This prototype has the advantage of being mountable on a rotational stage, but the disadvantage of being unstable. It is not possible to fix the planes reliably. They are also unstable and start vibrating if the environment is vibrating. It is also complicated to align two of those holders without any rotation relative to each

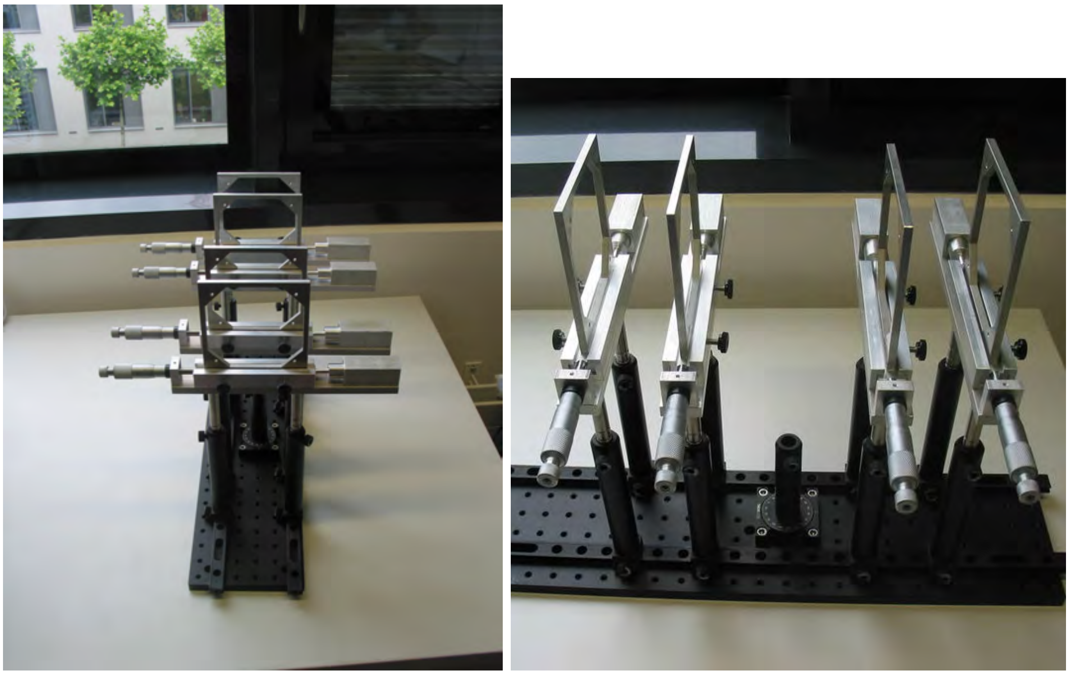

Figure 5.4: Front and side view of the MuPix telescope mechanics. The 60x15 cm^2 breadboard carries the two parallel optical rails, where the post holders are mounted on. The silver parts are the stainless steel post holders and the PCB holder version 3.

other.
Therefore, a second prototype (see Figure 5.5a and 5.5b top), similar to the first one, but mounted on two posts was designed. This prototype version improves the stability and is easier to align and was used at the DESY February 2014 test beam. However it has the disadvantage of not being movable horizontal to the beam, while the vertical direction can be adjusted by moving the posts in the holder up or down. The vertical alignments turned out to be very precise.

The problem of horizontal movement is solved by placing the PCB holder on an adjustable stage and is realized in the third prototype, which is also mounted on two steel posts and shown in Figure 5.5c. The position of the sensor can be adjusted with a micrometer screw, moving the PCB. A spring, placed in the aluminum cylincder on the right of Figure 5.5c provides the necessary back pressure. Screws vertical to the PCBs can be used to fix the setup. It is designed symmetrically to keep the center of mass between the two posts and not introduce any rotational tension in the mechanics. The second advantage is that the guide rail for the PCB frame can be turned around, which also moves the fixation screws to the other side. This makes it possible to deal with tight space constraints and gives the opportunity to move two planes very close together.

The aluminum plate carrying the components of PCB holder version 3 has a thickness of 2.5 cm. The total thickness, including the screws, is 4.2 cm. This could be reduced by a factor of two if needed.

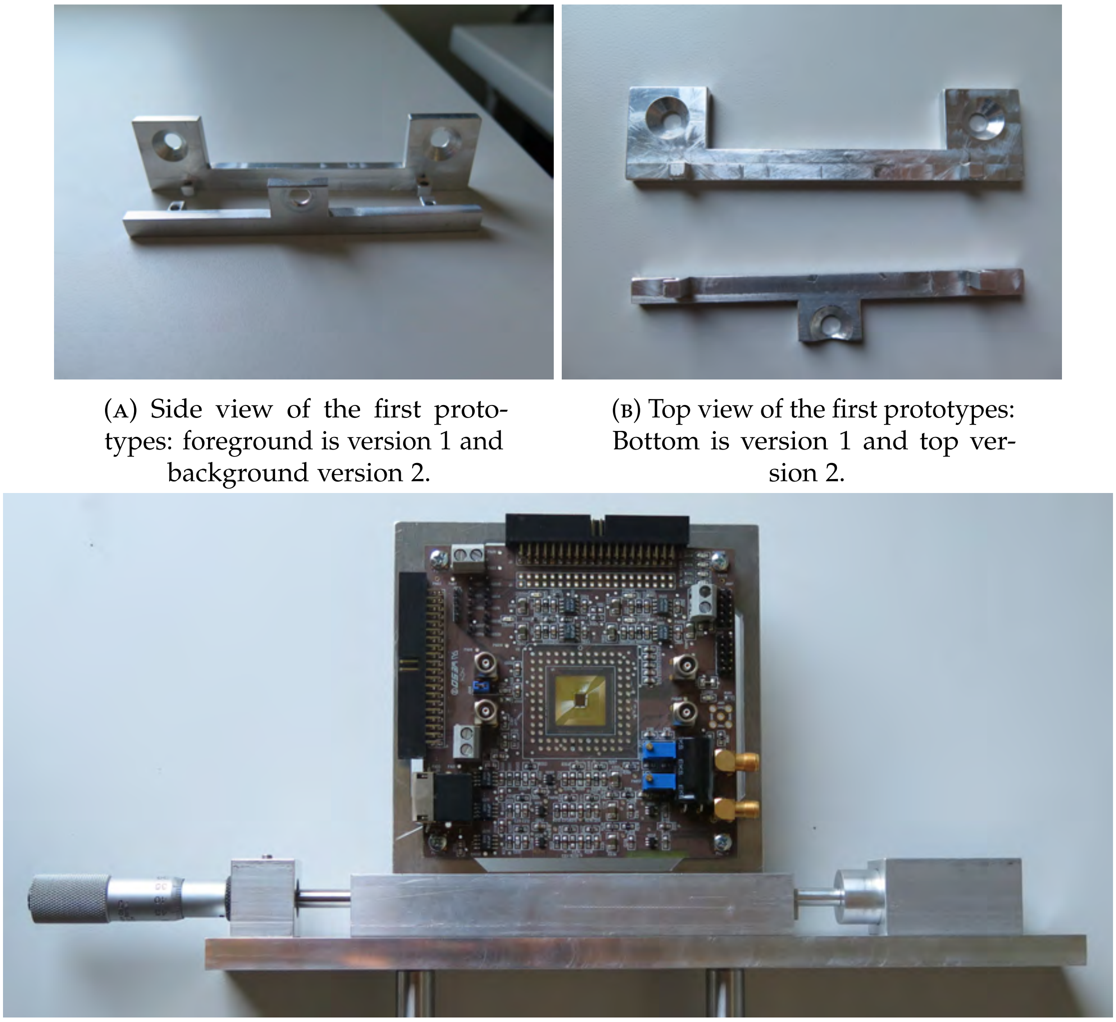

(A) Side view of the first prototypes: foreground is version 1 and background version 2.

(B) Top view of the first prototypes: Bottom is version 1 and top version 2.

(C) The third prototype with a MuPix test board and a MuPix4 chip glued on board. The micrometer screw on the bottom left is used to move the test board with a precision of 1 µm. The spring, inside an aluminum cylinder on the right side is used to create back pressure.

FIGURE 5.5: The three generations of PCB holder prototypes.

5.4 MuPix Prototypes

The Mu3e pixel sensor is currently under development. During this thesis, two prototypes, the MuPix4 and the MuPix6 were used as sensors for the telescope; their properties are compared in Table 5.2. Both have a fully digital readout mode, including a column and row address as well as a time information, the time stamp.

5.4.1 Sensor Electronics

The two prototypes have similar electronics, which are sketched in Figure 5.6. Each pixel has electronics, placed directly on the sensor:
The sensor itself is a diode. The charge deposited by a particle is integrated on capacitor

MuPix	Columns	Rows	Pixel width [µm]	Pixel height [µm]	area [mm^2]	active area [mm^2]	amplifier
4	32	40	92	80	14.72	9.22	single stage
6	32	40	103	80	16.18	10.55	double stage

TABLE 5.2: The MuPix prototypes used for the telescope.

and amplified by a charge sensitive amplifier (CSA). The amplified analog signal is sent via a source follower, that drives the high capacity of the signal line to the periphery. For the MuPix6 prototype a second amplification stage is located in the periphery. For both prototypes the signal is AC coupled via a CR filter to the baseline. This is done to decouple the charge signal from the other currents on the chip. At this point, the signal is also shaped [24]. A comparator compares now the voltage to a threshold. If it is above this threshold a digital output is created for the MuPix4. The MuPix6 signal is inverted in the second stage. Therefore the signal has to be below a certain threshold to create a digital output signal.

A tune DAC, which can be set for each pixel individually can be used to adjust the threshold of each pixel to compensate for fluctuations in the baseline between different pixel.

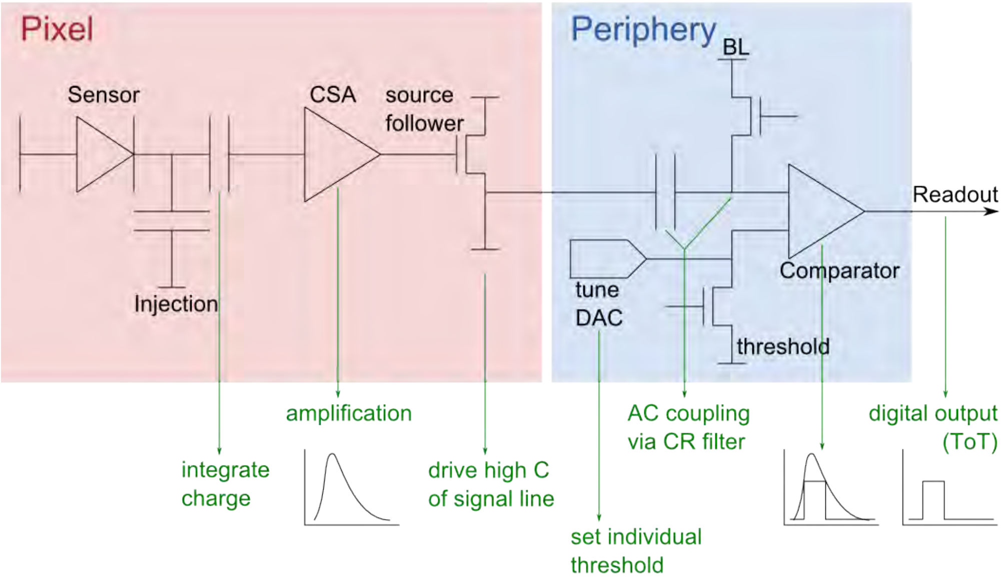

FIGURE 5.6: Schematic for signal generation on the MuPix prototypes [45].

In the pixel electronics an additional capacitor can be used to send a charge signal onto the pixel imitating the charge deposition by a particle. This is the injection signal and can be used to test and characterize the prototypes. For the MuPix prototypes, there are two different injections available, injection 1 and 2, which simulate particle hits in all even and odd double rows.

To adjust the performance of the prototypes it is possible to change the amplification of the CSAs, the driving force of the source follower and the signal shaping. This can be done by the use of digital to analog converters (DACs), which control the bias currents of the chip. The global threshold can also be set externally. Setting these DACs to appropriate values is crucial for the chip performance. A detailed study of the influences of those DACs for the MuPix4 is performed by a comparison of simulation and measurement [23, 46]. A list of the DAC settings used for the two sensors can be found in Appendix E.

5.4.2 Hit Storage

The digital output created by the comparator is sent to the next part of the digital electronics, where the hit information is created. Each pixel has its own readout cell in the digital part of the sensor, where the time stamp of each hit can be stored. For the MuPix4 and 6, this time stamp has 8 bits and has to be provided externally. If the comparator sends a signal, the time stamp is latched and stored. The latching of the time stamp is asynchronous to the switching frequency of the counter applied from the outside. Therefore it can happen, that the signals are switching while they are latched. This can result in wrong time information.

As long as the pixel is not read out, the pixel can not store additional hits and is blind until it is read out.

Gray Code

To prevent wrong time information, one can encode the counter, such that only one bit is switching at a time. This is the principle of the Gray Counter [47] and results in a reliable time information. In the worst case, the latched time is of by one in this case. One possible Gray Counter is the so called reflected binary code, which is chosen for the telescope project. One possible C++ implementation can be found in Appendix B.

5.4.3 MuPix Readout

The prototypes MuPix 4 and 6 need to be read out and controlled externally. This is done by an FPGA, which also sends the time information to the sensor. The firmware [44] includes a state machine, which performs the readout of the sensor. This state machine is shown in Figure 5.7 and works as follows: The FPGA's initial state is a wait state, that checks for the readmanual signal which is on if the readout sequence is sent

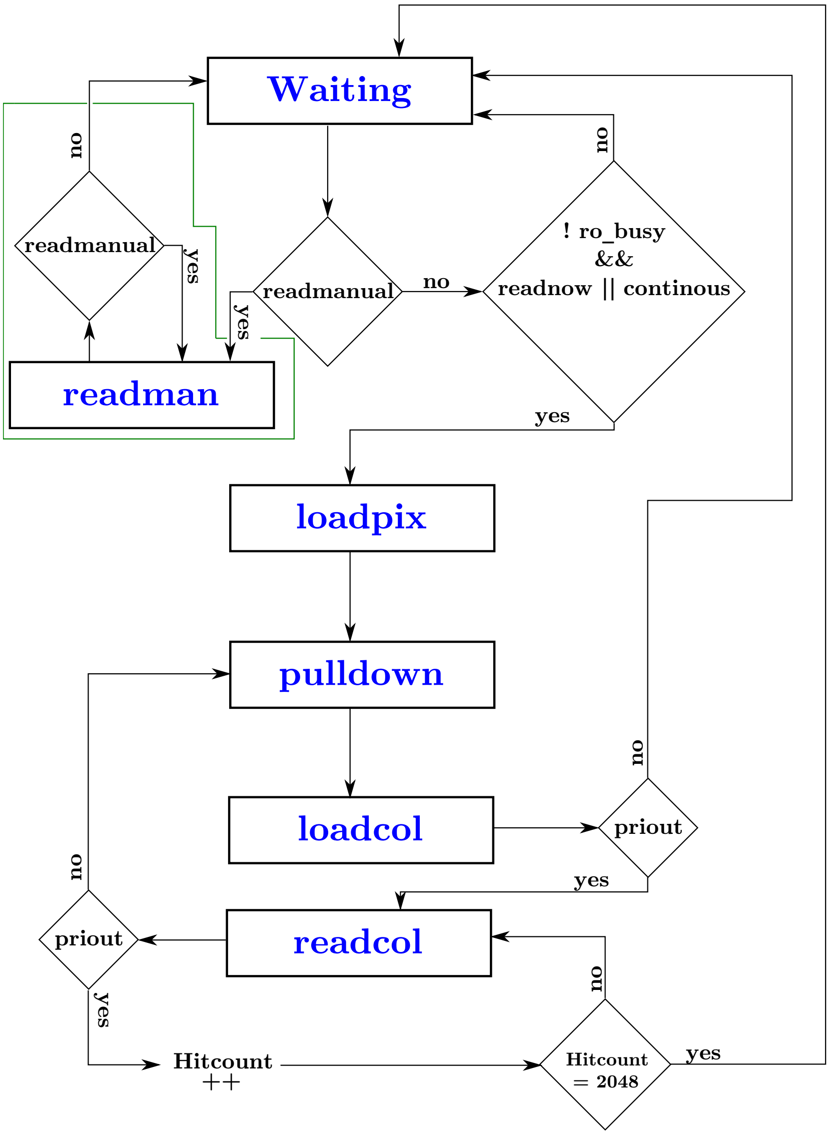

Figure 5.7: The FPGA state machine for the MuPix readout. The manual readout mode (framed green) is not used for performance runs, only for debugging.

in fixed time intervals set by the user. This readout mode is only used for debugging and is switched off for data taking. If the readmanual signal is off, the automatic readout mode is used. In this case the ro_ busy bit, indicating whether the FPGA is busy with other things, the readnow and the continuous readout signals are checked. If the ro_ busy signal is off and one of the others is on, a readout sequence is initialized: First, the loadpix signal is sent to the MuPix, that copies the hit information into the readout part of the digital logic. At this point the pixel itself is reset and sensitive again. In the next step a pulldown signal is emitted to initialize the readout bus. Now the loadcol signal is sent and the MuPix is loading the first hit from each logical column into the bus. If at least one hit is copied to the bus, the priout signal is emitted by the chip. If no hits are copied, the FPGA returns to the wait state. As long as the priout signal stays on, the FPGA sends readcol signals and one hit from the bus is sent to the FPGA. If the priout turns off, the FPGA goes to the pulldown state again. This procedure continues until all hits are read out, meaning the priout stays off or a number of 2048 hits (roughly twice the amount of pixels and named Hitcount in Figure 5.7) is read out. The FPGA writes the hit information in hit blocks into its local memory.

5.4.4 Special Characteristics of the Prototypes

The MuPix 4 has two main issues concerning the performance: First the row address of each odd double column is reset before it is read out. This effect is understood and removed in the MuPix 6 prototype. The second issue concerns the time stamps. Due to digital cross talk it is impossible to activate the time stamps in our test setup. In another setup the time stamps of the MuPix 4 are working. So this is introduced by the setup itself. This issue is also solved for the MuPix 6 prototype tests.

5.5 Electronics and Cabling

The MuPix sensor has to be read out and controlled by an FPGA to operate the telescope. Therefor, multiple customized PCBs and cables are used, which are introduced in the following. In Figure 5.8 the connections between the components are shown: The red lines from the PCBs (labeled 1, 2, 3 and 4), with the MuPix chips mounted represent the readout cables, which are connected over adapter cards to the HSMC (**H**igh **S**peed **M**ezzazine **C**ard) connector A. For the DESY testbeam, the readout is performed using flat ribbon cables and the HSMC readout adapter cards. Later the ribbon readout cables were replaced by SCSI III cables and the HSMC adapters by LVDS converter cards. The 40 lane flat ribbon slow control cables, shown in blue, connect to the FPGAs HSMC connector B via the control adapter cards with the sensors. The low voltage power supply, needed to operate the chip, the test board and the LVDS board electronics is connected to **S**ub**M**iniature version **A**("SMA") connectors via BNC cables. A HAMEG [48] power supply with four channels, one per sensor, is used to supply the system with 5 V at a maximum current of 750 mA (DESY testbeam). The current limit is set to protect the test board and the FPGA in case of a short. The Keithley [49] high voltage supply output is split and connected via four parallel cables to the chips, via another SMA connector on the test board. The HV lines are shown in purple in Figure 5.8, the low voltage lines are shown in green.

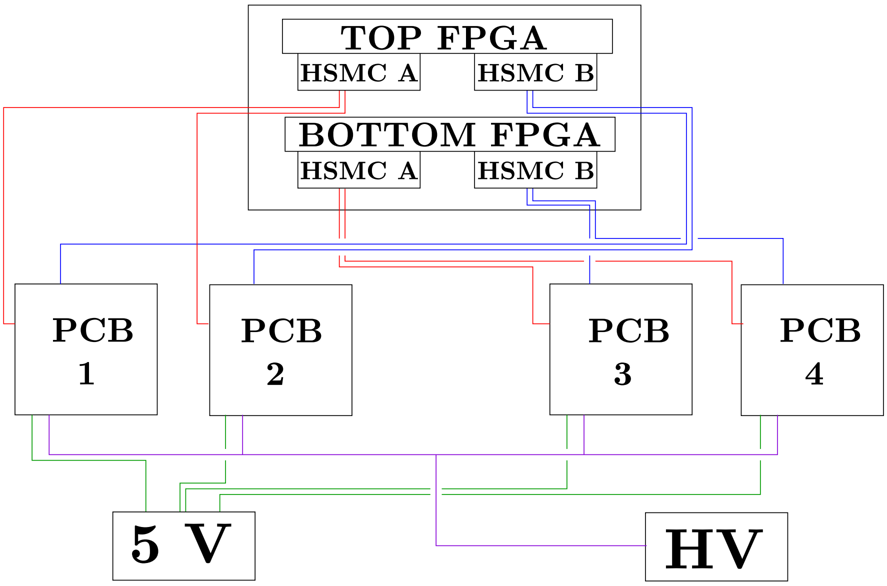

FIGURE 5.8: Schematic view of the readout hardware: The boxes 1 to 4 stand for the MuPix PCBs, the red lines represent the readout cables, the blue ones the slow control. The low voltage supply BNC cables ar shown in green and the HV supply lines in purple.

5.5.1 Stratix IV Development Board

Two Stratix IV development boards are used for the MuPix-Telescope. They have many connectors for maximum flexibility and easy detector readout and firmware development. A picture of the board is shown in Figure 5.9. For the telescope, the HSMC connectors A and B, framed in red in Figure 5.9 and the PCIe connector are used. The two HSMC adapters are used to control (HSMC B) and readout (HSMC A) the sensors. The PCIe port is used to connect the FPGA with the data acquisition computer. A picture of the FPGA with cards and cabling is shown in Figure 5.10c.

5.5.2 The MuPix Test Board

The MuPix prototypes need a support and test environment, providing the required power and connectors to readout and control the system. This is realized by a MuPix testboard [50], which is shown Figure 5.5, placed on the third PCB holder prototype. The MuPix prototypes are mounted in the center either glued on a carrier and placed in an IC socket or directly on the board and wire bonded to the PCB. It provides SMA connectors to apply low- and high voltage. A RJ45 port is installed for synchronization with the EUDET telescope. The luster terminals are used to get a good connection between the FPGAs and the test board ground. The testboard is equipped with several LEMO connectors to feed out the "Time-over-Threshold" signal for example. To drive

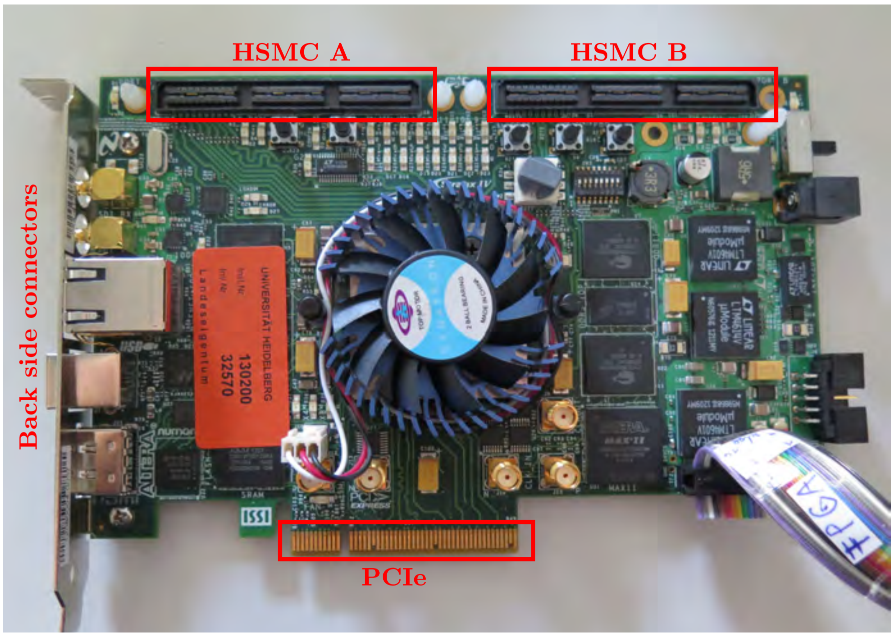

Figure 5.9: Picture of the Stratix IV development board. The HSMC and PCIe ports are highlighted. The FPGA itself is placed under the fan in the center. The ribbon cable in the bottom right corner is connected to a LCD showing debug information.

the signals over the ribbon cables, inverters can be used.
A more detailed description can be found in [22].

5.5.3 HSMC Adapter Cards

HSMC adapter cards serving as a bridge between the HSMC ports of the FPGA and the test board ribbon cables have been developed [50]. They are shown in Figures 5.10a and 5.10b. The connection to the HSMC port of the FPGA is on the bottom side. The two 40 pin plug connectors on the top side are used to plug in the ribbon cables from the MuPix test boards. The fast signals transported on those ribbon cables are terminated over a 150 Ω resistance to minimize reflections and cross talk and to maximize the signal quality. The fast signals are on different lines for the readout and slow control. This requires two different termination schemes.
On both sides of 40 pin connectors, a extra pin is reserved for grounding. The RJ45 connector on the card is not used for the MuPix telescope, but to interface to the EUDET telescope. The four LEMO-connectors can be used to feed in NIM standard trigger signals, which pass a NIM-TTL converter before they reach the HSMC port. The 20 pin connector, between the 40 pin connectors and the LEMO connectors, is used for FPGA synchronization.

5.5.4 LVDS Cards

To improve the signal quality and reduce digital crosstalk on the ribbon cables, two different cards with LVDS transmitters and receivers were developed [50]. These two cards are used foir the reaout of the sensors. Both need a 5V supply voltage and are interconnected by SCSI III cables. These cards are shown in Figure 5.11: The left card is the FPGA side LVDS card and replaces the HSMC readout adapter card. The FPGA LVDS card is similar to the HSMC card. The main differences are the additional transmitters and receivers to convert the TTL to LVDS signal and vice versa and the SCSI III adapters replacing the 40 pin plugs. On the PCB side, a new adapter card has to be plugged into the 40 pin readout connector, because no transmitters and receivers are available on the test board. This is the card shown on the right side in Figure 5.11. For debugging the time over threshold signal can be connected from the MuPix board over a LEMO cable and is also transmitted via LVDS to the FPGA. The power is supplied through an SMA adapter and is provided by another HAMEG power supply. The SCSI III cables have twisted pair lines for each LVDS signal pair and shielding. The ground is connected directly over the stainless steel connector and the shielding of the cable.

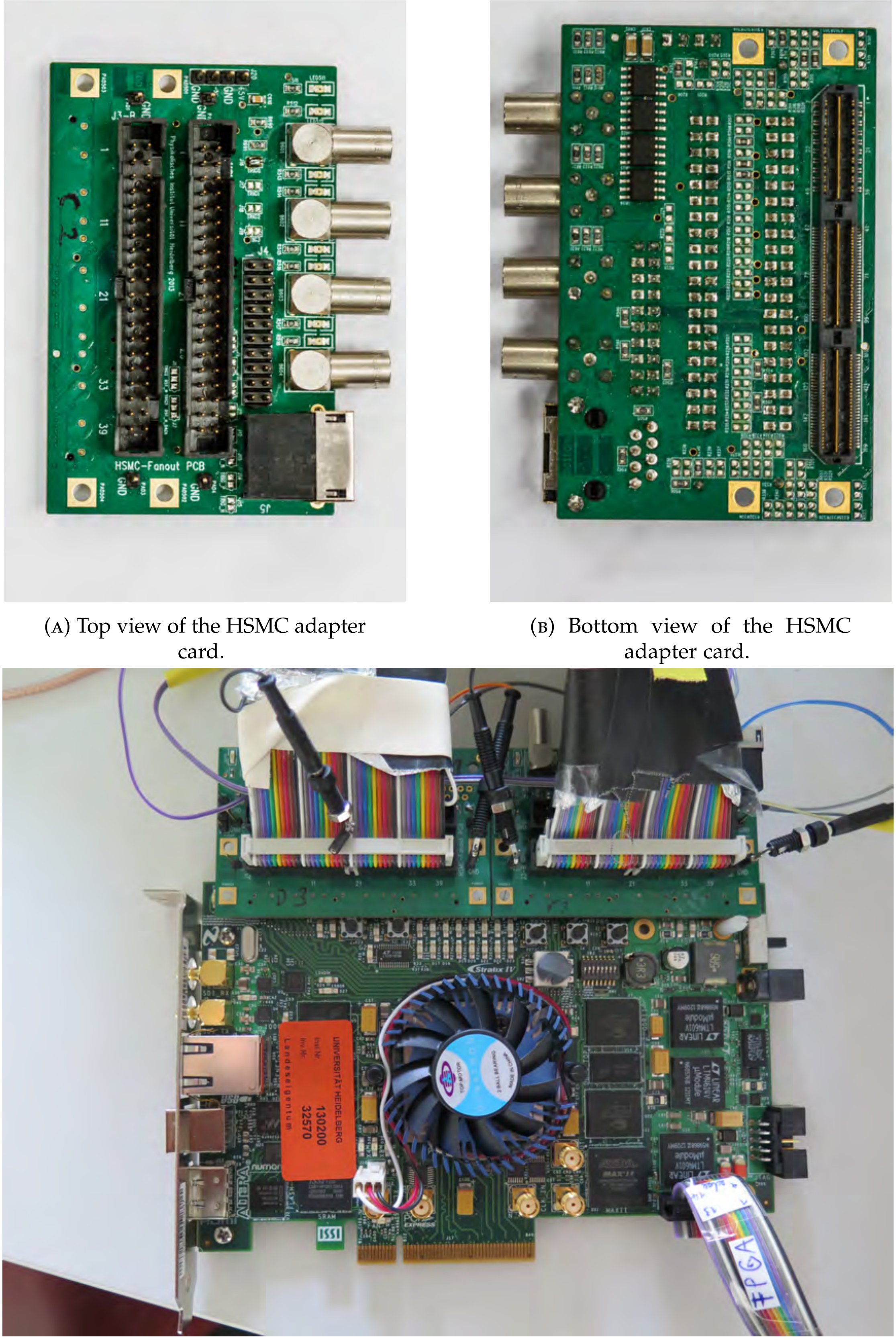

(A) Top view of the HSMC adapter card.

(B) Bottom view of the HSMC adapter card.

(C) Picture of the Statix IV development board with the two HSMC adapter cards mounted and 2 pluged in ribbon cables.

FIGURE 5.10: Pictures of HSMC adapter cards.

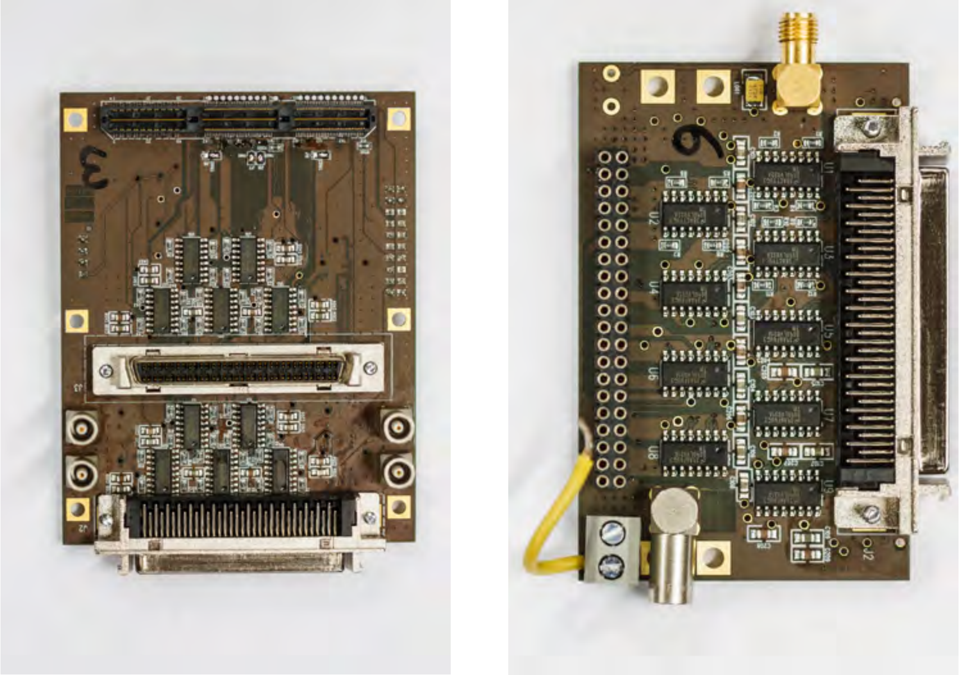

(A) FPGA side LVDS card.

(B) Test board side LVDS card.

FIGURE 5.11: LVDS readout adapter cards.

Chapter 6

Data Acquisition

The data acquisition system ("DAQ") system is a central part of the telescope and consists of different stages, which are introduced in the following, starting with an overview of the concept. This is followed by a description of the data taking and the data format generated by the FPGA. Afterwards, the generation of the time information and the sychronization of the FPGAs is addressed. Subsequently the data acquisition, data processing and storage in the readout computer is introduced. At the end the graphical user interface ("GUI") and the online monitoring are discussed.

6.1 DAQ-Concept

The telescope's DAQ is based on two FPGAs reading out and controlling two sensors each. The FPGAs are plugged into one powerful computer, which has to control the FPGAs and processes and stores the incoming data. This readout chain concept is shown in Figure 6.1.

To access the control and readout functions and monitor the telescope hardware components in a user friendly manner, a software providing a graphical access to the system, the graphical user interface ("GUI") has been developed and is described in more detail later.

The telescope is operating in a pull request mode meaning that the CPU asks the FPGA for new data. In order to reach the proposed performance of the telescope (compare Table 5.1), the system has to be able to handle high data rates. Therefore the readout software, running on the CPU, uses concurrent programming to optimize the processing speed.

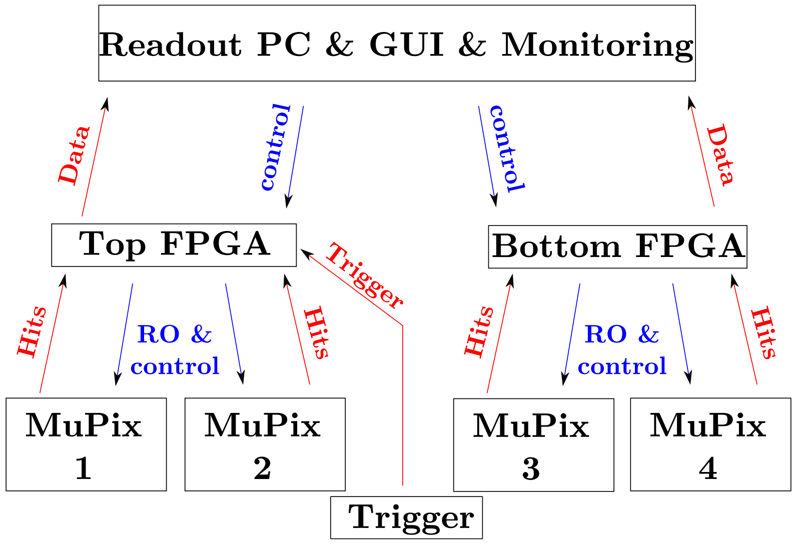

Figure 6.1: Conceptual drawing of the Telescope DAQ system readout chain. The blue arrows represent the control information, while the red arrows represent the data stream.

6.2 Telescope Readout Firmware

In operation each FPGA is reading out two sensors, while it also buffers the time information of incoming triggers. Therefore the firmware uses two identical state machines (compare Section 5.4.3) reading out both sensors in parallel. After finishing one loop in the readout state machine the FPGA creates a hit data block and writes it into its local memory. This hit block can contain hits from both sensors. If no hits are read out, a hit block without any hits is created. In the next step, the FPGA checks if any trigger arrived at the trigger input during the last sensor readout cycle. If this is the case, a trigger block is created and written into the memory. Both blocks contain an absolute time information corresponding to a 48 bit counter. The time information consists of the coarse counter and time stamp. The exact data structure is shown below. After finishing this readout cycle a register value is changed to indicate the last written point in memory. A new readout cycle is started immediately without waiting for the other FPGA to finish its readout. This results in an continuous readout of the sensors which can be asynchronous. The hit and trigger blocks have to be copied to the readout computer local memory and processed.

Readout Timing

4 m long cables and the delays due to the electronics between the FPGA and the MuPix sensor put strict requirements on the minimal wait time between two signals emitted

by the FPGA to ensure that the sensor has enough time to react to the signals. Also the sampling point of the firmware has to be chosen with respect to these delays. In addition the signals have to be applied long enough to drive the capacity of the cables and create the required switching voltages. Therefor the delays and signal length are set to conservative, fixed number of clock cycles in the case of the DESY testbeam. A more detailed study of the the timing of the signals was carried out between the testbeams [24]. Therefore the FPGA firmware was changed and the delays and signal length can be adjusted now. A summary of the timings used can be found in the Appendix D.

Data Structure

The data written to the memory is encoded in unsigned 32 bit words. Fixed pattern words are used to mark the beginning and end of a block. The data structure of the hit block is described in Table 6.1 for the DESY tesbeam data. For the PSI testbeam, the full 48 bit counter is stored using the least significant 17 bits from the second header word ("Hit block counter"). The trigger block structure is shown in Table 6.2.

Word offset	Value	Comment
0	0xFABEABBA	Beginning of hit block marker
1	Hit block counter	Crosscheck for blocks loss
2	Coarse counter	Number of times the 8 bit Graycounter has overflown
3	ChipMarker<12>	N Hits
	Column<6> Row<6> Time<8>	Hit address and fine time
N + 2	0xBEEFBEEF	End of hit block marker

Table 6.1: FPGA hit-block Structure for the DESY testbeam: All hits and information are stored in unsigned 32 bit integer values. The first and last elements are used to mark the beginning and end of a block. The Chip Markers are used to distinguish between the different sensor layers in the software.

Word offset	Value	Comment
0	0xCAFECAFE	Beginning of trigger block marker
1	Trigger block counter	Crosscheck for blocks lost
2	Coarse counter	2.5 ns counter, bits 47 down to 24
3	Trigger fine counter	2.5 ns counter, bits 23 down to 0
2·N + 1	0xCAFEBABE	End of trigger block marker

Table 6.2: FPGA trigger-block Structure: Each trigger is stored in two words; a fine counter and the coarse counter. The first and last block elements are the markers to distinguish between trigger and hit blocks.

6.3 FPGA Time Information and Synchronization

The FPGA is not only delivering the readout signals for the MuPix prototype, but also provides the required time information. Therefore the two FPGAs need the same absolute time information.

Each FPGA requires a 50 MHz clock, which can be applied externally or internally. The phase of this core clock passes a phase-locked loop ("PLL", dark green in Figure 6.3b). This clock is used for two different purposes. First it serves as a core clock, which is required to run the sensor readout. It is also multiplied in a clock multiplier to 400 MHz, the fast clock (the green block in Figure 6.3b).

Time Information

The fast clock is used to count a 48 bit counter up each cycle. This counter serves as absolute time information. One can select 8 consecutive bits from the lower 24 bits and use them as the time stamp counter and sent it gray encoded to the chip. In each hit block, the complete counter is written in the header. The trigger information in the trigger blocks is also this counter.

The absolute time information of a hit is split up into two parts. The least significant 8 bits are represented by the time stamp. Due to the changeable time stamp frequency it is required to know which 8 bits from the 48 bit counter are used. This meta information, the so called division factor (TSDF), is not changed over a run and stored in the header of the data file.

The 48 bit counter in each hit block is sampled at the beginning of a readout cycle. In order to extract the coarse counter, which give the rough time information, only the bits higher as the most significant time stamp bit are used. This selection methods is sketched in Figure 6.2

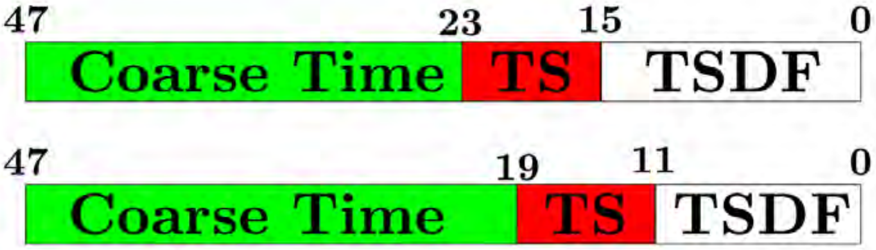

FIGURE 6.2: Schematic of the selection of time stamp (TS), the influence of the division factor and definition of the coarse counter. The upper top sketch shows the situation for the maximum division factor and the bottom one the situation for a division factor of 12.

Combining the coarse time with the time stamps lead to the absolute time information of each hit which is defined as

$$t = 2.5\ \text{ns} \cdot \left((\text{Coarse time}) << (\text{TSDF} + 8) + (\text{time stamp}) << \text{TSDF} \right). \qquad (6.1)$$

For the DESY testbeam, this was not implemented and a simple 32 bit coarse counter, counting the overflows of the 8 bit 20 MHz time stamps is used as absolute time information.

Synchronization

Due to the asynchronous readout state machines on the two FPGAs it important that both FPGAs have the same absolute time information and use the same clock. Therefor two different clocking schemes can be used:
The simple clocking scheme uses the internal 50 MHz oscillator of the master FPGA as clock. The clock is directly sent to an output of the master FPGA on the control HSMC adapter card and sent over a cable to an input on the control HSMC adapter card on the slave FPGA. In this case the slave FPGA uses the external clock. This is shown in Figure 6.3a and will only keep the clock phase difference constant for both FPGAs. A small offset or different relative phases will occur due to the cable connection.
The second possibility is, as shown in Figure 6.3b, to send the 50 MHz oscillator clock of the master FPGA to two outputs and loop it over two cables with the same length back to the inputs on both FPGAs. This leads to synchronized clocks with the same phase.

In addition a synchronous reset of the time counters is needed. This is realized in the same way as the clock synchronization: Writing a register value triggers a signal on the master FPGA, which is split and connected to two output pins on the HSMC readout adapter cards. Cables with equal length guide the signal to an input on each HSMC control adapter cards and trigger the reset synchronously.

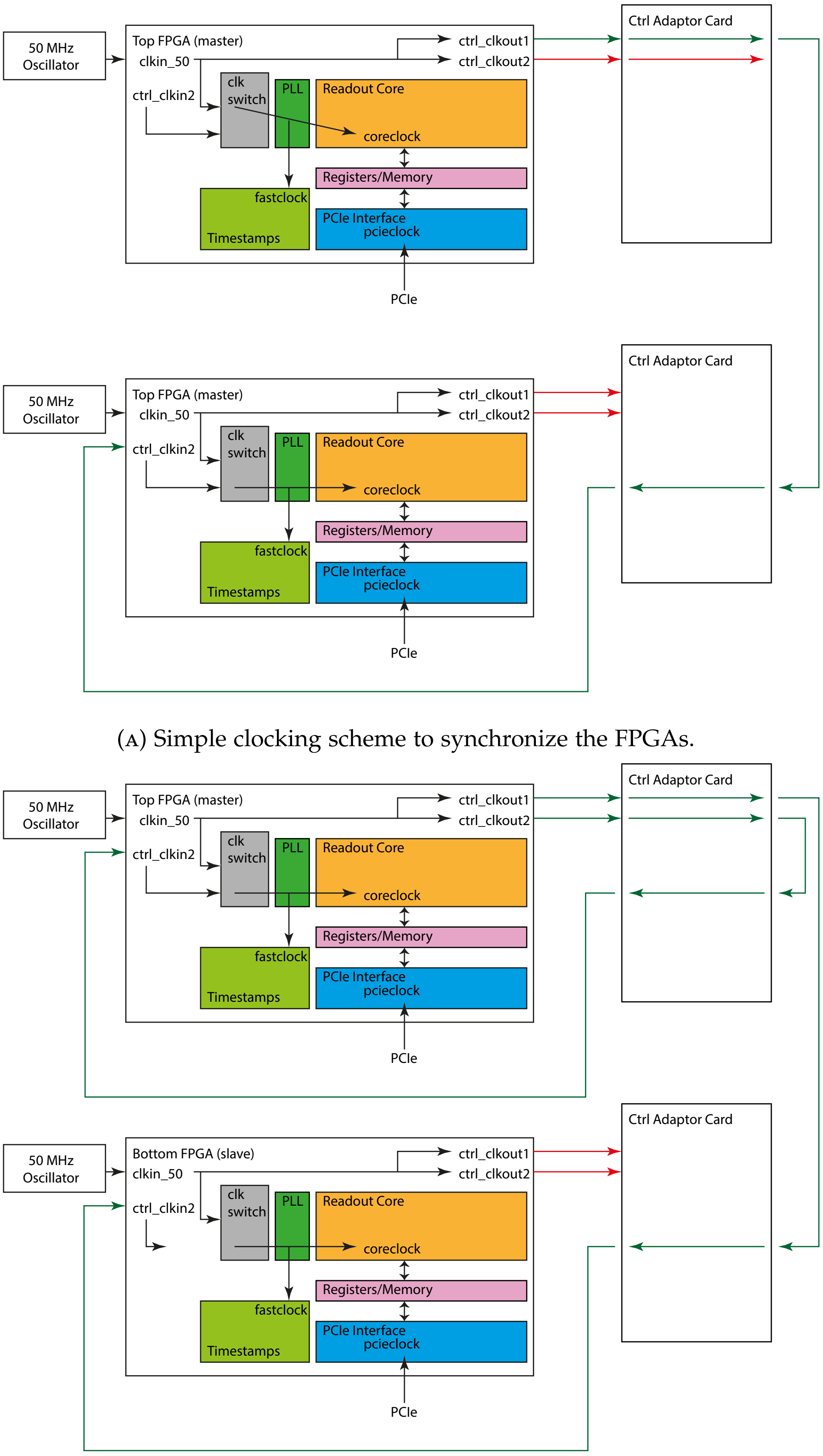

(A) Simple clocking scheme to synchronize the FPGAs.

(B) Clocking scheme to synchronize the FPGAs and run in phase.

FIGURE 6.3: FPGA clocking schemes. The green arrows indicate the used connections, while the red arrows represent signal which are not used.

6.4 Readout Software

The readout software consists of the software readout chain, the graphical user interface and the monitoring. It is realized in C++ and uses the Qt-libraries [51], the boost library [52] and the json library [53].

The software readout chain is used to copy the data provided by the two FPGAs to the local memory, process the data and write the final data stream to disk.
It consists of several stages: The first stage is a PCIe driver for the FPGA [43], which maps the registers and the memories to the local RAM.
The second stage is the telescope readout program. This program requires high computational power and can not be realized using only one core. In order to use the complete computational power available on the 6 core readout PCs, concurrent programming is used. Several threads run in parallel and can be executed asynchronously, without waiting for each other. The telescope readout program consists of seven threads controlling, processing, converting and writing the hits/trigger into a file. The thread structure and the data flow is shown in Figure 6.4: The memory is read out by a separate thread for each FPGA, the so called ReadOutThread, labeled ROT (**R**ead**O**utThread **T**op) and ROB (**R**ead**O**utThread **B**ottom) in Figure 6.4. The data are then processed by two other threads, the DataProcessingThreads, labeled as DPT (**D**ata**P**rocessingThread **T**op) and DPB (**D**ata**P**rocessingThread **B**ottom) in Figure 6.4. Then it is passed to the FileWriterThread, that writes the data to a file and passes the data to the monitoring thread, where the online monitrong is performed and the data are deleted from the RAM.
All threads are controlled and organized by the MainWindow, which also provides the GUI.

The threads are executed asynchronously and have to communicate and exchange data. This has to be realized in a threadsafe way, ensuring no memory used by a thread is overwritten by another one. The controlling of threads can be realized with signal-slot connections, while the data exchange is realized with threadsafe queues.

Thread Control

The principle of signals and slots provides a safe way to communicate between threads. A signal can be changed and sent by one thread and recognized by another one at a corresponding slot. This communication is implemented in the Qt thread class and well understood and stable. This makes it fairly simple to exchange information and control threads from another thread. The drawback of this method is that it is based

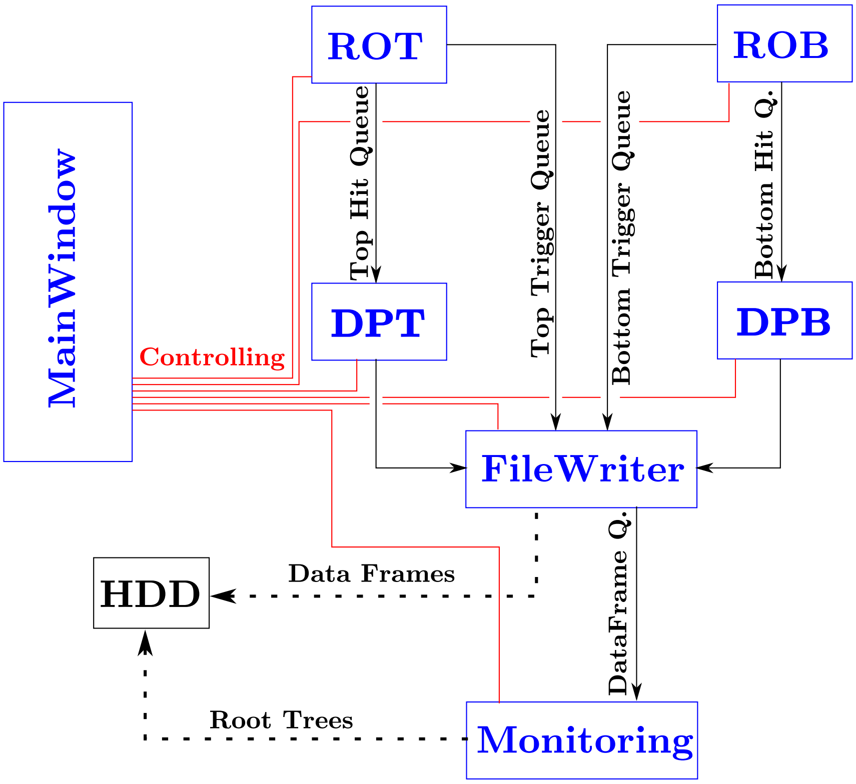

FIGURE 6.4: Schematic view of the DAQ software: The blue boxes represent the threads. The black arrows show the different vector queues, needed to pipeline the data through the system. The MainWindow thread starts, stops and controls the other threads. The black dashed arrows show the final data streams, which are stored on hard disk drives ("HDD").

on an event loop structure and is very slow, which makes it useless for high rate data exchange.

Threadsafe Data Exchange

A data stream between two threads is best realized by using queues with a single producer and a single consumer ("spsc"). The chosen queue template is the boost lockfree threadsafe spsc fifo queue. This queue has the needed specifications, is thread safe and due to the lockfree architecture very fast. The queue is realized as a ring buffer and the first element written ("pushed") is the first one that is read ("pulled"). The disadvantage is that there is no possibility to check how many events are in the queue, or if the producer overwrites the ring buffer before the data is read by the consumer. This can lead to a memory leakage if the queue is filled with pointer.

6.4.1 Threads:

In the following, the threads running in the software readout are explained in more detail:

- **MainWindow:** This thread controls the complete system. Here, all threads are started, controlled and stopped. In addition, it is used as central GUI and creates the MainWindow, shown in Figure 6.5. It also communicates with the two FPGAs and starts and stops the readout procedure. The communication with the FPGA happens via the mapped register. A complete table of entries in those registers can be found in Appendix D.

- **ReadOutThreads:** The readout threads (ROT and ROB in Figure 6.4) are used to read the FPGA memory. Therefore, the last written memory register value in the FPGA is checked. If this value changes (it is always incremented by the FPGA after one event is read out), a data block from the old last position to the new last memory position that was written is copied to a buffer. The buffer is then sorted into hit block- and trigger block-vectors (data structure compare Table 6.2 and 6.1). These vectors are pushed into two queues. The hit queue is sent to the data processing thread.

- **DataProcessingThread:** This thread takes the hit vectors from the readout thread and pipelines them to the FileWriter. It also takes the vectors and converts the unsigned 32bit integer words into hits with a x,y and z component and fills the hitmaps, that are directly available in the MainWindow Top Menu Bar. Therefore, the column and row addresses have to be converted from the logical to the physical layer (Conversion schemes for the two prototypes see Appendix C). The incoming trigger blocks are converted to unsigned 64 bit numbers containing the complete time information and pushed into a queue.

- **FileWriteThread:** The FileWriter creates the telescope frames consisting of time slices with the complete hit and meta information. It fetches the two trigger queues from the readout threads and deletes the bottom trigger queue, because it is not used. The bottom trigger queue has to be piped through, because the code of both readout threads is the same. It also fetches the hits from the data processing thread. The FileWriter looks at the coarse counter time information of the first element of the three queues and takes the lowest absolute time as a reference. All hits with the same coarse time information are added to a data block. To add all corresponding triggers, the highest absolute time of the hits (coarse time plus time stamp) is calculated and all triggers with a earlier time are added to the frame. This procedure ensures, that the incoming triggers are stored in the correct frames.

  For each frame, a header containing the length in 32 bit words and a checksum (boost crc32) is created. The complete frame is now dumped into a binary data file. A copy of the frame can be written into a queue and sent to the monitoring. The fraction of frames sent can be adapted to the data rate in order not to overload the monitoring.

- **MonitoringThread:** The MonitoringThread creates the online monitoring plots using the frames provided by the FileWriteThread and stores them in a ROOT [54] histogram file. In addition a postscript file containing the most relevant information is created after a user defined time interval. The default time interval is set to 20 seconds. Optionally it is possible to do an additional pre-selection of all events in order to filter out hot pixels and select events with hits in all four layers for further tracking. This pre-selection does not change or influence the raw data stream.
  The pre-selection is implemented but not used for the measurements during this thesis, because it only makes sense to use this pre-selection if one reconstructs the tracks directly online.

6.5 The MainWindow

The MainWindow is the graphical user interface for the MuPix-telescope and shown in Figure 6.5. In the version developed so far, many debug features are implemented. To perform the actual readout, only the "User friendly Testbeam Control and ReadOut" is needed. In the following, all buttons and their functions are introduced:

Top Menu Bar

- *FPGA*: Option bar to display the memory and register windows, which are used to check the memory or write register values by hand.
- *DACs*: Opens the windows for the chip and board DACs, where the values can be changed for each sensor.
- *Hitmaps*: This option displays the hitmaps of the 4 sensor layers.

Resets

- *Reset Event Counter*: This button resets the event counter that can be used as an offline crosscheck in the data stream.
- *Global Reset*: Sets all FPGA register values to their default values.
- *Reset Hitmap*: Sets the hitmaps to zero in the separate hitmap window.

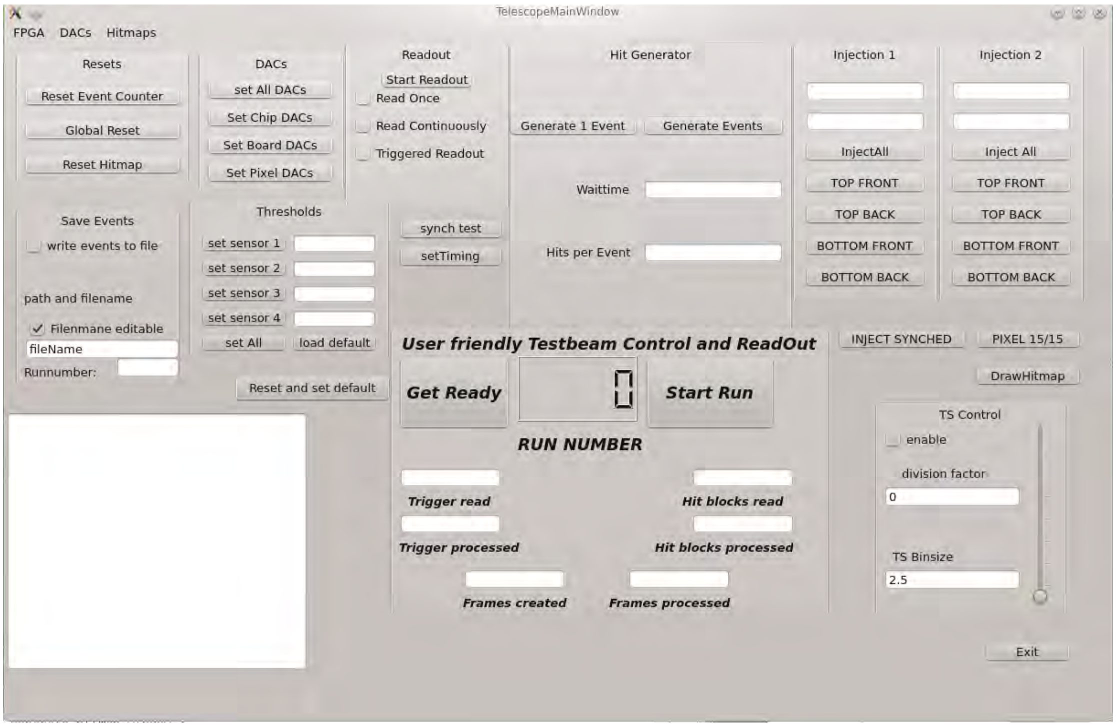

☑ Filenmane editable
path and filename: fileName
division factor: 0
TS Binsize: 2.5

Figure 6.5: Schematic view of the MainWindow.

DACs

This block is used to set the global DAC values for the four sensors, described in Section 5.4. The values of all DACs are displayed in the separate DAC windows, accessible over the Top Bar.

Readout

This block is the central one of the main window. One can choose between *Read Once*, *Readout Continuously* and *Triggered Readout*:

- *Read Once*: This option activates a single readout. All sensors are read out once.
- *Read Continuously*: This option activates a continuous readout. In this case the FPGA reads out its two sensors continuously.
- *Triggered Readout*: This option would trigger a single readout after a trigger is activated. This readout mode is not used, because neither an external trigger system was available, nor needed.

Hit Generator

This module can be used to generate hits on the FPGA and read them out directly in order to test the performance of the DAQ system. One can choose between a single event creation with a selectable number of hits or a continuous event generation at selectable time intervals and hits. This generator can be used to debug the software without using real sensors. This has the advantage of removing all issues concerning the sensor itself. This makes it easier to detect software issues.

Injections

The Injection 1 and 2 can be used to inject signals to the chip simulating hits. Due to the chip design, Injection 1 addresses the odd double columns and Injection 2 the even double columns. The buttons *TOP FRONT, TOP BACK, BOTTOM BACK* and *BOTTOM FRONT* inject the signals into the different telescope layers with the strength and length set in the white input fields above. The *injectAll* button can be used to inject the charge pulse of both injections to all four layers.

Save Events

The save events block is used to control the file writing mode: One can select by marking the *write events to file* check box if the data taken with the telescope should be written to a file. In the white line in the center, the file-path and name can be set. The run number displays the current run number. This function is only activated if test data is taken. For actual testbeam measurements the initial filename is hard coded and only a run number counts up to prevent accidental changes.

Thresholds

This block is used to get direct access to the global thresholds of the 4 sensors. The *load default* button loads the initial values, stored in the interface and displays them in the 4 input fields. With these fields, the values can be adjusted and set with the buttons left to the fields.

Message Display

The white area in the bottom left is used for displaying different messages, like errors during readout, run changes or DAC value changes. It also displays changes in the thread IDs, occurring wrong data structures and file changes.

User friendly Testbeam Control and ReadOut

This block is the central readout scheme for the use at testbeams. The *Get Ready* button initializes the readout by setting all DAC values, and resetting the absolute time counter.
The *Start Run* button starts all threads and activates the readout register for the FPGAs. After clicking, the label changes to *Stop Run* and clicking causes the stop of all threads and deactivates the FPGA readout. The threads are started before the FPGA starts reading out and the FPGA readout is stopped before the threads are stopped. This makes sure that all data taken are processed.
The *RUN NUMBER* display shows the current run number.
The other outputs in the bottom half of the block display the number of hits, frames and trigger blocks read and processed. The difference of "read" and "processed" should stay constant and at low numbers. Otherwise the DAQ system is too slow and the PC runs out of memory.

TS Control

The time stamp (TS) control is used to define the time stamp frequency and enables or disables them. The *division factor* and the corresponding *TS binsize* are displayed and can be changed with the slider. The time stamp is an 8bit Gray encoded counter running with a maximal frequency of 400 MHz, resulting in a minimal bin size of 2.5 ns. It can be divided by 2^n with n being smaller than 16 resulting in minimal frequency of roughly 6 kHz corresponding to 164 µs.

This block is not editable while the readout is activated.

Non-Grouped Icons

- *synch test*: Test icon to check whether the system is still running synchronously. The coarse counters of both FPGAs are displayed after clicking this icon.
- *setTiming*: Sets the default timing values again. This is included in the automatic readout.
- *INJECT SYNCHED*: Drives the injection signals from both FPGAs at the same time, which is not the case if one clicks on the other injection buttons.
- *PIXEL 15/15*: Not used for the telescope, can be used to debug the setup using the MuPix 4.
- *DrawHitmap*: Draw the hitmaps in the hitmap window.
- *Reset and set default*: Resets the settings and sets the default values again.

- *Exit*: Closes the GUI.

6.6 Online Monitoring

The online monitoring, performed by the MonitoringThread, uses ROOT to create all default monitoring plots. All plots are created for frames, provided from the FileWriter, there is no cross frame information available for the monitoring.

- **Hitmaps:** The hitmaps plot the number of hits per pixels in a 2D histogram. It can be used to check for changes in the sensor performance, for example the loss of DAC settings or hot pixels. For large enough beams, the sensor hitmaps should be uniformly filled.
- **Spatial Correlations:** Those Correlations are used to get a first overview of the alignment and performance. The correlations between row and row addresses of different sensor layers are expected to show a diagonal line as well as the column column address correlations. For correlations between rows and columns, so called cross correlations, one expects no lines at all - any line is a clear hint for a relative rotation of layers.
- **Timing:** The timing monitoring shows the time information from the different sensors. The time correlations are also plotted and should behave similar to the column column and row row correlations.

Chapter 7

Simulations

In order to validate the track reconstruction and compare the performance of the tracking methods, a simulation of the MuPix telescope has been developed. First the event generation method, the input parameter of the simulation and the track selection are discussed. Subsequently, the event generation and track reconstruction algorithms are validated, followed by a comparison of the two reconstruction methods. At the end the background acceptance and signal reconstruction efficiency are analyzed and optimal cut values are determined.

7.1 Event Generation

An event consists of two parts: Hits and noise. For the basic simulation it is assumed that the telescope planes are perfectly aligned, shifts and rotations of planes are set to zero. This could be adjusted for further studies. The beam profile is assumed to be homogeneous over the sensor, instead of the real Gaussian profile. This assumption is justified by the large distance of the telescope at the DESY to the beam window. This fans out the beam. At the PSI the beam is relatively expanded.
The starting point of each track is random (All random numbers are generated with the ROOT random generator TRandom3 [54]) and the initial flight direction is defined to be perpendicular to the first telescope plane. At each layer, the particle's flight direction is changed by a random scattering in the x and y plane. The RMS of the mean plane scattering angle Θ_{MS} at each layer is defined by the following formula [1]:

$$\Theta_{MS} = \frac{13.6\text{MeV}}{\beta c p} z \sqrt{\frac{x}{X_0}} \left(1 + 0.038 \ln \frac{x}{X_0}\right). \qquad (7.1)$$

Here, β is the fraction of speed of light c of the particle's speed, p the particle momentum, z the particle's charge magnitude and $\frac{x}{X_0}$ the sensor layer thickness in radiation lengths. To simulate the multiple scattering behavior, the scattering angle is calculated using random numbers drawn from a Gaussian distribution with a sigma of Θ_{MS} for the x and y direction. The thickness of each layer is assumed to be constant, the small changes due to non perpendicular crossing after the first scattering are neglected. The change in the particle's flight direction in x and y is described by:

$$\frac{dx}{dz}(\Theta_{MS}) = \tan(\Theta_{MS}) \tag{7.2}$$

$$\frac{dy}{dz}(\Theta_{MS}) = \tan(\Theta_{MS}) \tag{7.3}$$

Calculating the tangent of the two angles transforms the scattering angle into a change of flight direction, which is only a small correction for small angles. The new direction is propagated to the next layer, where another scattering is simulated. The propagation is visualized in Figure 7.1.

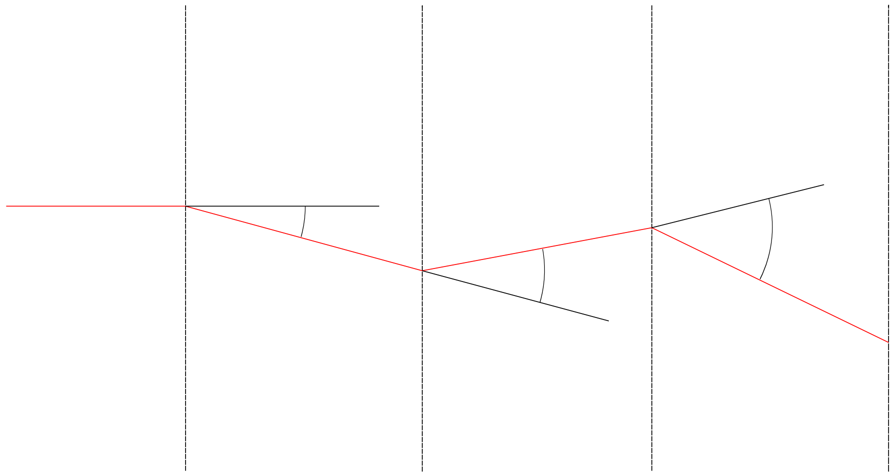

Figure 7.1: 1-dimensional track propagation. The three indicated angles represent the scattering at the relevant planes.

It is possible that a particle track is scattered out of the telescope acceptance. In this case, no track can be reconstructed due to a missing hit in one layer. The probability for such an event increases with a larger mean multiple scattering angle and smaller distances to the sensor edges. If such an incomplete track is created, it is directly thrown away and a new track is created. This leads to a larger run time for simulations with higher mean scattering angles and introduces a bias: The fact, that incomplete tracks are rejected reduces the fake track rate, because the probability to have one background hit combined to a track fit with three hits from an incomplete track is higher than having four background hits creating a valid track.

The background is generated on each plane separately by creating random hits on each plane, drawn from a uniform distribution.

At the DESY test beam facility, one expects only one track per frame. For the PSI beam, more than one track per frame can occur. The number of background hits also differs for the two areas: At DESY, the background activity is lower than at PSI. The probability to have a track, that do not pass all layers is also smaller at DESY than at PSI, due to the increased scattering. Therefore, the amount of background hits at PSI is expected to be higher. Additional background due to hot pixels only depends on the sensors and is not considered in the simulations.

The simulation needs some input parameters, which can be set freely:

- Maximum number of tracks per frame
- Maximum number of background hits per layer and frame
- Radiation length per sensor
- Sensor positions in initial direction of flight
- Particle momentum
- Particle mass
- Number of sensors

The used values for the following analysis are summarized in Table 7.1.

Name	Pixel matrix Col x Row	Pixel size [µm^2]	Z position s1 s1 [mm]	Z position s2 [mm]	Z position s3 [mm]	Z position s4 [mm]
DESY	32 x 40	92 x 80	0	75.5	150.5	226
PSI	32 x 40	103 x 80	0	35.9	109.3	142.6

Name	s1 scattering thickness [‰]	s2 scattering thickness [‰]	s3 scattering thickness [‰]	s4 scattering thickness [‰]	Particles & momentum
DESY	2.9	33.9	33.9	43.4	5 GeV e^-
PSI	2.5	2.5	2.5	2.5	250 MeV π^-

Table 7.1: Settings for the simulations performed.

The geometrical and the pixel sensor information are stored in configuration files which can be created or loaded from existing files. The particle characteristics have to be entered into the code or can be passed as arguments in a shell script.

7.2 Track Reconstruction Algorithm Structure

The track reconstruction is designed to run online, but is only implemented offline in this thesis:
The algorithm to reconstruct the tracks is divided in three stages: First the hot and noisy pixels have to be removed. The second step is the linking of hits to the tracks. The last step is to determine the right tracks.
The hot pixel removal is not required for the simulated data and is explained later. In order to reconstruct tracks, all hits are sorted in frames with the same time. The simulation directly creates these frames. For each frame, all possible combinations requiring one hit in each layer are selected. For every possibility the track fit is performed. The fitted tracks are then sorted by their $\mathcal{X}^2$ values. Now the fit with the lowest $\mathcal{X}^2$ is selected as the first track. The hits used for this track are locked and not used again, which assumes, that a pixel is only hit once per frame. Going through the list of fitted tracks, sorted by $\mathcal{X}^2$, tracks are selected as long as they do not use a hit from a previously selected track.

Estimation of Double Hits

The assumption that a pixel is not hit twice in one frame can be confirmed by looking at the probability to hit a pixel not more than one time, which is defined as

$$\begin{aligned} P(m,k) &= \frac{m!}{(m-k)! \cdot m^k} \\ P_{k=4} &= 99.53\% \end{aligned} \tag{7.4}$$

where m is the number of pixels and k is the number of hits per chip. It has to be mentioned, that the assumption of having 4 hits per layer is very conservative. The probability to hit a pixel twice ore more is given as

$$p = 1 - P(m,k) = 0.47\%. \tag{7.5}$$

The above numbers show, that the assumption of not hitting a pixel twice is justified. The final tracks are stored in a ROOT [54] tree containing all track parameters including the calculated errors and the hits corresponding to the track and the time information.

7.3 Validation of Event Generation

The functionality of the event generator is confirmed by an analysis of the generation itself. First, the homogeneity of the starting point is checked. The results are shown in Figure 7.2a and 7.2b. There is no structure visible, neither in the hitmaps nor in the projections. This homogeneous behavior is also expected for the other layers. Therefore, the other layers are also plotted and summarized in figures 7.2c, 7.2d ,7.2e, 7.2f, 7.2g and 7.2h. It is visible that the hits are homogeneously distributed over the sensors, as expected. The slightly smaller number of hits at the edge comes from the track generation, where hits in all four sensor layers are required.

The second crosscheck performed is the plot of the correlations between different layers, similar to the plots created by the online monitoring of the telescope. In Figure 7.3, the behavior of the correlations assuming the DESY testbeam characteristics (5 GeV electrons and the geometry from Table 7.1) and PSI characteristics (250 MeV pions and the geometry from Table 7.1) is shown:
The left column shows the DESY setup simulation, with less scattering and much higher particle momenta than the PSI setup simulation shown in the right column. The overall behavior is the same: More material in between two sensors leads to more scattering and a smeared out distribution. The irregular shape in the top right and bottom left corner is again caused by the way the tracks are generated. The second visible detail is the homogeneous background distribution. In the left column, there is no structure visible in the background distribution at all. In the right column, the central pixels have a slightly higher occupancy than the corner pixels. This is not due to in-homogeneous background creation, but due to stronger scattering, which suppresses tracks coming form the edge of the sensors. It is possible that the simulated particles scatter strongly and end up far away from their initial track. The probability of scattering away from the initial flight direction increases with each plane due to higher distances and more material.

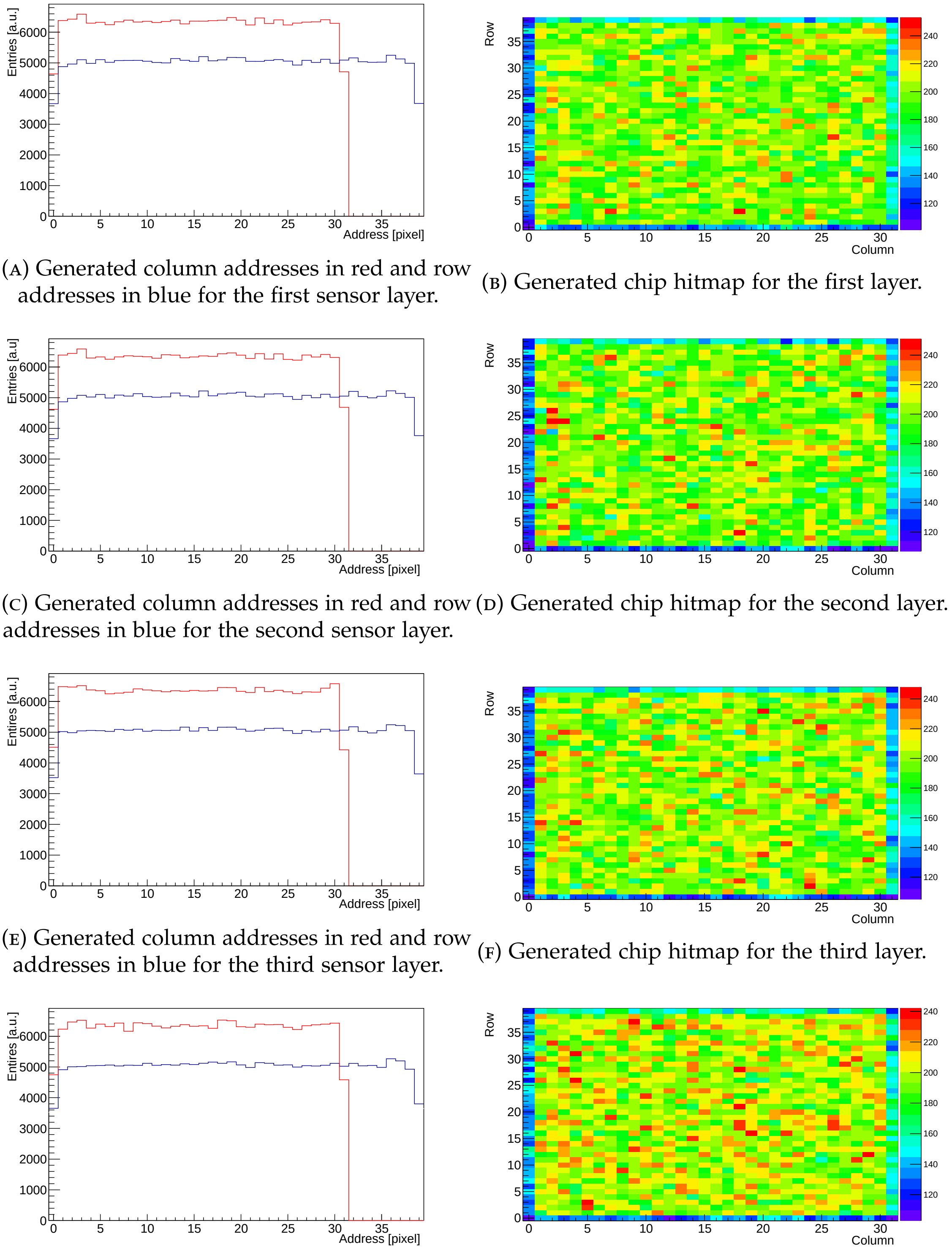

(A) Generated column addresses in red and row addresses in blue for the first sensor layer.

(B) Generated chip hitmap for the first layer.

(C) Generated column addresses in red and row addresses in blue for the second sensor layer.

(D) Generated chip hitmap for the second layer.

(E) Generated column addresses in red and row addresses in blue for the third sensor layer.

(F) Generated chip hitmap for the third layer.

(G) Generated column addresses in red and row addresses in blue for the fourth sensor layer.

(H) Generated chip hitmap for the fourth layer.

FIGURE 7.2: Validation of the event generation. The plots show the simulation results for a setup similar to the one at the DESY testbeam.

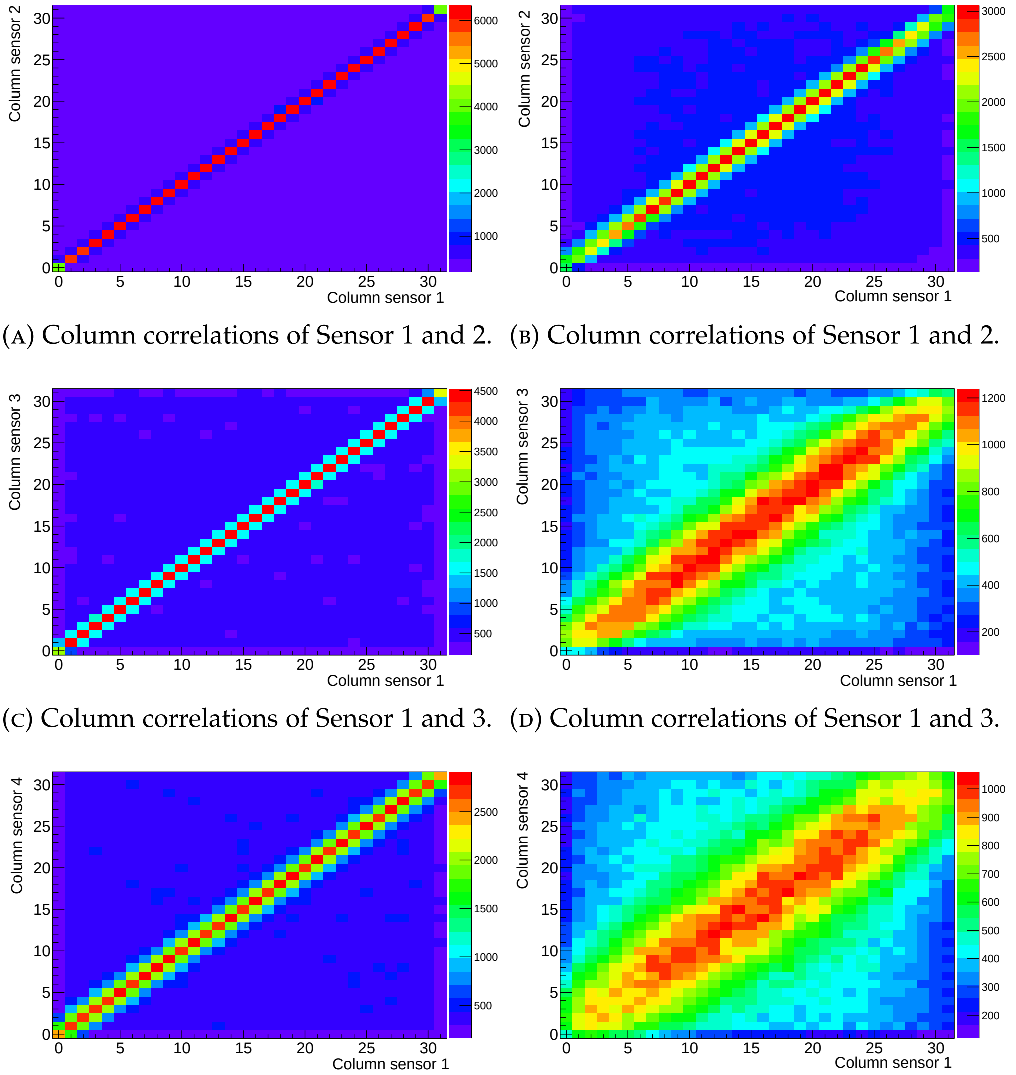

(A) Column correlations of Sensor 1 and 2. (B) Column correlations of Sensor 1 and 2.

(C) Column correlations of Sensor 1 and 3. (D) Column correlations of Sensor 1 and 3.

(E) Column correlations of Sensor 1 and 4. (F) Column correlations of Sensor 1 and 4.

FIGURE 7.3: Simulation results for the correlations between the column addresses of the sensors for different setups and particle energies, assuming two tracks per event and up to two background hits per layer: On the left side, the DESY testbeam (p=5 GeV electrons) is simulated and on the right side the PSI testbeam (p=250 MeV pions).

7.4 Validation of the Track Reconstruction

In the following, "simple tracking" denotes the algorithm ignoring multiple scattering and "tracking with correlations" the reconstruction including the uncertainties introduced by multiple scattering.

Before looking at the track reconstruction, the simple tracking itself has to be validated. From statistics it is known that the mean value of a $\mathcal{X}^2$ distribution should be equal to the number of degrees of freedom. For a straight track without any scattering, the mean value should therefore be 4 [42]. This can be tested by simply creating a sample of frames with random straight tracks with uniformly distributed slopes and propagating those tracks through all 4 layers, assuming no scattering and reconstruct the tracks. The resulting $\mathcal{X}^2$ distribution is shown in Figure 7.4.

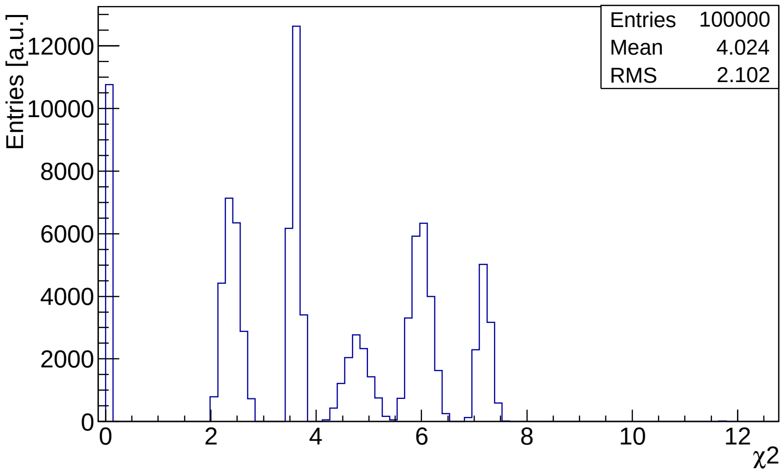

FIGURE 7.4: The $\mathcal{X}^2$ distribution for straight tracks without scattering.

The mean value of the distribution is 4, as expected. The shape is introduced by discretization effects, due to the pixel size: The reconstruction does not know about the real tracks and can only minimize the $\mathcal{X}^2$. In the case of a straight line, there is only a finite number of possible hit combinations resulting in a discrete distribution.
For Figure 7.4, the pixel size is set to the size of the MuPix 4 pixels. This leads to the peak at zero for tracks, where all pixels are in a perfect line. The spikes at 2, 3.5, 5, 6, 7.5 are from the other combinations. Smaller pixel sizes only increase the number of spikes but do not change the mean value.

The residuals of all planes have a mean value of zero and their distribution is symmetrical around zero. Due to the symmetrical plane setup it is expected, that the residuals of planes 1 and 4 and 2 and 3 are identical, which is also the case.

For the track fit using the generalized least squares method, it is not possible to simply fit tracks without scattering, due to the way it is working: Without scattering, the covariance matrix for the parameters will always be zero, which can not be inverted. Setting the scattering thickness of the layers to very tiny values, which are close to no scattering, leads to large inverted matrices. This leads to large $\mathcal{X}^2$ values and makes it impossible to analyze the method for tracks without scattering.

7.5 Comparison of the Track Reconstruction Methods

The reconstruction algorithms use the methods described in Chapter 4. Both algorithms are used to check for consistency of their results: The $\mathcal{X}^2$ distributions for a pure background sample, a pure data sample and a sample with two tracks and up to two background hits per layer are shown in Figure 7.5 for the two algorithms.

There are some slight differences in the distributions which can be explained by the differences between the two methods. The simple method has no estimation for the effect of scattering and its $\mathcal{X}^2$ definition, equation 4.5, is just the sum of the squared distances from the hits to the fitted track, weighted by the spatial resolution. There are also no correlations between different planes implemented. This leads to a change in the distribution, depending on the size of Θ_{MS}. More scattering leads to larger displacements and therefore a larger mean value for the $\mathcal{X}^2$ distribution.
The pure background samples look similar but also peak at different values. This is again explained by the working principle: The fit including scattering propagates the uncertainty due to scattering starting from a reference layer. Therefore, the contribution to the $\mathcal{X}^2$ becomes smaller with the number of planes and the distance between the hit plane and the reference plane. This leads to systematically smaller $\mathcal{X}^2$ values for random background combinations and scattered tracks compared to the simple tracking.
If one looks at the plots for two tracks and up to two background hits per layer, one can see, that the signal background separation is similar for both algorithms. The distribution has its minimum close to the end of the pure signal distribution, which is at different $\mathcal{X}^2$ values for the 2 methods. The large amount of hits in the region with $\mathcal{X}^2$ higher than 40 for the simple tracking and 20 for the tracking including correlations originates from background only. In the region below 20 (simple tracking) and 10 (tracking with correlations) almost all hits are signal hits.

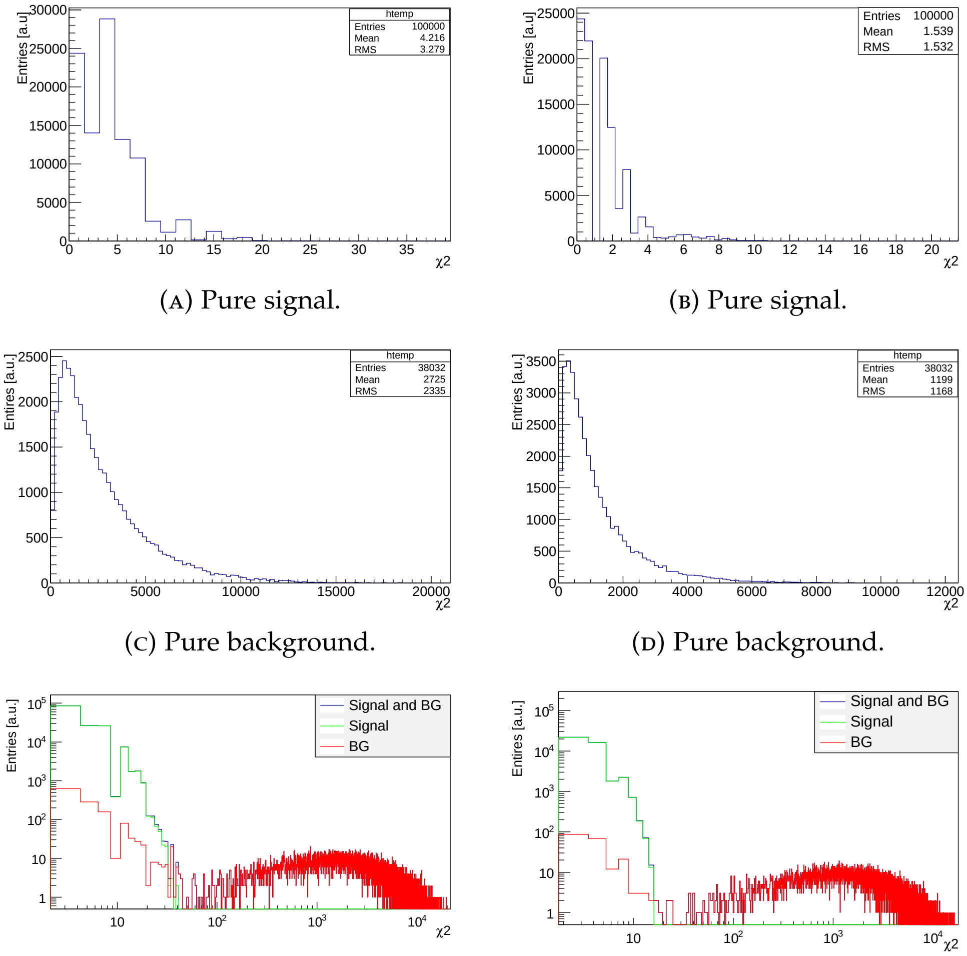

(A) Pure signal.

(B) Pure signal.

(C) Pure background.

(D) Pure background.

(E) 2 tracks and up to 2 background hits per layer.

(F) 2 tracks and up to 2 background hits per layer.

FIGURE 7.5: Overview over the $\mathcal{X}^2$ distributions from both reconstruction methods for DESY conditions. The left column shows the simple tracking and the right column the tracking including multiple scattering.

7.6 Reconstruction Efficiency and Background Rejection

To distinguish between background and signal events a $\mathcal{X}^2$ cut can be applied. The effects of this cut are explained in detail and compared for both techniques. To find a good trade-off between high track reconstruction efficiency and low background acceptance, both parameters are plotted as a function of the $\mathcal{X}^2$ for different scenarios. In Figure 7.6 the track reconstruction efficiency for the DESY and PSI conditions assuming two tracks per frame is shown.

For the DESY conditions, the performance of both techniques is comparable as the scattering is relatively low. Therefore the difference due to ignoring the scattering for the simple tracking is small. Under PSI conditions, this is different: The shape of the efficiency as function of $\mathcal{X}^2$ for the tracking with correlations is similar to the

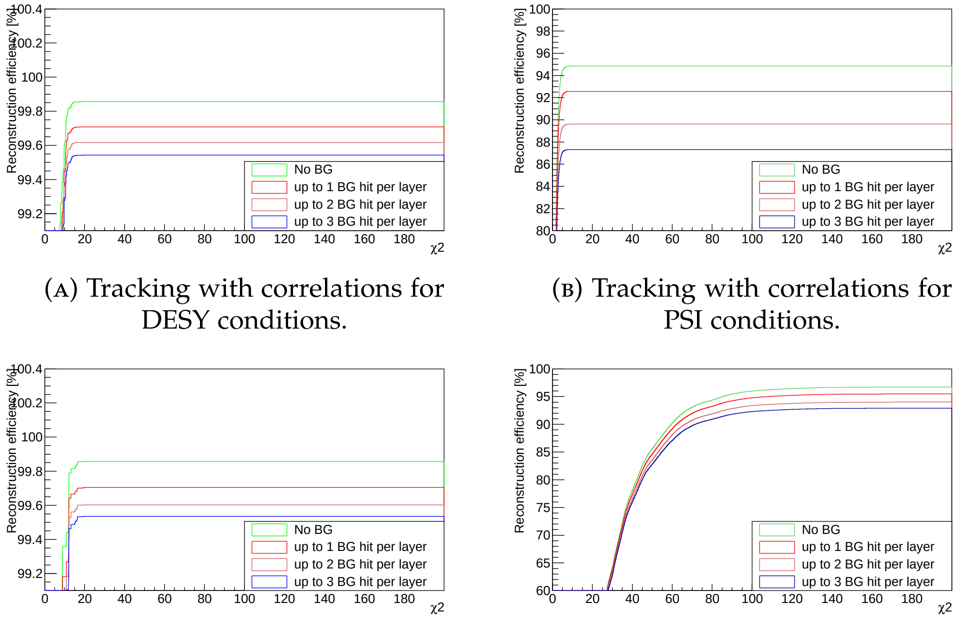

(A) Tracking with correlations for DESY conditions.

(B) Tracking with correlations for PSI conditions.

(C) Simple tracking for DESY conditions.

(D) Simple tracking for PSI conditions.

Figure 7.6: Reconstruction efficiency as function of $\mathcal{X}^2$ cut value for the two methods for different amount of background hits and for both DESY and PSI conditions, assuming two hits per frame: Top plots show the tracking with correlations and the bottom ones show the simple tracking.

DESY conditions, but their absolute efficiency is lower. This can be explained by the increased mean scattering, which leads to a higher probability of two tracks crossing each other and being misinterpreted as two different tracks. In addition a background hit at one of the planes can result in a better track candidate than the real track hit due to the scattering. In the simple tracking algorithm the reconstruction efficiency reaches a slightly higher absolute value of up to 96.5 % compared to the 94.8 % for the tracking with correlations. The shape of the efficiency curve changes strongly, which is also expected: Assuming a straight track, ignoring the scattering at the planes leads to larger residuals for more scattering and this leads per definition to a higher $\mathcal{X}^2$ value. Therefore the efficiency increases slower in $\mathcal{X}^2$ for larger mean scattering angles.
The absolute efficiency reaches never 100 % even for $\mathcal{X}^2$ going to infinity, if one has two or more tracks per frame. This is caused by the possibility of having two scattered tracks, which cross each other. This can result in lower $\mathcal{X}^2$ values another combination of the eight hits from the initial tracks.

The second relevant value to look at is the number of reconstructed fake tracks, either coming from pure background combinations or track hits combined with noise hit. In this case the normalization is not well defined. Therefore the background is normalized to the complete number of reconstructed tracks, because it gives a measure for the impurity of the track sample and the results are plotted in Figure 7.7. All plots show the same behavior: The more noise/background hits are created, the larger the probability to fit a fake track. For low $\mathcal{X}^2$ values, the background is coming from reconstructed tracks, consisting of a mixture of real track hits and noise hits, while the high $\mathcal{X}^2$ values are coming from pure background distributions.

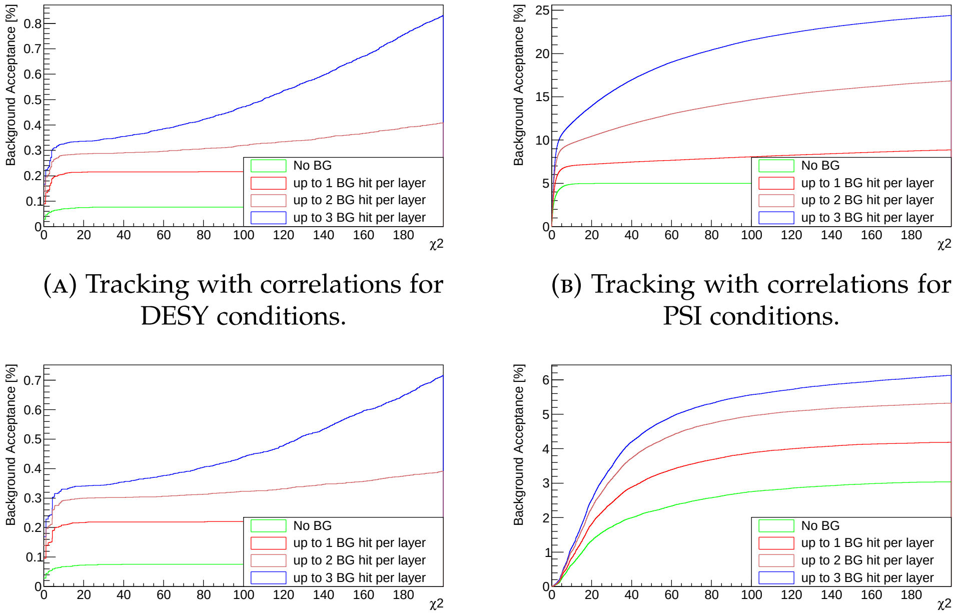

(A) Tracking with correlations for DESY conditions.

(B) Tracking with correlations for PSI conditions.

(C) Simple tracking for DESY conditions.

(D) Simple tracking for PSI conditions.

FIGURE 7.7: Background accaptance as function of the $\mathcal{X}^2$ cutvaue for different numbers of background hits and tracks per frame assuming the DESY and PSI conditions.

For the DESY conditions, the difference for both techniques is again very small and the overall background acceptance stays below 1 % which is a very low background acceptance. In contrast, for PSI conditions, the background acceptance for the simple tracking increases to over 6 % for the analyzed range, which can be explained: Fake tracks can be created either by pure background hits, combinations of background and track hits or wrongly assigned track hits. The probability to create these fake tracks increases with increasing scattering. The tracking with correlations shows a much faster rising background acceptance as function of the $\mathcal{X}^2$ cut. This has to be put into perspective of the faster rising signal efficiency curve, already saturated at around 20 compared to the simple tracking, which saturates around 100.

Figure 7.6 also shows, that the absolute reconstruction efficiency of the simple tracking algorithm is higher than the one for the tracking with correlations while the background acceptance for the simple tracking is smaller compared to the other method (see Figure 7.7).

Optimal $\mathcal{X}^2$ Values

The optimal $\mathcal{X}^2$ strongly depends on the settings. In the case of the DESY conditions, a cut value of 15 makes sense for the tracking with correlations, because the signal reconstruction efficiency is saturated and the background acceptance is below 1% for single track frames and 2% for two track frames.
For the simple track fitting, the best value is 40 for the DESY conditions, resulting in comparable signal efficiency and background acceptance.

For the PSI setup, the ideal cut value for tracking with correlations can be determined with the same arguments: The background acceptance for $\mathcal{X}^2$ smaller than 15 is again acceptable small and stays below 15 % and the efficiency is again saturated at up to 95 %. For the simple tracking, the cut value should be set around 100, leading to a high efficiency of up to 95 % and an acceptably background acceptance of below 6 %.

Those results depend on the amount of scattering and the geometrical properties of the setup and therefore have to be reevaluated for every setup. The tracking with correlations is stable under changes of scattering in terms of reconstruction efficiency, while the simple tracking method varies strongly with the scattering and geometry. The background acceptance is slightly lower for the simple tracking, which can be explained by the way the tracks are selected: The simple tracking minimizes the squared distances while the tracking with correlations starts at a reference plane and accepts hits with larger distances at higher plane numbers. So in the latter case it becomes more likely to pick up a noise hit on one of the last planes, which fits better than the hit corresponding to the track.

Chapter 8

DESY T22 Testbeam

From 02.02 - 09.02.2014 a testbeam at DESY was performed and the HV -MAPS telescope was tested for the first time uisng the MuPix 4 prototype.
DESY II is used as a pre-accelerator for the PETRA III ring and contains electrons with up to 7 GeV [55]. A carbon fiber (see Figure 8.1) in the beam is used to create hard Bremsstrahlung. The photons hit a converter target where electrons and positrons are created. A magnet, placed behind the converter, spreads the beam and a lead collimator selects the requested energy range.
Four Bremstrahlung beamlines are available for testbeams in the DESY testbeam hall shown in Figure 8.2: T21, T22, T24, T24/1. The Mu3e testbeam was performed in area T22, equipped with the EUDET telescope *Aconite* [57, 58, 59] to characterize the MuPix sensors. The MuPix telescope setup was placed on an xy table behind the EUDET telescope, roughly 7 meters away from the collimator. A GBit Ethernet connection between the hut and the area itself was used to remotely control the readout computer and the low voltage supply in the area during the measurement time. The high voltage supply could not be controlled remotely and was therefore fixed while the beam was on.

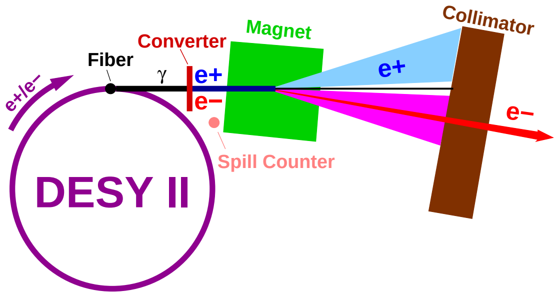

FIGURE 8.1: Schematic of the DESY testbeam system [56].

The MuPix 4 characterization and resolution measurements had the highest priority and the beam energy was therefore fixed to 5 GeV resulting in low multiple scattering

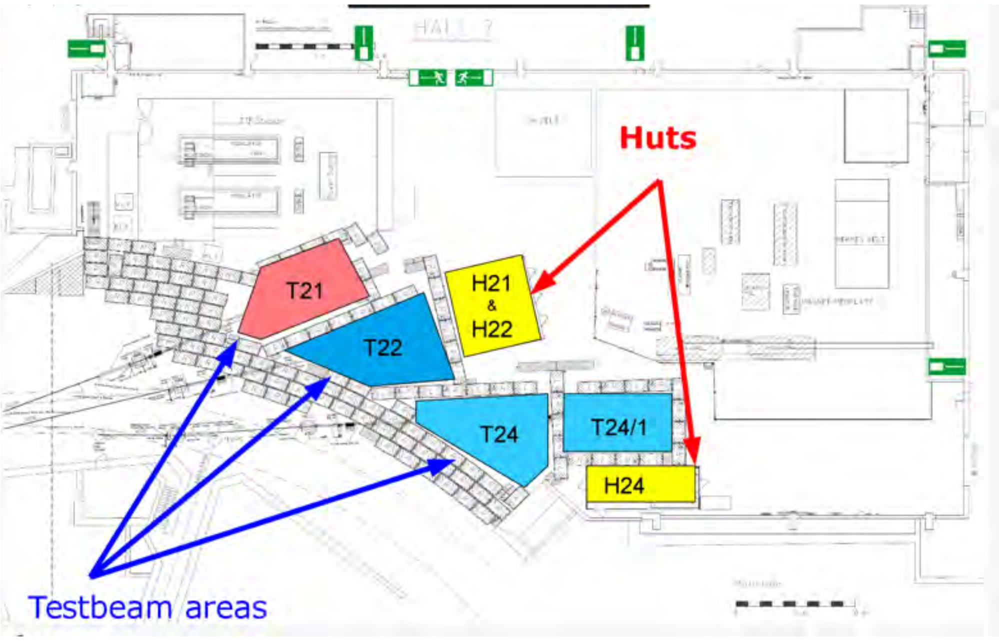

FIGURE 8.2: Overview over the DESY II testbeam hall: The four testbeam areas are colored in blue and red, while the control huts are marked in yellow.[60]

but a relatively low particle rate. However, the main goal concerning the telescope was to test the telescope under real testbeam conditions and to measure hit correlations between different planes. This was the very first test and it was not expected to have a completely working setup.

8.1 Setup

In Figure 8.3, a picture of the setup is shown. The MuPix telescope was mounted on one of the available xy-tables. The connection to the PC was done via 8 flat ribbon cables surrounded by aluminum to shield them against external electronic fields and a plastic foil to protect the cables. In addition, all PCBs were connected to a separate LV power supply, while the HV was connected to a shared HV supply and set to 60 V for all measurements.

As sensors, the sensors from the single MuPix 4 setups [22, 23] are re-used. The first three PCBs are thinned down to 100 µm to reduce the influence of multiple scattering. The last layer consisted of a chip on carrier mounted on a normal PCB. The chip was placed at the collimator side and detected the particles before they passed the PCB and carrier. Only one sensor was glued directly on the PCB, while the remaining two sensors were glued on a carrier, mounted on a thinned board and added a large amount of material in the beam. This introduced additional scattering and reduced the resolution.

Foam blocks in front of the readout computer were used as a support structure to carry the weight of the cables and connectors and to protect the FPGA boards and PCIe slots.

An aluminum structure behind the telescope was also used as a stress relief for the cables.

The chosen coordinate system is a right handed Cartesian coordinate system with the positive z-direction going along the beam particle flight direction. The positive x-direction is parallel to the columns, pointing towards higher columns, while the y-direction corresponds to the rows. The alignment of the setup was done by eye with the help of a cross laser available at the testbeam area, which was mounted directly on the collimator and pointed along the beam direction. With this alignment method it was only possible to align the complete telescope parallel to the beam. There was

Layer	Z-Position	Sensor number	PCB number	Mounting	x/X_0
1	0 mm	# 41	# 41	on thin PCB	2.9 ‰
2	75.5 mm	# 15	# 31	Carrier on thin PCB	33.9 ‰
3	150.5 mm	# 13	# 30	Carrier on thin PCB	33.9 ‰
4	226 mm	# 12	# 20	Carrier on PCB	33.4 ‰

Table 8.1: Overview over the used sensors for the DESY testbeam. Sensor 1 is the closest to the beam window, while layer 4 is the last one. During the testbeam, sensor 1 and 2 were swapped.

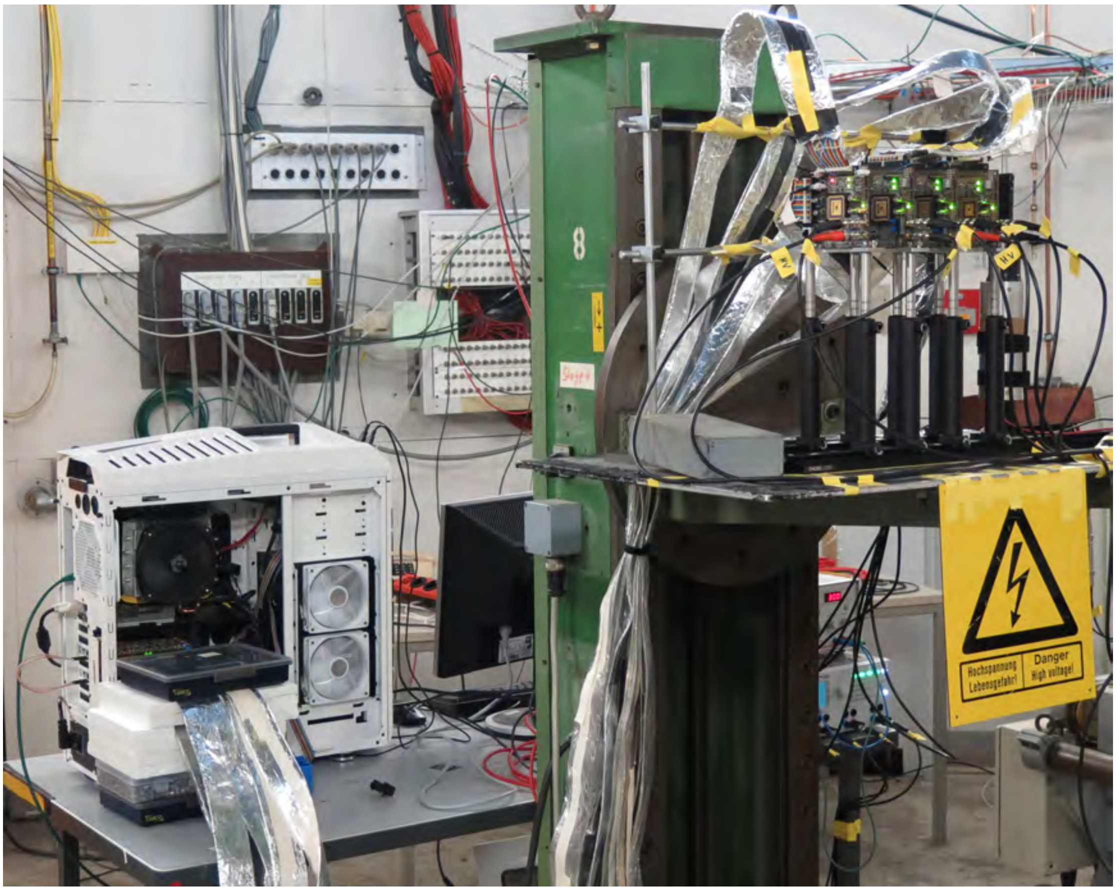

Figure 8.3: The DESY testbeam setup: On the top right, the telescope, mounted on a movable stage, provided by the DESY testbeam group. The telescope is connected to the RO computer via 4 m long shielded ribbon cables.

no possibility to move the layers relative to each other in horizontal direction, so the x alignment limit in this context was the precision in gluing the sensor on the PCB, which turned out to be relatively precise. The vertical alignment was done with a water level, which lead to a precision on the level of 100 µm over the full telescope length.

8.2 Data Taking & Performance

After a smooth setup assembly, quite some time was spent in order to find the beam position. A scintillator in front of the telescope was added as a local beam monitor. Subsequently, roughly 60 hours of data were taken without any trouble with the DAQ system. No crash or memory leak occurred.
In total 2800 runs were recorded, each representing 30 seconds of data taking. The short runs were necessary due to a software issue at the time of the testbeam; the monitoring was not implemented in the software and a second program running in parallel to the readout program plotted the monitoring graphs described in Chapter 5. The raw data was written unsorted online to a binary file on a hard disk. Each data block contains a header of four 32 bit words containing the meta information: The first is a FPGA label used to distinguish between hits from the different FPGAs offline. The second word is a beginning of block marker. The third word counts the number of events and the fourth counts the number of triggers in order to check the file consistency, while the fifth word gives the number of hits in this block. At the end of each block a trailer with the coarse counter giving the time information and end of block marker is written. This results in a header plus trailer of seven words per block. The amount of hits per block is less than 3. Therefore a lot of overhead is created and large files.

Data Runs

In order to understand and analyze the influence of different thresholds and to calculate the efficiency of different layers, data samples with different settings were recorded. Two threshold scans were performed for sensors number 15 and 41. After the first scan, the sensors with number 15 and 41, corresponding to the layers 1 and 2, were swapped. This was done to have the possibility of using the sensor at layer 2 as a DUT for the offline analysis. Matching reconstructed tracks from layer 1, 3 and 4 with a time coincident hit in layer 2 can be used to determine the efficiency of the sensor at layer 2. Due to the swapping of the sensors the geometrical properties changed: Therefore the Geo ID 001 describes the initial geometrical properties and Geo ID 002 the settings after interchanging the sensors. Finally three long runs with high statistics were taken. A summary of the different data samples taken at DESY is shown in Table 8.2.

ID	Geo	Number	Sensor # 41	Sensor # 15	Sensor # 13	Sensor # 12
	ID	of Runs	Threshold [V]	Threshold [V]	Threshold [V]	Threshold [V]
01	001	660	0.840	0.850	0.850	0.840
02	001	1304	0.850	0.860	0.860	0.850
03	001	005	0.820	0.825	0.825	0.825
04	001	113	0.840	0.855	0.855	0.840
05	001	125	0.840	0.850	0.855	0.840
06	001	546	0.840	0.845	0.855	0.840
07	001	151	0.840	0.840	0.855	0.840
08	001	144	0.840	0.835	0.855	0.840
09	001	123	0.840	0.830	0.855	0.840
10	001	132	0.840	0.825	0.855	0.840
11	001	126	0.840	0.820	0.855	0.840
12	001	123	0.840	0.820	0.855	0.840
13	001	118	0.840	0.865	0.855	0.840
				sensors swapped		
14	002	314	0.840	0.855	0.855	0.840
15	002	123	0.840	0.850	0.855	0.840
16	002	140	0.840	0.845	0.855	0.840
17	002	132	0.840	0.840	0.855	0.840
18	002	600	0.840	0.835	0.855	0.840
19	002	128	0.840	0.830	0.855	0.840
20	002	043	0.840	0.825	0.855	0.840
21	002	868	0.850	0.840	0.850	0.840

Table 8.2: Overview over the runs taken at DESY. The Geo ID describes the mechanical setup and alignment. During the two threshold scans, the system was not touched. Swapping sensor # 41 and # 15 changed the orientation slightly. The ID is used to label results from this testbeam.

DESY Data Structure

At DESY, the timestamps of the sensors were switched off. Therefore the only time information available is the coarse counter of the FPGA. This counter counts up one every 5.12 µs and is stored in the meta information of each hit block created by the FPGA. The data stream in the final file is not sorted.

DAQ Performance

The DAQ was running stably under normal DESY beam conditions. For a stress test to prove the stability of the DAQ the thresholds of all four sensors were reduced down to 0.8 V, which is essentially the baseline voltage. The so created noise hits were read out and stored. The highest achieved data rate is 610 MByte/run, which corresponds to 20.3 MByte/s. Each FPGA produced 10.15 MByte/s = 81.2 MBit/s, with multiple hits per event. For example one hit block with 100 hits, 50 per sensor, consists of 107 words à 32 bit. This would correspond to a track rate of

$$F_{\text{Track}} = \frac{81.2 \cdot 10^6}{2 \cdot 107 \cdot 32\,\text{s}} = 5.93 \cdot 10^5\ \text{Hz} = 593\ \text{kHz}. \tag{8.1}$$

With a more efficient file structure, this rate can be even increased, but the bottleneck at this testbeam was neither the software nor the sensor itself. The long ribbon cables and the conservative wait times between readout signals from the FPGA limited the readout speed. Another possible limit, which was not reached at this testbeam, is the data logging speed on a HDD, which is in the order of 50 MByte/s.

MuPix 4 Performance

The hitmaps of the sensors in the HV-MAPS telescope as function of the row and column address are shown in Figure 8.4. All sensors have the known feature of non-readout row addresses (compare Chapter 5.4). This leads to more hits in the first two rows. All sensors are also slightly noisier on the right side. MuPix # 12 and # 41 have both one hot pixel. The two pixels contain more than 99 % of all hits. Due to digital cross talk on the ribbon cables, some hits are read out with the wrongly address. These wrong assigned hits can bee seen in the non working rows.
In this test setup, the time stamps were deactivated in order to reduce the digital cross talk. Because of the cross talk it was not possible to read out the MuPix 4 sensor with the time stamps switched on with the 4 m long non single lane shielded ribbon cables. This behavior is analyzed in detail in [23] and [22].

Online Monitoring

The written data files were processed by the monitoring and monitoring plots were created and updated. The online monitoring was also running stably and could process a single run of 30 seconds in roughly 3 seconds. The monitoring output, shown in Figure 8.5, contains all relevant information for the DESY testbeam. This includes the column correlations of all layers, the sensor hitmaps and some cross relations between columns and rows. All two dimensional histograms are plotted as scatter plots, because the correlations between layers are better visible as scatter plots, if hot pixels are present.
Online, the correlations between the first two and the last two sensors are more clearly visible than the ones from separate FPGAs. This is due to the unsorted data structure - the two FPGAs were running at the same clock speed and were synchronized. However, they were not necessarily in the same readout state nor did they read out the same number of frames. The data were stored as fast as possible and no event sorting was performed. This lead to a non-continuous data stream and the monitoring macro was not able to recognize the hit correlations between the FPGAs.

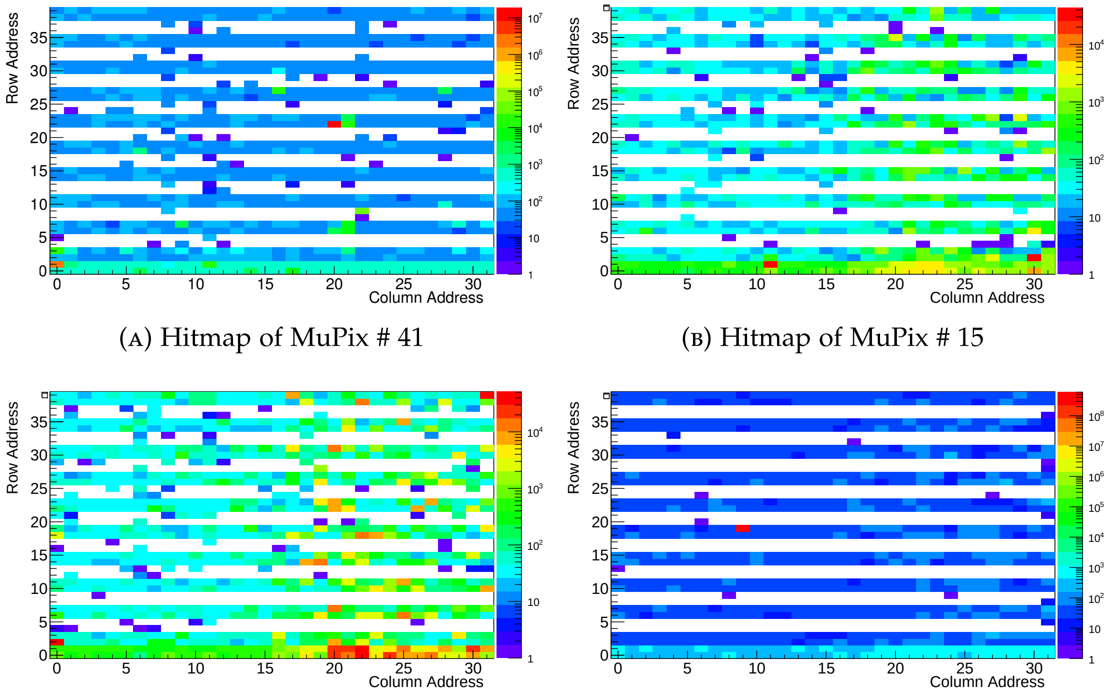

(A) Hitmap of MuPix # 41

(B) Hitmap of MuPix # 15

(C) Hitmap of MuPix # 13

(D) Hitmap of MuPix # 12

Figure 8.4: Exemplary overview over the Hitmaps of the prototypes from run ID 01.

The vertical and horizontal lines in the correlation plots of Figure 8.5 are the result of the hot pixels, which are present in every readout cycle and therefore introduce a large amount of correlated hits with other background or between noise hits and the tracks.

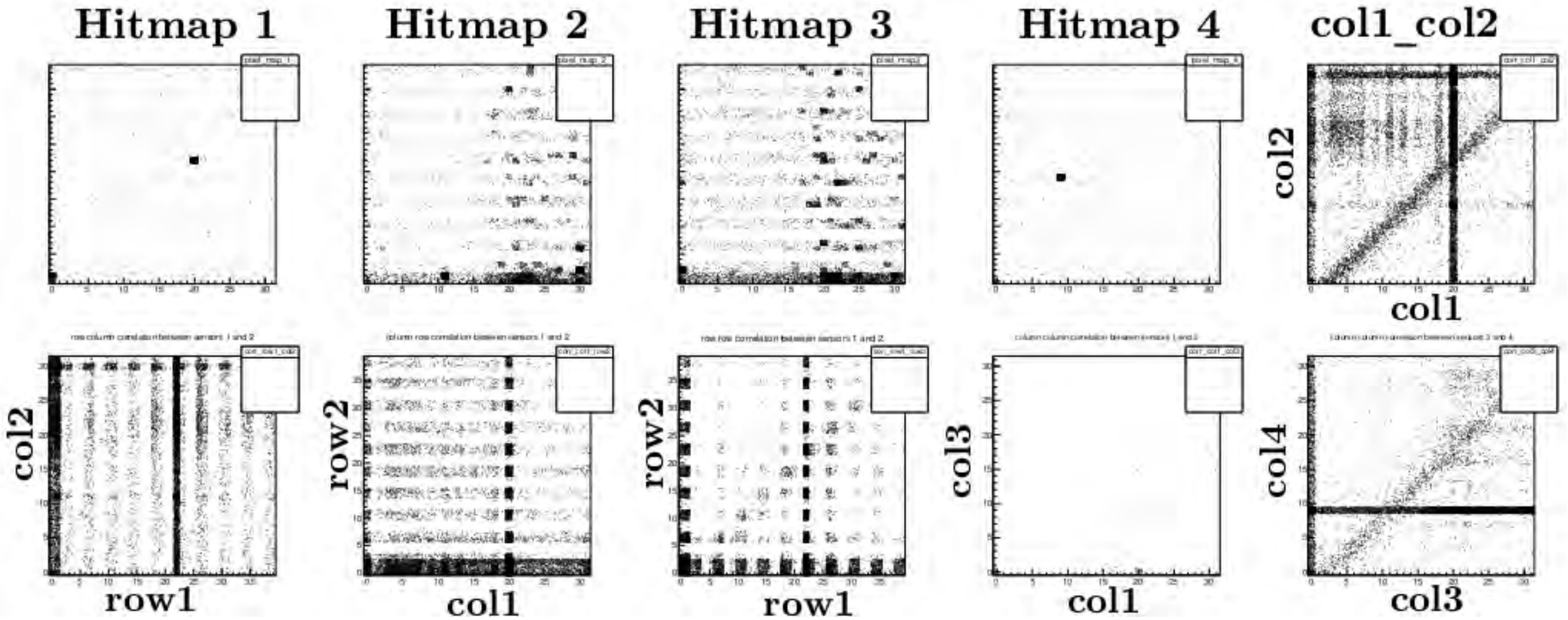

Figure 8.5: Detail of the online monitoring macro output. The four left plots in the upper row show the hitmaps and the upper right plot shows the column correlations between the first two sensors. The three left plots in the lower row are the remaining correlations of the first two sensors. The fourth plot shows the column correlations of sensors 1 and 3 and the last plot the correllations of layer 3 and 4. The larger labels were added later for better readability.

8.3 Analysis

The analysis of the DESY data was done offline in multiple steps as described below. The first step was to reproduce the results of the online monitoring. At this point, two issues were realized. In the data files events without any hits existed, even if the block header indicated hits. At the corresponding position, entries from the header were written. This is most likely the result of a bug in the code and can not be fixed offline. The second feature was, that hits with only one hit per frame never occurred. This was most likely caused by another software issue, which was corrected after the testbeam. These problems reduced the amount of useful data for offline analysis.

Frame Creation from raw Data Files

The data files are not time sorted. Therefore a complete run file is read and the contained hit blocks are sorted by their coarse counters. From this sorted list, the frames for the analysis are created by merging all hit block with the same coarse counter into one frame. These frames are used to search for tracks and to align the telescope.

In the second step the hot pixels were removed, as described below. In the third step, a rough alignment was done and finally the tracks were reconstructed as described in Section 7.2.

8.4 Hot Pixel Removal

The used MuPix 4 prototypes all have issues with hot pixels, which were firing in many readout frames, without seeing real particles. They had to be removed, since they can introduce fake tracks. This was done by looping over all frames and counting the hits per pixel.

The hot pixel removal was performed in two steps: The first step was to remove the hot pixels by marking all pixels which have more than 5 % of the hits (pixel firing essentially in each readout). This is required to perform the second step, calculating the mean of all remaining pixels and all pixels with

$$\#Hits > \#\overline{hits} + n \cdot \sigma_{\overline{hits}} \tag{8.2}$$

were removed. n can be changed depending on the required noise suppression. $\sigma_{\overline{hits}}$ is the RMS of the mean hit number. This scheme is working very nicely for a tuned pixel, with constant baselines on all sensors, which would correspond to homogeneous

hitmap for the sensors in Figure 8.4. This is not the case for the MuPix 4, where the right side of the sensors turned out to be noisier than the left side. This results in a removal of many pixels on the right side (compare PSI analysis in Chapter 9). This behavior comes from the fact, that an in-proper DAC-tuning procedure was used, which was originally not developed for the MuPix 4 chip. For the MuPix 6 prototype a customized tuning is under development at the moment [24].
The second reason for removing only the hot pixels is that the non-working row addresses introduced more hits in the two lowest columns compared to the remaining chip. This has the same effect as the not optimal DAC settings.

8.5 Telescope Alignment

The third step was to align the telescope: The difference of the column position of hits from the same frame between the different sensor layers can be plotted to study the shift of the sensors. Fitting a Gaussian to these position difference plots leads to a first estimate on the misalignment of the telescope. Figure 8.6 shows exemplary alignment results for run ID 21, which was a run with comparable conservative threshold settings and high statistics.

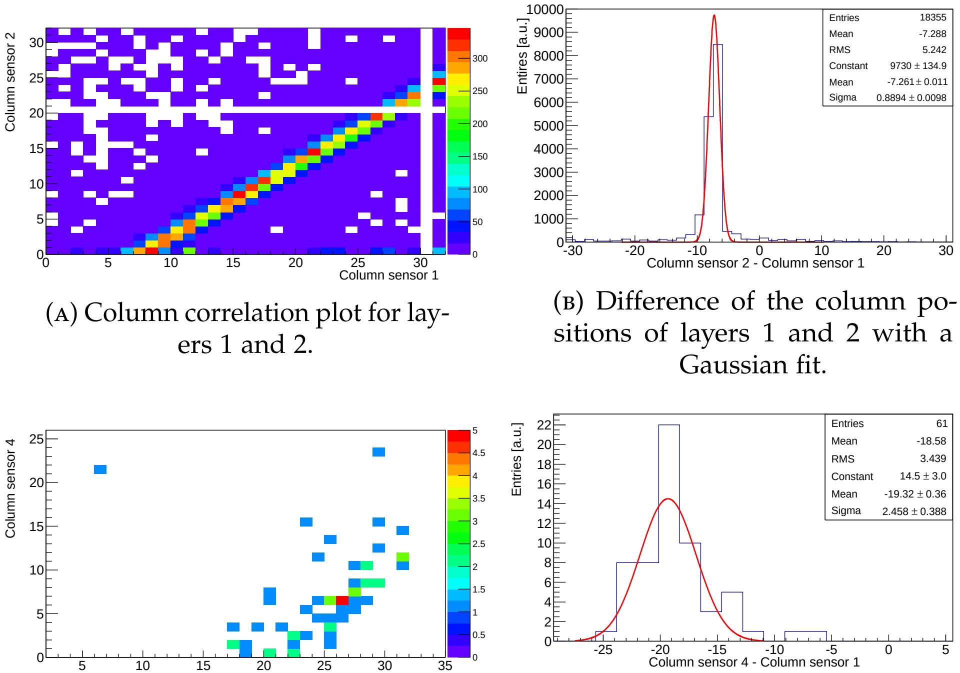

(a) Column correlation plot for layers 1 and 2.

(b) Difference of the column positions of layers 1 and 2 with a Gaussian fit.

(c) Column correlation plot for layers 1 and 4.

(d) Difference of the column positions of layers 1 and 4 with a Gaussian fit.

Figure 8.6: Plots used for the alignment of the MuPix telescope for run ID 21 after removal of hot pixels.

The misalignment of the telescope was −7.26 ± 0.01 pixel in the case for the first and second layer. This small uncertainty suggests, that the alignment between two planes can be done with a high precision below the pixel size, before tracks are reconstructed. The width of the distribution gives an upper limit on the resolution of the telescope and is 0.89 pixel. This is already larger than the intrinsic pixel resolution of

$$\sigma_{\text{Pixel}} = \frac{size_{\text{Pixel}}}{\sqrt{12}} \approx 0.29 \cdot size_{\text{Pixel}}.$$

This means that multiple scattering is the dominating effect for this setup even for 5 GeV electrons. The lower two plots in Figure 8.6 show the scattering effect and the misalignment between the first and fourth layer. This distribution shows larger smearing and a large offset, which is expected, because the misalignment of the planes becomes larger with higher distances between the layers. This was already visible in the online monitoring, but could not be corrected due to the missing possibility of moving the chips in x direction. This was improved in future setups using the PCB holder version 3.

8.5.1 Timing and Synchronization

The larger number of correlated hits between planes 1 and 2 (3 and 4) and the small number of correlated hits between planes 1 and 4 suggests a crosscheck whether the FPGAs were running synchronously. Both FPGAs were running with a 50 MHz clock and the coarse counter was counting up every 5.12 µs, which corresponds to the overflow frequency of a 8 bit counter at 20 MHz. Because of the switched off sensor time stamps this is the only available time information. Therefore the hits corresponding to a track should be in the same coarse counter frame. If the two FPGAs were running asynchronously, there would be an offset between events with 2 hits in both FPGAs. The probability to have random coincidences between two tracks in this case is very low due to the low particle rate $\mathcal{O}$(1 Hz).

To test if both FPGAs were synchronized a scan over the run ID 21 was performed. a search for events with hits in all for layers within 1000 frames before and after each frame was done. The difference in the coarse counter for the events with hits in layers is filled in a histogram. This leads to the result, that the combined events with hits in 4 layers are suppressed by an order of magnitude for one coarse counter of. A zoom into this histogram is shown in Figure 8.7. Most events with hits in all layers are coincident. The small number of events, which are not coincident can be explained with the low particle rate $\mathcal{O}$(1 Hz) and by the time resolution of the sensor in combination with the coarse counter frequency. Figure 8.7 shows that there was neither a constant offset between the two FPGAs nor were they running at different frequencies. Therefore, the low amount of coincident hits between the two FPGAs cannot be explained with an

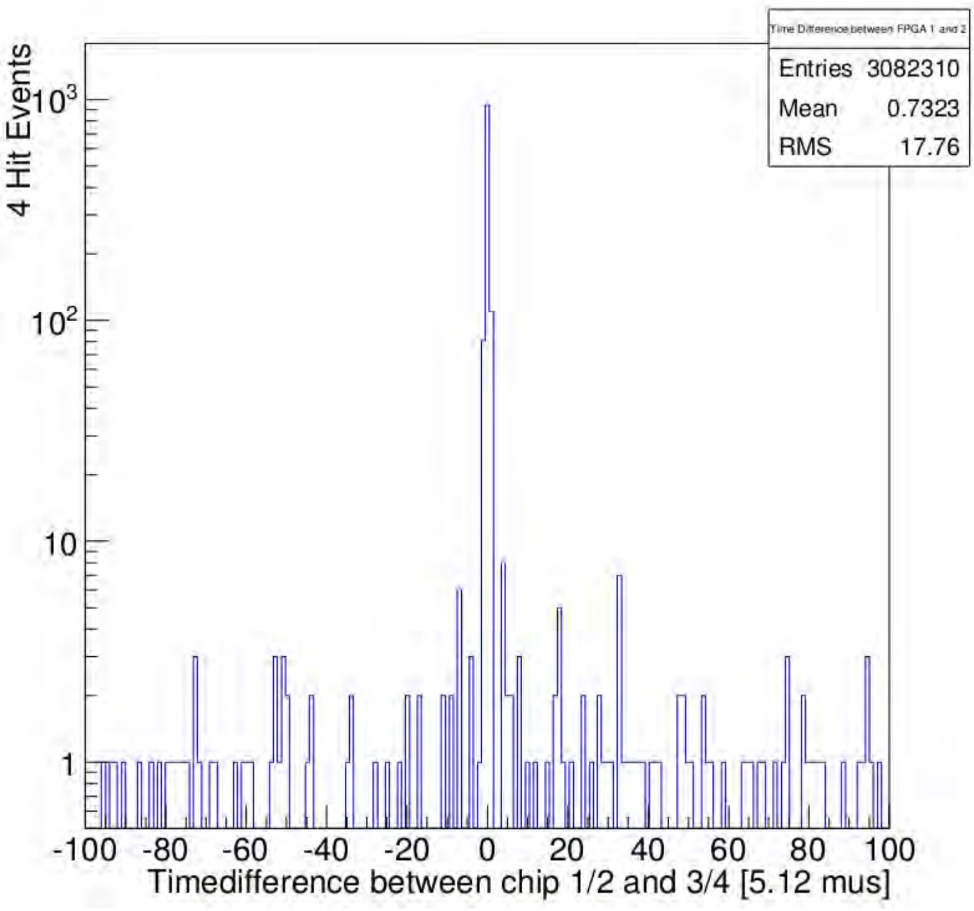

FIGURE 8.7: Events with hits in all four layers plotted against the coarse counter difference of the two FPGAs.

offset. It is most likely caused by the data file storage issues explained at the beginning of this chapter.

8.5.2 Track Reconstruction

The MuPix 4 address problem makes it impossible to use the two tracking methods described in Chapter 4. The number of events fulfilling the requirement of 4 hits is already very small. Taking also the row address into account will reduce the number of tracks that can be reconstructed dramatically due to the large probability of hits in working and non working rows in different layers - Therefore, it is useful to analyze the data looking only at the x position and perform the fit in one dimension. This has two effects: First the $\mathcal{X}^2$ for real tracks will be smaller due to the not used y position. Second the probability to get fake tracks due to noise hits is strongly increased because the effective number of "pixels" is reduced from 1280 to 32, if the rows are ignored.

However the structure of the track reconstruction algorithm is the same as in the simulation (see Section 7.2): The hot pixels are already removed and the hit-track linking and track selection is done in exactly the same way. The main difference is the fit routine itself. The simple tracking methods, converted to the one dimensional track model is used. Therefore the $\mathcal{X}^2$ is now defined as

$$\mathcal{X}^2 = \sum_{i=1}^{4} \frac{(x_i - (x_0 + a_x z_i))^2}{\sigma^2_{x_{mi}}}. \tag{8.3}$$

Using the pre-aligned data one can perform the track fit minimizing the equation 8.3, like for the simple tracking. The $\mathcal{X}^2$ distribution for the fitted tracks from ID 21 is shown in Figure 8.8.

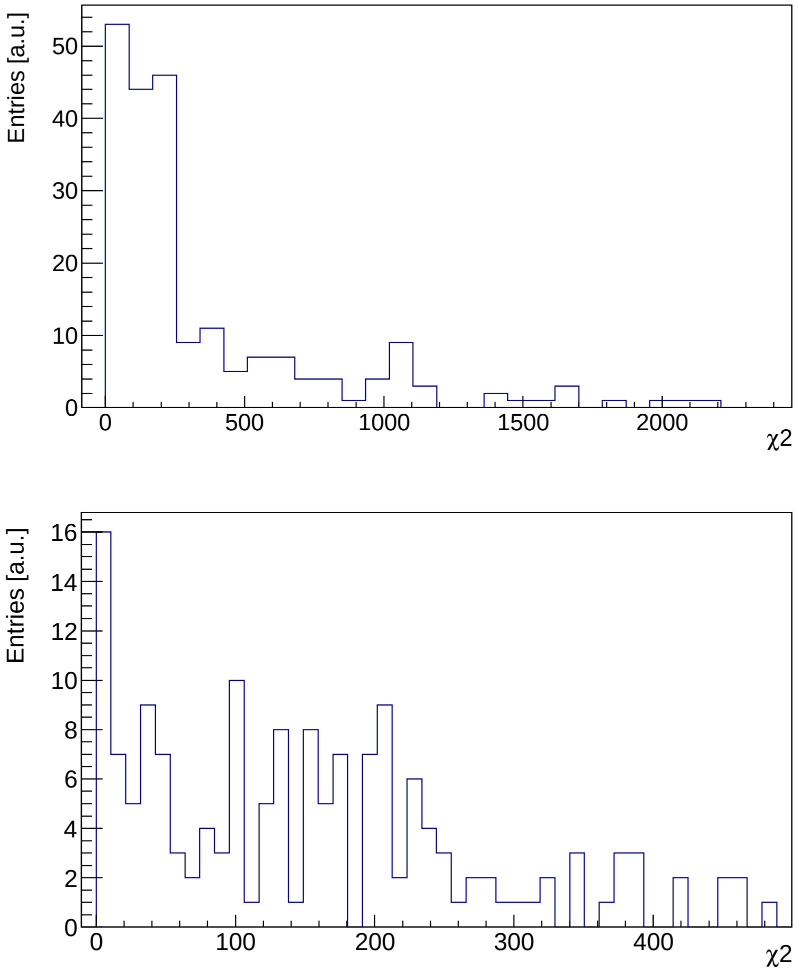

Figure 8.8: $\mathcal{X}^2$ distribution for run ID 21 after applying the hot pixel removal and the mechanical alignment corrections.

The zoom into the $\mathcal{X}^2$ distribution, shown in the bottom plot in Figure 8.8, shows, that track with $\mathcal{X}^2 < 40$ are existing. This shows that the reconstruction is working, even for thick and not tuned sensors. In the simulations it was shown, that there is a minimum in the $\mathcal{X}^2$ distribution (compare the two bottom plots in Figure 7.5). This minimum is not clearly visible in Figure 8.8. A trend towards a minimum around 70 could be seen, but there is not enough statistics to call this a significant minimum. Higher statistics would be required to show the significance. The position could be explained by an underestimation of the radiation length for the layers in the simulation, due the maybe underestimated scattering thickness of the carrier because of its unknown exact composition. For stronger scattering the $\mathcal{X}^2$ distribution changes and the minimum will move to higher values and become less significant, because the shape of the random combinations background will not change.

Another reason for the high $\mathcal{X}^2$ values could be a misalignment of the planes. A misalignment would result in residuals of the tracks not being distributed around zero. Therefore the track residuals are plotted in Figure 8.9.

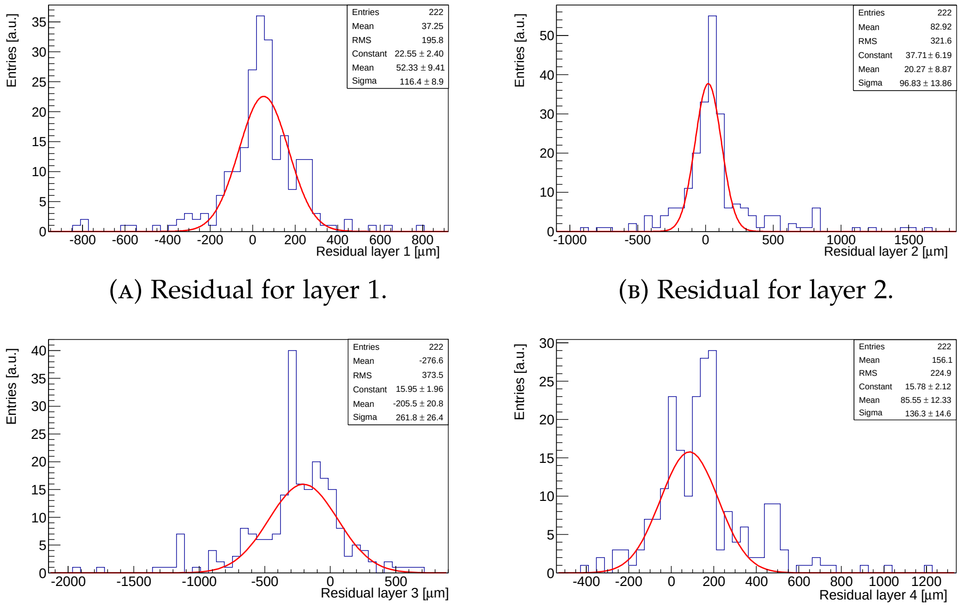

(A) Residual for layer 1.

(B) Residual for layer 2.

(C) Residual for layer 3.

(D) Residual for layer 4.

FIGURE 8.9: Track residuals for the DESY run ID 21.

The residuals for layers 1 and 2 peak around zero with a mean value smaller than the pixel size, while the residuals for layers 3 and 4 are off by more than a pixel. The shape of layer 3 is asymmetric and has one sharp spike on the distribution. This might be due to a misalignment, which is not visible in the correlation plots. Another reason could be the digital cross talk on the readout cables, which leads to wrongly assigned hits. A systematic bias in the track reconstruction algorithm can be excluded, because there is no offset visible in the simulations.

8.6 Summary

The results from the DESY testbeam in February 2014 show that the MuPix telescope concept is sustainable. It turns out, that the mechanical alignment can be done with a high precision in y $\mathcal{O}$(100 μm) and z $\mathcal{O}$(1 mm). The position in x is not variable, which reduces the total overlapping area to roughly 25 % of the chip size. This is improved with the latest PCB holder prototype version 3.

The DAQ system is stable, even though some bugs in the data storage reduced the amount of useful data. All DAQ problems found during this testbeam have been fixed in the meantime.

The hot pixel remover is working, which is clearly visible in the correlation and projection plots in Figure 8.6. It is also visible there, that the shifts of the system in x direction can be determined with high precision in the order of less than one pixel.

Finally the track reconstruction algorithm is working. It was possible to reconstruct tracks even with the MuPix 4 sensor and its features and the non optimal DAQ settings.

Chapter 9

PSI πM1 Testbeam

The PSI testbeam from 01.06 - 08.06.2014 was scheduled to test the new MuPix 6 prototype and the new features developed since the DESY testbeam. This included the new readout software, the improved mechanics, especially the newly developed PCB holder, the MuPix 6 prototype implementation, the inclusion of the scintillating tiles as timing reference, the time stamps and the new LVDS data links. The last and, besides the test of the MuPix time resolution, the most important goal was to take high statistic data runs to test the developed track reconstruction methods at lower energies with a completely working chip. PSI offers a secondary beam, created at the primary target M (see Figure 2.8) of a mixture of pions, muons and electrons with a selectable momentum between 100 MeV/c and 500 MeV/c [61]. While the relatively low particle momenta lead to pronounced multiple scattering the particle rate at πM1 reaches up to 1 GHz.

The PSI accelerator team performed a scheduled accelerator maintenance during the first two test beam days, where a water leak in one of the accelerator magnets was found. This was only fixable after removing one of the cavities. Unfortunately, this resulted in a testbeam without beam.

While waiting for beam, the telescope was assembled and tested using an active source.

9.1 Setup

The setup looked similar to the DESY testbeam setup. The main changes were the additional scintillating tiles, the new PCB holders and the SCSI III readout cables. A picture of the PSI setup is shown in Figure 9.1.

The four sensors aligned parallel to the beam were mounted on the telescope mechanics. The power was supplied via BNC cables. The slow control was done with the ribbon

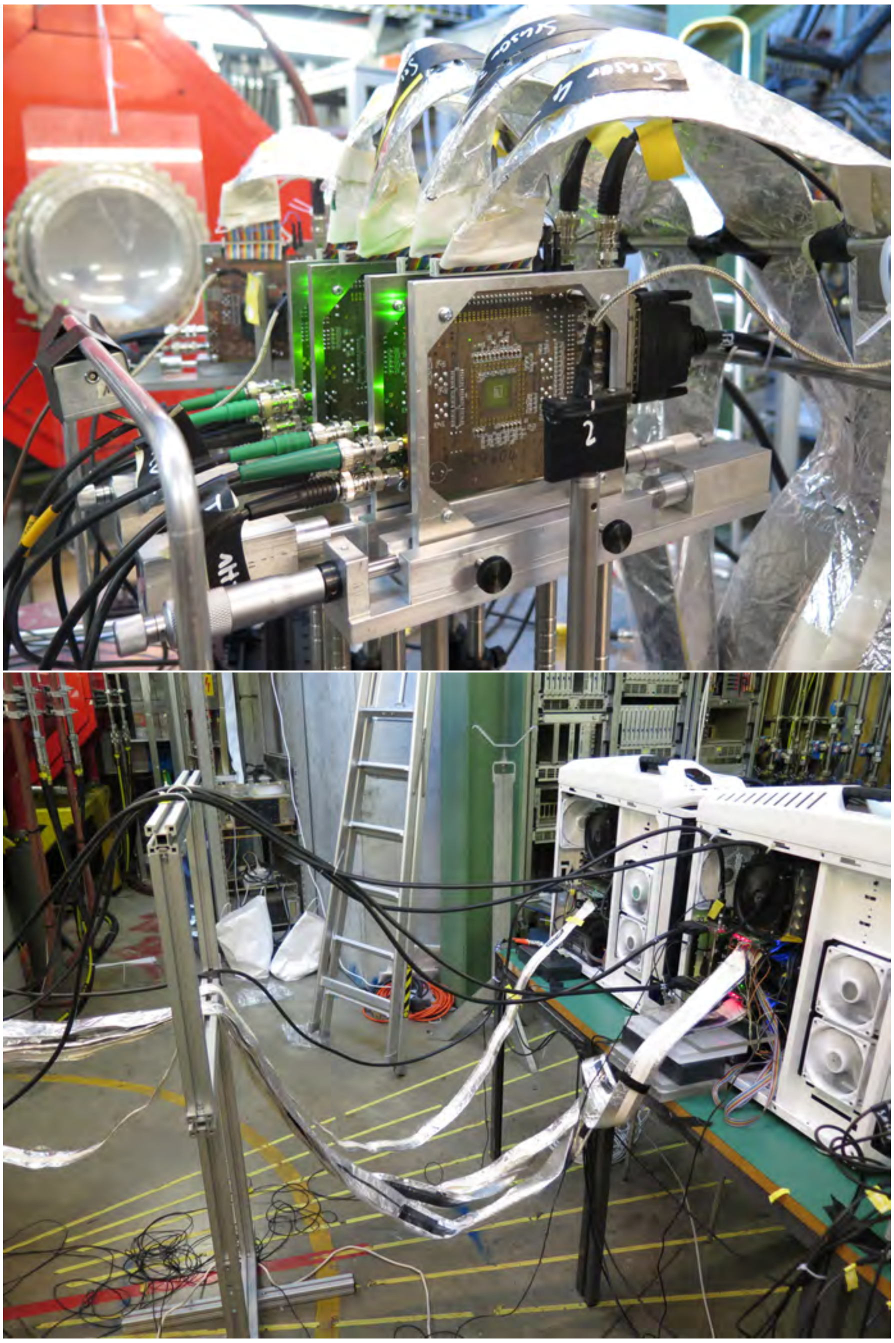

Figure 9.1: Pictures of the PSI setup: The top picture shows a close view of the setup from the backside. The red magnet in the back is the last quadrupole from the beamline with the beam window, secured by a plastic plate. The bottom picture shows the cabling to the readout computer. The front computer is the telescope readout PC, the back one is used for the single MuPix setup.

cables, while the readout was done via LVDS links for better signal quality, requiring an additional PCB with LVDS receivers and transmitters at the MuPix boards. Additional scintillating tiles in front and behind the telescope were used as a timing reference. Similar to the DESY testbeam a computer in the measuring hut was set up to remotely control the readout PC. Both computers and the power supplies were connected to the local network.

Sensors

For this testbeam the MuPix 6 prototypes were used. All four 250 µm thick sensors were directly glued to thinned PCBs. The prototypes are listed in Table 9.1. The thinner sensors glued directly on the boards reduced the effective radiation length by a factor of 10. This is a great improvement for low momentum tracking. However the final goal is to use 50 µm sensors, glued on 25 µm Kapton foil.

Layer	PCB number	Mounting	Threshold [mV]	x/X_0
1	# 57	glued on thin PCB	650	2.5 ‰
2	# 60	glued on thin PCB	650	2.5 ‰
3	# 58	glued on thin PCB	650	2.5 ‰
4	# 4604	glued on thin PCB	650	2.5 ‰

Table 9.1: Overview over the sensors used for the PSI testbeam. Sensor 1 was the closest to the beam window, while layer 4 was the last one.

9.2 Performance

DAQ

The DAQ software, still based on a pull architecture, was developed, re-factored and merged with the DAQ system of the sensor standalone test setup in the time between the DESY and PSI testbeams and included new features:
The online monitoring was moved from a separate macro to a thread in the telescope DAQ using the data directly without having to read the data files again, which made it possible to change the runs only after 500 MB of data instead of every 30 seconds. The FPGA firmware was also merged with the MuPix standalone firmware resulting in new additional changeable settings, like the timing of the readout signals and a throttle limiting the highest possible readout frequency of the FPGA. Especially the readout throttle changed the behavior of the DAQ essentially. While using the throttle, the DAQ was running stably without a memory leakage. However, removing the throttle triggered the FPGA to send empty frames (or with hits, if there were any) with a frequency of 50 MHz. This rate could not be handled by the DAQ and lead to an overwriting of the frame pointer in the queues. This issue will be solved for future versions by reducing the amount of newly created pointers by using a large fixed size ring buffers.

Run number	TS Division Factor	TS Binsize	FPGA Throttle	Wait Time	Source Intensity	Duration
57	0x5	80 ns	0xAFFE	2.5 ms	250 kBq	≈ 5 h
61	0xF	164 µs	0xAFFE	2.25 ms	3.7 MBq	15 min
70 - 73	0xF	164 µs	0xFF	12.75 µs	3.7 MBq	30 min
86 - 88	0x0	2.5 ns	0x80	6.4 µs	3.7 MBq	14 min
86 - 88	0x0	2.5 ns	0x80	6.4 µs	3.7 MBq	14 min
91 - 137	0x8	640 ns	0xF4	12.7 µs	3.7 MBq	≈ 9 h
139	0x8	640 ns	0xF4	12.7 µs	0.0	42 min

Table 9.2: List of the runs taken at PSI. The FPGA throttle set the minimal wait time between two readout cycles and the time stamp (TS) division factor d (second column) reduces the timestamps frequency by a factor of 2^d. This results in the TS Binsize, which is listed next to the division factor. The FPGA throttle is the minum number of 20 MHz clockcycles between to readouts. This results in the wait time. The last run was used as an area background run.

Data Runs

During this campaign only a few runs were taken while debugging the setup and performing source tests. The time stamp performance and the synchronization of the telescope were the only tested features. A 3.7 MBq and a 250 kBq ^{90}Sr-source were used and placed behind the last plane pointing towards the first plane. With this setup, various data runs were taken in order to search for coincident hits on the four planes. For all stored runs, the threshold was fixed and the maximum FPGA readout frequency was limited to the values in Table 9.2, which summarizes the runs taken.

Unfortunately a bug in the FPGA firmware resulted in a undesirable issue: The time stamps were not Gray encoded and the least significant bit was switching with a very high frequency, which was limiting the maximum usable time stamp frequency. In addition, normal counting resulted in all 8 bits switching at the same time which introduces a considerable amount of cross talk and can cause discharge of the capacitors that store the time stamps. This also lead to the issues of sampling while switching explained in subsection 5.4.2.

PSI File Structure

The readout software developments towards this testbeam an the MuPix 6 made it possible to operate the telescope with time stamps switched on. In addition the data files written in this testbeam are time sorted. All hits, which belong to the same coarse counter are fetched and merged to a frame, which is written to the file. This makes it easier to do the offline analysis. The time information is created as described in Section 6.3. To have a unique time information, the wait time between two readouts has to be shorter as the time stamp counter overflow time of 256 times time stamp bin size. Therefore the run number 57 should not be used for analysis.

9.3 Analysis

The analysis of the PSI data was relatively simple. The radioactive source runs were studied with respect to the time stamp distributions for different sensors and their correlations after the hot pixel remover was tested.

9.3.1 Hot Pixel Removal

The hot pixel removal works along the same principle as described for the DESY testbeam (see section 8.4). The first step is to remove the hot pixel with more than 5 % of the total hits. The advantage of the MuPix 6 sensor is that all addresses are working correctly. Therefore also the second step of the hot pixel remover, namely the removal of noisy hits, can be applied. The effect of removing all pixels with more hits than

$$\#Hits > \#\overline{hits} + 6 \cdot \sigma_{\overline{hits}} = \#\overline{hits} + 6 \cdot \sqrt{\#\overline{hits}} \tag{9.1}$$

is shown for run 71 in Figure 9.2.

The upper three plots, corresponding to sensor 2 show, that the hot and noisy pixel remover works. The noisy pixels are also effectively removed. But this noisy pixels removal method has a weak point in the high statistics limit. For high statistics, the square root of the mean value becomes small compared to the mean value. Any systematical variations in the efficiency or heterogeneous occupancy of the sensor will lead to a removal of the pixels which are systematically more often on. This effect is shown in the lower two plots in Figure 9.2. A large number of slightly noisier pixels is removed, even if they only have a few percent more hits.

One reason for heterogeneous occupancy could be the missing individual pixel tuning, which results in baseline variations relative to the threshold. This results in a reduced effective threshold for some pixels and more signals are visible for the low energy (0.55 MeV) particles from the radioactive source. This effect is studied at the moment [24].

Due to the weak point of the hot pixel removal for high statistics, this methods should be used very carefully. For the following timing analysis this method is suitable. For a tracking analysis, this method can be replaced by another more robust removal method. This can be done for example by studying the occupancy distributions and apply a cut on the occupancy.

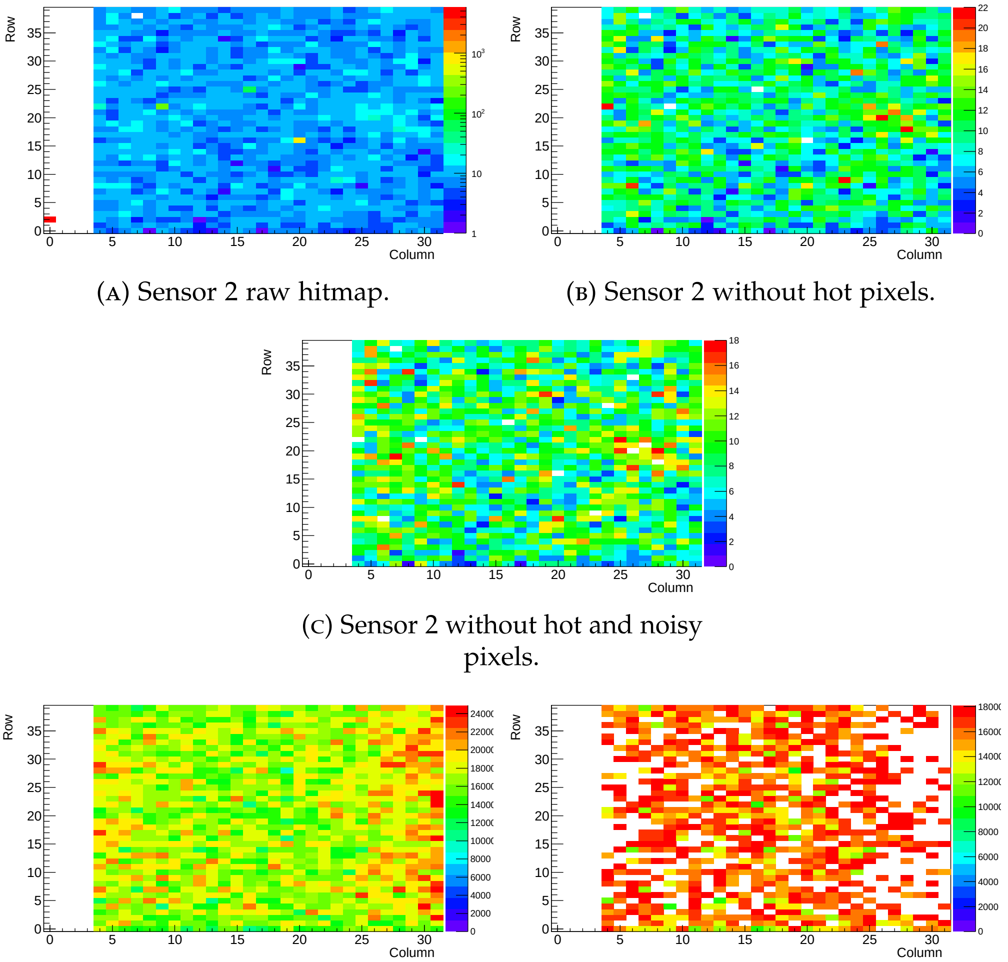

(a) Sensor 2 raw hitmap.

(b) Sensor 2 without hot pixels.

(c) Sensor 2 without hot and noisy pixels.

(d) Sensor 4 hitmap without hot pixels.

(e) Sensor 4 Hitmap without hot and noisy pixels.

Figure 9.2: The hitmaps for run 71 before and after hot and noisy pixel removal. Colums 0-4 use the single stage amplifier from the MuPix 4 design and are switched off.

9.3.2 Timing Analysis

The first realized issue with the time stamps was a bug in the software. Due to a wrong conversion, all time stamp division factors larger than 9 can not be used, because the file writing thread used a different division factor than the actual one. This lead to a wrong definition of the coarse time bins and resulted in a wrong frame creation. Therefore the runs 61 and 70-73 can not be used for the timing analysis.

Run 93 is chosen to get an overview over the time stamp distribution. This run had a time stamp frequency of 640 ns, which corresponds to the time stamp division factor of 8. The readout speed of the FPGA was limited to one readout every 12.7 µs. Therefore an unambiguous, absolute time information assignment is guaranteed. The time stamp distributions of all 4 sensors for run 93 are shown exemplary in Figure 9.3: The sensor 4, which is closest to the source, sees most particles. Sensor 3 has over an order of magnitude less hits than sensor 4 and sensor 2 has less than sensor 3. Sensor 2, has the lowest absolute number of entries and statistical fluctuations are visible. Sensor 1 has more entries, which are produced by a hot pixel.

However, the distributions are all flat as expected for measurements with a radioactive source. A closer look on Figure 9.3 shows, that the sensor 1 and 2 have many hits in the zeroth bin. This is most likely caused by a noisy pixel. These noisy pixels also explain the higher number of hits for sensor 1 compared to sensor 2.

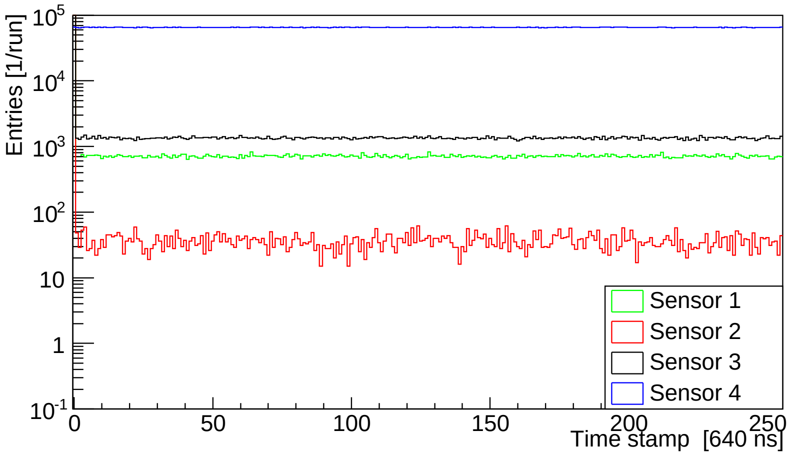

FIGURE 9.3: Time stamp distribution for the four sensors. The plotted data shows the run 93 with the ^{90}Sr source.

The more interesting part of the time stamp information is to analyze whether the hits taken during the source runs were due to particles from the ^{90}Sr-source or only noise hits. Hits from real particles should be time correlated in different layers. To study this effect all time correlations of sensor layer 4 with the others for run 93 are summarized in Figure 9.4. The left column shows the correlation before removing the hot and noisy pixel as described above, while the right column shows the clean samples.

It is expected, that the number of correlated hits between layer 4 and 3 is the highest, because the source is mounted directly behind layer 4 and points to layer 1 in direction of the beam window. Therefore the correlations between sensor 4 and 1 should contain the smallest amount of entries. This is not the case in the raw data. The high number of coincident hits between layer 1 and 4 in Figure 9.4 was caused by a hot pixel in sensor 1, which was always on. This can be seen in the facts that first the diagonal line is flat and does not have this sharp line in the middle containing over an order of magnitude more hits. Secondly there are many hits with time stamp 0 for sensor one, which are most likely caused by hot pixel, because all these entries disappear after removing the hot pixels.

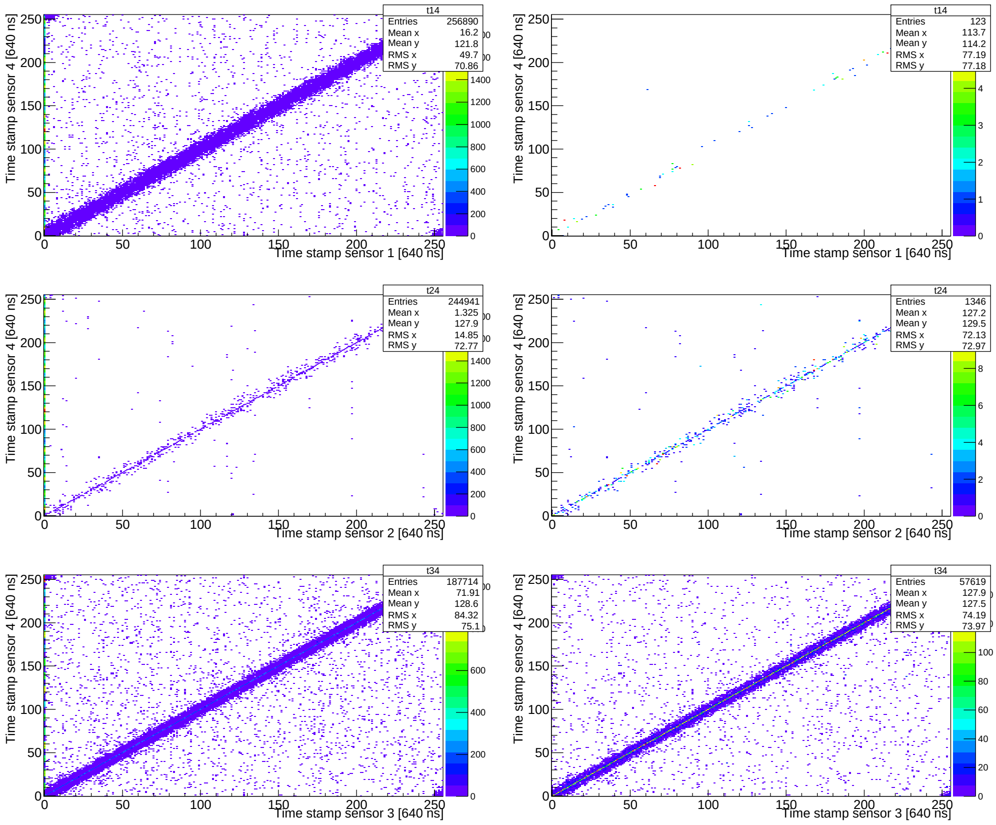

FIGURE 9.4: Timing measurements with the ^{90}Sr source at PSI. The plots show the correlations between sensors 4 and the others for run 71. On the left column the raw hits plots are shown and on the right column, the results after removing the hot pixels are shown.

After removing all hot pixels, the plots, shown in the left column in Figure 9.4 look exactly as expected: Clear straight diagonal lines and two clusters in the top left and bottom right corners. The number of entries is decreasing with the number of layers crossed due to scattering and absorption of the particles, exactly as expected. There is also no offset visible, which means that the time counters were synchronously reset at both FPGAs.

The entries in the corner are a result of the time stamp counter overflow. If the counters are near the minimum/maximum, it can happen that one hit which is slightly later in time sees the counter switching, while the correlated earlier hit sees a high time stamp counter.

The difference between the plots before and after removing the hot pixels from layers 4 and 3 is small, which is expected, because the noisiest pixels are in layers 1 and 2. Layers 3 and 4 do not have hot pixel, but many noisy pixels.

Besides all the clear diagonal line there are equal distributed uncorrelated hit in Figure 9.4. This caused by frames with more than one hit on plane 4. These frames are rare, compared to the frames with only one hit in layer 4.

For the final telescope, a more precise time stamp information is needed to reduce the particle multiplicities which did not play any role for source tests. This was not possible at the test beam. A more detailed study of those effects is ongoing at the moment [24]. It seems to be possible to increase the time stamp frequency after changing the FPGA firmware.

Searching for spatial correlations by looking only at timed hits was not successful due to the strong scattering of the low energy of 0.55 MeV of the particles coming from the source.

Part III

Conclusions

Chapter 10

Summary & Outlook

10.1 Summary

The MuPix telescope was successfully developed as an integration test for the Mu3e experiment and for usage at testbeams at the Paul-Scherrer-Institute in Switzerland. A flexible mechanical concept, based on optomechanical components from Thorlabs and custom PCB holders was designed and realized. The DAQ-software was implemented on a powerful computer with a graphical user interface, online monitoring and a set of analysis macros for offline hot pixel removal and track reconstruction.

The system was used with great success at two testbeam campaigns: The DESY testbeam in February 2014 showed that the telescope concept, using the MuPix 4 prototype, works and the DAQ runs stably. It was confirmed that the readout is able to handle high hit rates in the order of 600 kHz per sensor. The mechanical alignment of the telescope achieved a precision of below 100 µm. The data analysis results prove that the track reconstruction and the hot pixel removal are working. The software alignment was done with a precision below the pixel size of 92x80 µm^2.

The second testbeam at PSI was supposed to measure the time resolution of the MuPix6 and take high statistic data runs to analyze the track reconstruction algorithm in more detail. Issues with the accelerator resulted in no beam during this week and only timing tests with a ^{90}Sr source were performed. First these measurements showed that the time stamps of the MuPix6 are operational and the system is running synchronously. Secondly, the new DAQ software was tested and approved. The new LVDS signal transmission improved the data quality and all hits were assigned correctly.

To understand the track reconstruction a simulation of the telescope was developed and the track reconstruction was successfully analyzed. It was possible to determine a reconstruction efficiency of up to 96.5 % for events with two tracks and up to two background hits per plane for the two configurations. The corresponding background rejection, normalized to the total number of reconstructed tracks, reaches more than

99 %, depending on the $\mathcal{X}^2$ cut value, the scattering effect of the planes and the geometrical properties.

10.2 Outlook

Despite its currently stable setup, the MuPix telescope still has potential for further improvements:
An automatized software alignment procedure and online track reconstruction could be implemented directly in the DAQ-software. The maximum track rate could be increased by using direct memory access for higher data transmission.
The MuPix telescope performance strongly depends on the MuPix sensors, which are under active development at the moment. Therefore, new prototypes will be produced and have to be integrated into the DAQ. Especially the size of the sensors will change from the current size of approximately 10 mm^2 to 4 cm^2 while the sensors thickness will decrease down to 50 µm. Replacing the central part of the PCBs by a thin Kapton foil will reduce the thickness to 0.6 ‰ of a radiation length per layer. The efficiency of the sensors was determined to be above 99 %, which will be the case for the future sensors and lead to a high efficiency for the telescope of above 96 %. The time stamps of the sensor will also be finer for the future sensors. For the final version, a resolution better then 50 ns is aspired.
The readout speed also will be increased to handle the 20 MHz track rate. To process this high rate it is necessary to run at single track frames, which requires a readout speed of higher than 20 MHz.
The mechanical principle is working fine but could be improved by a system which makes it possible to move the planes remotely from the DAQ system. In this case, the fine mechanical alignment could be done with beam switched on.
The track reconstruction algorithm, especially the execution speed could be optimized. In this context, moving to the GPU for tracking could result in a higher reconstruction speed.
The existing simulation framework could be used to optimize the distances between the sensor planes and study the influence of misalignment between different planes.
A third testbeam carried out at the end of July 2014 at PSI, which is not discussed in this thesis, provided high statistics data. This data will be analyzed for further studies of the performance at low particle momenta.

As the MuPix telescope is the first operating HV-MAPS telescope, the achieved results are very promising. The HV-MAPS concept will be scaled up to larger systems. The experiences collected with the MuPix telescope are very useful and will help to construct the Mu3e pixel detector. The results shown are a first step towards the complete detector.

With all these possible improvements the MuPix telescope will be a very flexible and powerful tool for future detector development even beyond the Mu3e experiment. Additionally it fills a gap in the current availability of beam telescopes due to its optimization for high rates and low momentum particles.

Part IV

Appendix

Appendix A

Track Fitting

The set of parameters as result of the matrix inversion for the simple track fit is given by

$$\begin{aligned}
a_x &= \frac{\sum_{i=1}^{n} z_i \cdot \sum_{i=1}^{n} {z_i}^2}{\left(\sum_{i=1}^{n} {z_i}^2\right)^2 - \sum_{i=1}^{n} z_i \cdot \sum_{i=1}^{n} 1} \sum_{i=1}^{n} x_i + \frac{-\sum_{i=1}^{n} 1}{\left(\sum_{i=1}^{n} {z_i}^2\right)^2 - \sum_{i=1}^{n} z_i \cdot \sum_{i=1}^{n} 1} \sum_{i=1}^{n} (x_i + z_i) \\
x_0 &= \frac{-\sum_{i=1}^{n} z_i}{\left(\sum_{i=1}^{n} {z_i}^2\right)^2 - \sum_{i=1}^{n} z_i \cdot \sum_{i=1}^{n} 1} \sum_{i=1}^{n} x_i + \frac{1 + \frac{-\sum_{i=1}^{n} z_i \cdot \sum_{i=1}^{n} 1}{\left(\sum_{i=1}^{n} {z_i}^2\right)^2 - \sum_{i=1}^{n} z_i \cdot \sum_{i=1}^{n} 1}}{\sum_{i=1}^{n} z_i} \sum_{i=1}^{n} (x_i + z_i) \qquad \text{(A.1)} \\
a_y &= \frac{\sum_{i=1}^{n} z_i \cdot \sum_{i=1}^{n} {z_i}^2}{\left(\sum_{i=1}^{n} {z_i}^2\right)^2 - \sum_{i=1}^{n} z_i \cdot \sum_{i=1}^{n} 1} \sum_{i=1}^{n} x_i + \frac{-\sum_{i=1}^{n} 1}{\left(\sum_{i=1}^{n} {z_i}^2\right)^2 - \sum_{i=1}^{n} z_i \cdot \sum_{i=1}^{n} 1} \sum_{i=1}^{n} (x_i + z_i) \\
y_0 &= \frac{-\sum_{i=1}^{n} z_i}{\left(\sum_{i=1}^{n} {z_i}^2\right)^2 - \sum_{i=1}^{n} z_i \cdot \sum_{i=1}^{n} 1} \sum_{i=1}^{n} x_i + \frac{1 + \frac{-\sum_{i=1}^{n} z_i \cdot \sum_{i=1}^{n} 1}{\left(\sum_{i=1}^{n} {z_i}^2\right)^2 - \sum_{i=1}^{n} z_i \cdot \sum_{i=1}^{n} 1}}{\sum_{i=1}^{n} z_i} \sum_{i=1}^{n} (x_i + z_i)\,.
\end{aligned}$$

Iterative calculation of the covariance matrix:

The covarianc ematrix at the reference plane is given as

$$\mathrm{cov}(0) = \begin{pmatrix} s_{scatter} & 0 \\ 0 & s_{scatter} \end{pmatrix}. \tag{A.2}$$

The parameter vector $\vec{a}_i$ has to be propagated to the next layer, which is placed at a distance dz:

$$\vec{a}_i = F \cdot \vec{a}_{i-1} \tag{A.3}$$

with the propagation matrix

$$F(i,i-1) = \begin{pmatrix} 1 & 0 & 0 & 0 \\ 0 & 1 & 0 & 0 \\ dz & 0 & 1 & 0 \\ 0 & dz & 0 & 1 \end{pmatrix}. \tag{A.4}$$

The covariance matrix at layer i follows as:

$$\mathrm{cov}(i) = F(i,i-1)\,\mathrm{cov}(i-1)\,F(i,i-1)^{\mathrm{T}}. \tag{A.5}$$

The local measurement covariance is now defined as:

$$\mathrm{cov}_m(i) = \begin{pmatrix} \mathrm{cov}(i)_{22} & \mathrm{cov}(i)_{23} \\ \mathrm{cov}(i)_{32} & \mathrm{cov}(i)_{33} \end{pmatrix} + \begin{pmatrix} s_x & 0 \\ 0 & s_y \end{pmatrix}. \tag{A.6}$$

The error for each plane is given by the following equation:

$$\Sigma_i = (H \cdot F)\Sigma_{a_0}(H \cdot F)^{\mathrm{T}}. \tag{A.7}$$

The element (0,0) is now the uncertainty on the x position and (1,1) the uncertainty on the y position.

Appendix B

Gray Code Converter

In C++ the conversion can be realized with this loop [62]:

```
//Binary to Gray

unsigned int binaryToGray(unsigned int num)
{
        return (num >> 1) ^ num;
}

// Gray to binary

unsigned int grayToBinary(unsigned int num)
{
    unsigned int mask;
    for (mask = num >> 1; mask != 0; mask = mask >> 1)
    {
        num = num ^ mask;
    }
    return num;
}
```

Appendix C

Digital to Physical Address Conversion

The MuPix 4 and 6 prototypes consist of a pixel matrix of 32x40[*] pixels. However, the digital scheme consists of a 64x20 pixel matrix. Therefore, two transformations have to be used: One to transform from digital to physical address and vice versa.
For the MuPix4 prototype, this is straight forward and can be defined as [23], taking into account that all divisions are integer divisions:

$$\begin{aligned} \mathrm{row}_{\mathrm{physcial}} &= \mathrm{row}_{\mathrm{digital}} \cdot 2 + \left(\mathrm{column}_{\mathrm{digital}} \text{ modulo } 2\right) && \text{(C.1)} \\ \mathrm{column}_{\mathrm{physcial}} &= \mathrm{column}_{\mathrm{digital}}/2 && \text{(C.2)} \end{aligned}$$

The reverse transformation is defined as:

$$\begin{aligned} \mathrm{row}_{\mathrm{digital}} &= \mathrm{row}_{\mathrm{physical}}/2 && \text{(C.3)} \\ \mathrm{column}_{\mathrm{digital}} &= \mathrm{column}_{\mathrm{physical}} \cdot 2 + \left(\mathrm{row}_{\mathrm{physical}} \text{ modulo } 2\right) && \text{(C.4)} \end{aligned}$$

For the MuPix6 prototype, the transformation is a bit more complex. An address scheme change leads to the following transformation:

[*] The first number always addresses the number of columns and the second the number of rows.

$$\begin{aligned}
\text{row}_{\text{physcial}} &= \text{row}_{\text{digital}} \cdot 2 \\
&\quad + \left(\left(\text{column}_{\text{digital}} - 1\right) \text{ modulo } 2\right) \\
&\quad +2 \cdot \left(\left(\text{column}_{\text{digital}} - 1\right) \text{ modulo } 2\right) \left(\left(\text{row}_{\text{digital}}\right) \text{ modulo } 2\right) \\
&\quad -2 \cdot \left(\left(\text{column}_{\text{digital}} - 1\right) \text{ modulo } 2\right) \left(\left(\text{row}_{\text{digital}} - 1\right) \text{ modulo } 2\right) && \text{(C.5)}
\end{aligned}$$

$$\text{column}_{\text{physcial}} = \left(\text{column}_{\text{digital}}/2\right) \qquad \text{(C.6)}$$

Appendix D

FPGA Communication

The software communication with the FPGAs is done via two registers: A writable register to send commands, the write register in Table D.2 and a read only register to get status information, the read register in Table D.3 are used.

The timing delays used for the testbeams and their corresponding bits in the register are listed in Table D.1.

Address	Delay	DESY	PSI
3 down to 0	Delay LDPIX-PULLDOWN	0x4	0x3
7 down to 4	Delay PULLDOWN-LDCOL	0x1	0x3
11 down to 8	Delay LDCOL-RDCOL	0x3	0xC
15 down to 12	Delay RDCOL-RDCOL	0x3	0x7
19 down to 16	Delay RDCOL-PULLDOWN	0x1	0xE
23 down to 20	RDCOL width	0x1	0x7
27 down to 24	PRIOUT sampling point, negative from end of RDCOL cycle	0x1	0x7
31 down to 28	Data sampling point, negative from end of RDCOL cycle	0x2	0x7

Table D.1: Read-out delay register values. All delays are given in readout clock cycles corresponding to 50 ns.

Offset	Register	Comments
0x00		**FPGA Control**
0x00	LEDs	Bits 7 down to 0: LEDs 15 down to 8
0x01	Resets	Bit 0: Reset all Bit 1: Memory writing Bit 2: Trigger logic Bit 3: Mupix IFs Bit 4: SPI IFs Bit 5: Injection generator Bit 6: Hitbus histogramming Bit 7: Bit 8: User part of PCIe Bit 9: Zero memory
0x08		**Slow Control**
0x08	Threshold DAC front	15 bit DAC (Bits 15 down to 1), writes SPI bus (threshold and injection)
0x09	Injection DACs front	2 15 bit DACs Bits 15 down to 1 Injection 1 Bits 31 down to 17 Injection 2
0x0A	Injection duration front	Bits 15 down to 0 Injection 1 Bits 31 down to 16 Injection 2
0x0B	Threshold DAC back	15 bit DAC (Bits 15 down to 1), writes SPI bus (threshold and injection)
0x0C	Injection DACs back	2 15 bit DACs Bits 15 down to 1 Injection 1 Bits 31 down to 17 Injection 2
0x0D	Injection duration back	Bits 15 down to 0 Injection 1 Bits 31 down to 16 Injection 2
0x0E	Injection	Perform injection(s) Bit 0: Injection 1 front Bit 1: Injection 2 front Bit 2: Injection 1 back Bit 3: Injection 2 back
0x0F	Slow Control (Chip SPI)	Bit 0: front `SIN` Bit 1: front `CK_C` Bit 2: front `CK_D` Bit 3: front `LD_C` Bit 4: back `SIN` Bit 5: back `CK_C` Bit 6: back `CK_D` Bit 7: back `LD_C`
0x10		**Trigger Control**
0x10	Trigger control register	Bits 5 down to 0: Trigger mask Bits 13 down to 8: Veto mask Bit 14: Reset scalers Bit 15: Generate single trigger
0x11	Trigger wait counter	24 Bits: 0 for no autotriggers Trigger generated every N 50 MHz cycles
0x12	Hitbus selection	Bit 0: Front hitbus from CTRL adapter (0)/from RO adapter (1) Bit 1: Back hitbus from CTRL adapter (0)/from RO adapter (1)
0x20		**Readout Control**
0x20	Readout Control register	Bit 0: Triggered RO Bit 1: Continuous RO Bit 2: Read now Bit 3: Read manual Bit 4: Reset event count Bit 6: Generate hits Bit 8: Disable front RO Bit 9: Disable back RO Bit 10: Enable Hitbus RO Bits 31 down to 16: Number of hits to generate
0x21	Manual readout bits	Bit 0: LDPIX front Bit 1: PULLDOWN front Bit 2: LDCOL front Bit 3: RDCOL front Bit 4: LDPIX back Bit 5: PULLDOWN back Bit 6: LDCOL back Bit 7: RDCOL back
0x22	Timestamp control	Bits 7 down to 0: timestamp front Bit 8: Use gray counter front Bit 9: Reset gray counter Bits 23 down to 16: timestamp back Bit 24: Use gray counter back Bits 31 down to 28: 2^x frequency divider wrt. 250 MHz
0x23	Fixedpattern register	Bits 11 down to 0: Hit pattern front Bits 27 down to 16: Hit pattern back
0x24	Readout timing register	See table D.1
0x25	Readout pause register	32 bit: Wait cycles before next LDPIX
0x28		**Histogram Control**
0x28	Hitbus histogram control	Bit 0: Take data front Bit 1: Zero histogram front Bit 2: Take data back Bit 3: Zero histogram back
0x29	Hitbus histogram bin	Bits 9 down to 0: Front bin Bits 25 down to 16: Back bin
0x38		**DMA Registers**
0x38	DMA control register	Bit 0: Enable DMA Bit 1: Perform DMA now
0x39	DMA control address low	Bits 31 down to 0 of address
0x3A	DMA control address high	Bits 63 down to 32 of address
0x3B	DMA data address low	Bits 31 down to 0 of address
0x3C	DMA data address high	Bits 63 down to 32 of address

Table D.2: Register map for the writeable registers

Offset	Register	Comments
0x00		**FPGA Control**
0x00	Dipswitch and PLLs	Bits 7 down to 0: Dipswitch Bit 8: 50 MHz PLL locked Bit 10: 1 if ctrl_clkin2 is used Bit 11: No transitions on clkin_50 Bit 12: No transitions on ctrl_clkin2
0x01	Version	Git hash
0x08		**Slow Control**
0x0F	Slow Control (Chip SPI)	Bit 0: front SOUT_C Bit 1: front SOUT_D Bit 2: back SOUT_C Bit 3: back SOUT_D
0x10		**Trigger Control**
0x10	Trigger bits	Bits 5 down to 0: Trigger inputs Bit 6: Busy Bit 7: Zeroing memory Bit 8: Busy front Bit 9: Busy back
0x11	Trigger counter	32 Bits
0x12	Raw trigger counter	32 Bits
0x13	Trigger 0 scaler	32 Bits
0x14	Trigger 1 scaler	32 Bits
0x15	Trigger 2 scaler	32 Bits
0x16	Trigger 3 scaler	32 Bits
0x17	Trigger 4 scaler	32 Bits
0x18	Trigger 5 scaler	32 Bits
0x20		**Readout Control**
0x20	Memory write address	Bits 15 down to 0
0x21	Last end of event address	Bits 15 down to 0
0x22	Front readout signals	Bit 0: Hitbus Bit 1: Priout Bits 7 down to 2: Row address Bits 13 down to 8: Col address Bits 21 down to 14: Timestamp
0x23	Back readout signals	Bit 0: Hitbus Bit 1: Priout Bits 7 down to 2: Row address Bits 13 down to 8: Col address Bits 21 down to 14: Timestamp
0x24	RO state machines	Bits 7 down to 0: Memorywriter Bits 15 down to 8: Front RO Bits 23 down to 16: Back RO
0x25	Coarse counter	Upper 32 bits of 400 MHz 48 bit counter
0x28		**Histogram reading**
0x29	Hitbus histogram data	Bits 15 down to 0: Front bin content Bits 31 down to 16: Back bin content
0x38		**DMA Registers**
0x38	DMA status register	Bits 7 down to 0: State machine state Bits 19 down to 16: Start counter Bits 23 down to 20: Granted counter Bits 27 down to 24: Data written counter Bits 31 down to 28: Interrupt counter

Table D.3: Register map for the read-only registers

Appendix E

DAC Settings

DACs (Digital-to-Analog Converters), implemented on the chip, can be used to control current flows in different elements of the chip. Those currents influence the performance and should be set to the correct values. A summary of the existing DACs and their settings are summarized in Table E.1. It has to be mentioned, that one unused DAC value has to be set to an arbitrary value. Ignoring this DAC sends one DAC less and therefor, the shift register is not completely filled and the input values are assigned to the wrong DACs.

DAC	default	MuPix4	MuPix6
VPDAC	0x0	0x2	0x0
VPComp	0x3C	0x14	0x3C
VNDel	0xA	0xA	0xA
VNLoad	0x5	0x5	0x5
VNFoll	0xA	0x10	0xA
VNFB	0xA	0x1	0xA
VN	0x3C	0x3C	0x3C
THRes	0x3C	0x8	0x3C
BLRes	0x3C	0x1	0x3C
VNFB2	–	–	0x1
VNLoad2	–	–	0x5
VN2	–	–	0x3C
BLRes2	–	–	0x3C

Table E.1: Overview over the DAC values for the MuPix 4 and 6. The default values were chosen by Ivan Perić. The four last DACs in the table are the ones controlling the 2nd amplification stage. Therefor, they do not exist in the MuPix4. The red marked DAC was set accidentally to a wrong value because of a communication mistake.

List of Figures

List of Tables

Bibliography

[1] J. Beringer et al. Review of Particle Physics (RPP). *Phys.Rev.*, D86:010001, 2012.

[2] Wikimedia Commons. Standard model of elementary particles, 2014. [Online; accessed 25-july-2014].

[3] G. Aad et al. Observation of a new particle in the search for the Standard Model Higgs boson with the ATLAS detector at the LHC. 2012.

[4] S. Chatrchyan et al. Observation of a new boson at a mass of 125 GeV with the CMS experiment at the LHC. *Phys.Lett.B*, 2012.

[5] Q. R. Ahmad et al. Measurement of the charged current interactions produced by b-8 solar neutrinos at the sudbury neutrino observatory. *Phys. Rev. Lett.*, 87:071301, 2001.

[6] F.P. An et al. Observation of electron-antineutrino disappearance at Daya Bay. *Phys.Rev.Lett.*, 108:171803, 2012.

[7] Y. Fukuda et al. Evidence for oscillation of atmospheric neutrinos. *Phys. Rev. Lett.*, 81:1562–1567, 1998.

[8] W. Rodejohann and A. Schöning. The Standard Model of Particle Physics. Lecture notes, 2012.

[9] U. Bellgardt et al. Search for the Decay $\mu^+ \to e^+e^+e^-$. *Nucl.Phys.*, B299:1, 1988.

[10] L.M. Brarkov et al. Search for $\mu^+ \to e^+\gamma$ down to 10^{-14} branching ratio. *Research Proposal to PSI*, 1999.

[11] W. J. Marciano, T. Mori, and J. M. Roney. Charged Lepton Flavor Violation Experiments. *Ann.Rev.Nucl.Part.Sci.*, 58:315–341, 2008.

[12] J. Adam et al. New constraint on the existence of the $\mu^+ \to e^+\gamma$ decay. *Phys. Rev. Lett.*, 110:201801, May 2013.

[13] A.M. Baldini, F. Cei, C. Cerri, S. Dussoni, L. Galli, et al. MEG Upgrade Proposal. *ArXiv e-prints*, January 2013.

[14] A. Blondel et al. Letter of intent for an experiment to search for the decay $\mu \to eee$, 2012.

[15] T. Prokscha et al. The new high-intensity surface muon beam μe4 for the generation of low-energy muons at psi. *Physica*, B 364-375:460–463, 2006.

[16] R. M. Djilkibaev and R. V. Konoplich. Rare Muon Decay $\mu^+ \to e^+e^-e^+\nu_e\bar{\nu_\mu}$. *Phys.Rev.*, D79:073004, 2009.

[17] M. Zimmermann. Cooling with Gaseous Helium for the Mu3e Experiment. Bachelor thesis, Heidelberg University, 2012.

[18] Lukas Huxold. Cooling of the Mu3e Pixel Detector. Bachelor thesis, Heidelberg University, 2014.

[19] Adrian Herkert. personal communication. Master's thesis, Physikalisches Institut, Heidelberg, 2014.

[20] A.-K. Perrevoort. Characterisation of High Voltage Monolithic Active Pixel Sensors for the Mu3e Experiment. Master thesis, Heidelberg University, 2012.

[21] H. Augustin. Charakterisierung von HV-MAPS. Bachelor thesis, Heidelberg University, 2012.

[22] R. Philipp. Characterisation of High Voltage Monolithic Active Pixel Sensors for the Mu3e Experiment. Master thesis, Heidelberg University, 2014.

[23] Fabian Foerster. HV-MAPS Readout and Direct Memory Access for the Mu3e Experiment. Master thesis, Heidelberg University, 2014.

[24] Heiko Augustin. Title not fixed yet. Master thesis, Heidelberg University, 2014.

[25] P. Eckert. *Title to be defined*. PhD thesis, Kirchhoff Institut für Physik, 2014. personal contact.

[26] G.S. Bauer, Y. Dai, and W. Wagner. SINQ layout, operation, applications and R&D to high power. *J. Phys. IV France*, 12(8):3–26, 2002.

[27] J. Ashkin H. A. Bethe. Passage of radiation through matter. *Nucl. P*, 1:253, 1953.

[28] S.M. Seltzer and M.J. Berger. Energy loss straggling of protons and mesons. In *In Studies in Penetration of Charged Particles in Matter*, volume 39 of *Nuclear Science Series*. Nat. Academy of Sciences, 1964.

[29] G. Wentzel. Zur Theorie der Streuung von β-Strahlen. *Ann. d. Phys.*, 374:335, 1922.

[30] S. Goudsmit and J.L. Saunderson. Multiple Scattering of Electrons. II. *Phys.Rev.*, 58:36–42, 1940.

[31] S. Goudsmit and J.L. Saunderson. Multiple Scattering of Electrons. *Phys.Rev.*, 57:24–29, 1940.

[32] G. Molière. Theory of the scattering of fast charged particles. 1. Single scattering in the shielded Coulomb field. *Z.Naturforsch.*, A2:133–145, 1947.

[33] G. Molière. Theory of the scattering of fast charged particles. 2. Repeated and multiple scattering. *Z.Naturforsch.*, A3:78–97, 1948.

[34] H.A. Bethe. Molère's theory of multiple scattering. *Phys.Rev.*, 89:1256–1266, 1953.

[35] H.W. Lewis. Multiple Scattering in an Infinite Medium. *Phys.Rev.*, 78:526–529, 1950.

[36] V. L. Highland. Some Practical Remarks on Multiple Scattering. *Nucl.Instrum.Meth.*, 129:497, 1975.

[37] K. Nakamura et al. Review of particle physics. *J. Phys.*, G37:075021, 2010.

[38] I. Perić. A novel monolithic pixelated particle detector implemented in high-voltage CMOS technology. *Nucl.Instrum.Meth.*, A582:876, 2007.

[39] L. Greiner, E. Anderssen, H.S. Matis, H.G. Ritter, J. Schambach, J. Silber, T. Stezelberger, X. Sun, M. Szelezniak, J. Thomas, F. Videbaek, C. Vu, and H. Wieman. A MAPS based vertex detector for the STAR experiment at RHIC. *Nucl. Instr. Meth.*, A 650:68 – 72, 2011. International Workshop on Semiconductor Pixel Detectors for Particles and Imaging 2010.

[40] Texas Instruments Incorporated. LVDS Application and Data Handbook, 2002.

[41] U.S. NIM committee. Standard nim instrumentation system. Technical report, U.S. Department of Energy, May 1990.

[42] G. Cowan. *Statistical Data Analysis*. Oxford University Press, Oxford, 1998.

[43] M. Kiehn. *Track reconstruction for the Mu3e experiment*. PhD thesis, Heidelberg University, In preparation.

[44] Niklaus Berger. MuPix Firmware. Personal Contact.

[45] I. Peric. MuPixel small pixel detector description. Internal Note.

[46] S. Shreshta. simulated pulse shapes. private communication.

[47] Frank Gray. Pulse code communication, 1953.

[48] HAMEG Instruments. *Power supply HMP 4030 HMP 4040*, April 2012.

[49] Keithley Instruments Inc. *High Voltage power supply series 2600 B*.

[50] Dirk Wiedner. MuPix Test PCB Develoment. Personal Contact.

[51] Qt Project. Qt project, 2014. Accessed: 21.06.2014.

[52] Boost. Boost c++ libraries, 2014. [Online; accessed 26-june-2014].

[53] JSON Group. Json (javascript object notation), 2014. Accessed: 21.06.2014.

[54] R. Brun et al. *ROOT Users Guide 3.1c*. Geneva, September 2001.

[55] T. Behnke et al. Test Beams at DESY. Technical report, DESY Hamburg, 2007.

[56] Desy Testbeam Group. DESY Testbeam Homepage.

[57] I.-M. Gregor. EUDET-Pixel Telescope. *PoS*, VERTEX2008:034, 2008.

[58] P. Roloff. The EUDET high resolution pixel telescope. *Nucl.Instrum.Meth.*, A604:265–268, 2009.

[59] T. Haas. A pixel telescope for detector R & D for an international linear collider. *Nucl.Instrum.Meth.*, A569:53–56, 2006.

[60] Marcel Stanitzki. DESY-II Teastbeam Facility. Talk on DESY telescope workshop, July 2014.

[61] M. Seidel et al. Production of a 1.3 MW proton beam at PSI. In *Proceedings of IPAC'10, Kyoto, Japan*, 2010.

[62] Wikimedia Commons. Gray code, 2014. [Online; accessed 07-july-2014].

Acknowledgments

At this point I would like to thank all the people who have supported my during my thesis:

First of all I would like to thank **Prof. Dr. André Schöning** for giving me the opportunity to work for the Mu3e group at this challenging topic and his support during the last year. I also would like to thank him and **Prof. Dr. Stephanie Hansmann-Menzemer** for the survey of my thesis.

The Mu3e group at Heidelberg for the good working atmosphere, the support wherever needed and the smooth testbeams in Hamburg and Villigen. Especially I would like to thank...

- **Heiko Augustin** for the great teamwork while merging the software and helping me implementing the MuPix6 prototype.
- **Niklaus Berger** for introducing me in multithreaded programming, the time invested in bug fixing and the great working firmware provided. Thank you also for the great discussions about tracking and for expanding my culinary experiences.
- **Dorothea vom Bruch** for being a great office mate, the reading of my thesis correcting my spelling and transporting my snowboard safely to Canada.
- **Simon Corrodi** for his great effort developing a MuPix4 emulator to test the telescope DAQ for the first time. Also thank you for the great Swiss Fondue.
- **Fabian Förster** for his assistance while performing the first steps in developing the DAQ and the great time talking about nerdy stuff.
- **Moritz Kiehn** for his patience while discussing the telescope tracking and his help while re-factoring the telescope code and for bringing a lot of cake and strawberries for the coffee break.
- **Raphael Philipp** for the great teamwork analyzing the MuPix3 PSI testbeam data and your help with the MuPix4.
- **Dirk Wiedner** for supporting me all time, while having an incredible workload, especially in the weeks before testbeams. Thank you for the smooth organization of my summer student stay at TRIUMF in Vancouver.
- **everybody** who read my thesis and gave me some correction hints.

Last but not least I also like to thank my family and my friends for supporting me from the very beginning of my studies and covering my back while I was caring ou this thesis.

Erklärung:

Ich versichere, dass ich diese Arbeit selbstständig verfasst habe und keine anderen als die angegebenen Quellen und Hilfsmittel benutzt habe.

Heidelberg, den (Datum) ....